Synthesis and Characterization of Fe-based/Fe_3Al-based/Al-based Metal Matrix Composites

鐵基/鐵三鋁基/鋁基金屬基複合材料的合成和表徵

CHUNG, Kam Chuen

鍾錦銓

A Thesis Submitted in Partial Fulfillment
of the Requirement for the Degree of
Master of Philosophy
in
Materials Science and Engineering

August 2007

Thesis/Assessment Committee

Professor HARK, Sui Kong (Chair)
Professor NG, Hang Leung Dickon (Thesis Supervisor)
Professor WONG, King Young (Committee Member)
Professor YAO, Kefu (External Examiner)

Abstract

Three types of metal matrix composites (MMCs), namely Fe-based /Fe_3Al-based /Al-based MMCs, were synthesized by the displacement reactions between selected metals and metal oxides during sintering.

The Fe-based MMC was synthesized by sintering of an Al-Fe_3O_4 powder mixture. Fe_3O_4 was initially reacted with Al to form FeO and Al_2O_3. FeO was then reduced to form Fe. Finally, Al_2O_3 and FeO reacted to form hercynite. The measured saturation magnetization of hercynite was smaller than that calculated. It was because the stoichiometric ratio of hercynite had been altered and it had a partially inverse spinel structure.

The Fe_3Al-based MMC products were reinforced by Al_2O_3, MgO or $MgAl_2O_4$. The first type, Fe_3Al-Al_2O_3 MMC was synthesized by sintering of a Fe-Al-Fe_3O_4 powder mixture. Initially, Al reacted with Fe to form Fe_2Al_5. The Fe_3O_4 was reduced by Fe_2Al_5 to form Fe and Al_2O_3, meanwhile, Al diffused from Fe_2Al_5 to Fe to form the Fe_3Al matrix. All the reactions were completed at 1400°C. The second type, Fe_3Al-MgO MMC was produced by a two-step sintering of a Fe-Al-Mg-Al_2O_3 powder mixture. During the step-one sintering at 480°C, a disintegrated sample containing Fe, Fe_2Al_5 and MgO was obtained. After grinding and pressing of the product, the step-two sintering produced a Fe_3Al matrix. To avoid the decomposition of MgO in this Fe_3Al matrix, the sintering temperature was limited to 1000°C. Similarly, the third type, Fe_3Al-$MgAl_2O_4$ MMC was synthesized by decreasing the relative amount of Mg. Residual Al_2O_3 reacted with MgO to form $MgAl_2O_4$ during the step-two sintering. The Fe_3Al-MgO and Fe_3Al-$MgAl_2O_4$ MMCs were measured to be 95% and 98% of their theoretical densities and their VHNs were determined to be

143 and 184, respectively.

The Al-based MMC was synthesized by sintering of an Al-Fe_3O_4 powder mixture. The displacement reaction between Al and Fe_3O_4 took place at 1100°C. Liquid (Al, Fe) with hypereutectic composition containing Al_2O_3 particles was obtained. The liquid was cooled down to room temperature by different routes, namely furnace-cooling and NaCl-solution-quenching. For the furnace-cooled sample, proeutectic Al_3Fe plates with length over hundreds of μm, plate-like divorced eutectic Al_3Fe and Al_2O_3 particles were found in the Al matrix. For the sample quenched from 700°C, the liquid solidified in hypoeutectic manner and Al dendrites were formed. The dendritic spacing was a few μm. Al-Al_6Fe eutectic was formed in the inter-dendritic regions. For that quenched from 900°C, the size of proeutectic Al_3Fe phases was reduced to tens of μm, the Fe-rich liquid solidified in eutectic manner and Al-Al_6Fe eutectic was formed, while the Fe-deficient liquid solidified in hypoeutectic manner and dendritic structure similar to that quenched from 700°C were formed.

摘要

三類型金屬基複合材料，即鋁基/鐵三鋁基/鐵基金屬基複合材料，已經透過被挑選的金屬和金屬氧化物在燒結時的置換反應被合成出來。

鐵基金屬基複合材料透過燒結鋁和四氧化三鐵的粉末混合物被合成出來。四氧化三鐵首先和鋁反應形成一氧化鐵和氧化鋁。一氧化鐵其後被原成鐵和氧化鋁。最後，氧化鋁和一氧化鐵反應形成鐵鋁尖晶石。。鐵鋁尖晶石被測量出來的飽和勵磁較計算值爲小。這是由於鐵鋁尖晶石的化學計算比已被變更和它擁有部分反尖晶石型結構。

鐵三鋁基金屬基複合材料被氧化鋁、氧化鎂或鎂鋁尖晶石增強。第一類型，氧化鋁鐵三鋁基金屬基複合材料透過燒結鐵、鋁和四氧化三鐵的粉末混合物被合成出來。首先，鐵和鋁反應形成鐵二鋁五。四氧化三被鐵二鋁五還原成鐵和氧化鋁，其間，鋁從鐵二鋁五擴散到鐵來形成鐵三鋁基體。所有反應在攝氏 1400 度完成。第二類型，氧化鎂鐵三鋁基金屬基複合材料透過燒結鐵、鋁、鎂和氧化鋁的粉末混合物被合成出來。在攝氏 480 度的第一步燒結當中，含有鐵、鐵二鋁五和氧化鎂的碎裂樣品被獲得。產物經過研磨和壓制後，第二步燒結產生鐵三鋁基。爲避免氧化鎂在鐵三鋁基體的分解，燒結溫度被限制在攝氏 1000 度。相似地，第三類型，鎂鋁尖晶石鐵三鋁基金屬基複合材料透過減少鎂的相對份量被合成出來。在第二步燒結當中，剩餘的氧化鋁和氧化鎂反應形成鎂鋁尖晶石。氧化鎂和鎂鋁尖晶石鐵三鋁基金屬基複合材料的密度分別爲理論密度的 95%和 98%，維氏硬度值分別爲 143 和 184。

鋁基金屬基複合材料透過燒結鋁和四氧化三鐵的粉末混合物被合成出來。鋁和四氧化三鐵的置換反應在攝氏 1000 度發生，得出含有氧化鋁顆粒的過共晶成份的鋁鐵液相。液相以不同的途徑冷卻至室溫，即爐冷卻和氯化鈉溶液淬火。在爐冷卻的樣品中，長度逾數百毫米的先共晶鋁三鐵板塊、板塊狀的離散共晶鋁三

鐵和氧化鋁顆粒在鋁基體中被發現。在從攝氏 700 度淬火的樣品中，液相以亞共晶的方式固化而且形成鋁晶枝。晶枝間距爲數微米。鋁和鋁六鐵的共晶體在晶枝間的區域形成。在從攝氏 900 度淬火的樣品中，先共晶鋁三鐵相的尺寸縮小至數十微米，富鐵液相以共晶的方式固化而且形成鋁和鋁六鐵的共晶體，而欠鐵液相以亞共晶的方式固化而且形成類似從攝氏 700 度淬火的樣品的晶枝結構。

Acknowledgement

I would like to express my sincere gratitude to my supervisor, Prof. D. H. L. Ng for his patient guidance throughout my M. Phil study. My supervisor not only gave me suggestions on my research works, but also showed me the professionalism and passion of being a scholar. Working in his research team have enriched my knowledge in materials science and improved my analytical skills. Also, it gave me a precious chance to meet people all over the world, which enhanced my communication skills and broaden my horizon. I think such a fruitful experience will benefit me to face difficulties and challenges in the future.

I would like to thank Dr. C. J. Deng, Dr. P. Yu, Dr. C. D. Qin, Dr. Y. Y. Xi, Dr. R. Wu and Dr. F. L. Kwong for their advices and assistances on my research. I also thank Mr. S. K. Li and Mr. M. H. Yeung for their relentless efforts to provide me technical supports.

It is my pleasure to work with my groupmates, Mr. M. Y. Yau, Mr. C. K. Kwok, Mr. C. Y. To, Ms. Y. Wang, Ms. L. Y. Cheung, Ms. W. M. Hon, Ms. T. K. Li, Ms. W. C. Tang, Mr. J. T. Zhu, Mr. K. C. Li and Mr. H. C. Yeung. I have gained a lot of supports and encouragements from them during my research life.

Finally, I would express my gratitude to my family. They all understand the commitment I have made to my work. Their support and care free me up to focus on my works and our great relationship gives me driving force to succeed.

Table of contents

List of tables

Page

List of figures

Page

Chapter 1 Introduction

1.1. Metal matrix composites (MMCs)

1.1.1. Introduction

A composite is defined as a material containing two or more integrated constituents to give a combination of properties that cannot be attained in the original materials when they are not combined. [1] As the name implies, a MMC is composed of ductile metal as the matrix in which the reinforcements are distributed. In general, they possess higher service temperatures than their monolithic metal counterparts. Furthermore, the reinforcements may improve specific stiffness, specific strength, abrasion resistance, creep resistance, thermal conductivity and dimensional stability. [2-5] By properly choosing matrix and reinforcements, the resulting properties of a MMC can be tailored for advanced structural, automotive, aerospace, electronic, thermal and wear applications.

1.1.2. Matrix materials

Alloys of aluminum, magnesium, titanium as well as some intermetallic compounds (IMCs) with considerable ductility and toughness can be employed as matrix materials. [6] A metallic material can exhibit a wide range of readily controllable properties through appropriate selection of alloy composition and processing method. The extensive use of metallic alloys in composite engineering is not only due to their strength and toughness, but also the simplicity and low cost of fabrication.

The choice of a matrix alloy for an MMC depends on several factors. The most important one is whether the composite is to be continuously or discontinuously reinforced. In case of continuously reinforced MMCs, the majority of the load is

transferred to the continuous fibers and hence the strength of composite mainly depends on the strength of fiber. The primary roles of the matrix are to provide effective transfer of load to the fibers and to prevent crack propagation when fiber failure occurs. On this basis, lower strength, more ductile and tougher matrix alloys may be utilized in continuously reinforced MMCs. For discontinuously reinforced MMCs, the matrix may govern the composite strength. Then, the matrix alloy with higher strength may be required.

Other considerations in the choice of the matrix include potential matrix/reinforcement reactions, either during processing or in service, which might cause degradation in performance; thermal stress due to thermal expansion mismatch between the matrix and reinforcement; and the influence of matrix fatigue behavior on the cyclic response of the composite. [8]

1.1.3. Reinforcements

Reinforcements in MMCs are secondary phases added to metallic matrix that result in some net property improvement. Generally, most reinforcements are ceramics such as oxides, nitrides and carbides, which are characterized by their superior strength and stiffness at both ambient and elevated temperatures.

The reinforcement may be in the form of particulates, both continuous and discontinuous fibers, and whiskers as shown in Fig. 1.1; concentrations normally range between 10 and 60 vol%. Continuous fiber materials include carbon, silicon carbide, boron, alumina, and the refractory metals. On the other hand, discontinuous reinforcements consist primarily of silicon carbide whiskers, chopped fibers of alumina and carbon, and particulates of silicon carbide and alumina. Continuously reinforced MMCs display enhanced strength along the fiber direction while discontinuously reinforced MMCs display more isotropic characteristics.

The role of the reinforcement depends on its type in the MMCs. In particulate

and whisker reinforced MMCs, the matrix acts as the major load bearing part while the reinforcements strengthen the composite by preventing matrix deformation. In continuous fiber reinforced MMCs, the reinforcement is the principal load bearing part while the matrix serves to bond the reinforcement and distribute the load. Typically, reinforcement increases the strength and hardness of MMCs.

1.1.4. Fabrication techniques

Nowadays, there are many processes for fabricating MMCs. The choice of the process is dictated by many factors, the most important ones are:

- Preservation of reinforcement strength
- Minimization of reinforcement damage
- Promotion of wetting between the matrix and reinforcement and uniform distribution of reinforcement

In general, the conventional fabrication processes can be classified into liquid-state processes and solid-state processes. In order to further improve the properties and lower the production cost of the MMCs, many new techniques are invented and applied to the fabrication processes. In-situ technique and rapid solidification technique are the two methods which achieved prominent successes in recent research activities.

1.1.4.1. Liquid state processes

Liquid state processing is characterized by intimate interfacial contact between the molten matrix and the reinforcement which leads to strong interfacial bonding, however, it may cause the formation of a brittle interfacial layer. A majority of the commercial applications are using liquid state processing because the liquid metal is generally less expensive and easier to handle compared with powders, and the final product can be fabricated in a wide variety by casting. The most commonly used techniques of liquid state processing are describe as follows:

- Slurry casting: Liquid metal is stirred as solid reinforcements are added to the melt to produce a slurry (Fig. 1.2). Stirring continues as the melt is cooled until the metal becomes semi-solid and trap the reinforcements in a uniform manner. Further solidification then take place without addition stirring. The slurry may be transferred directly to a shape mold prior to complete solidification, or it may be allowed to solidify in billet or rod shape so that it can be reheated to slurry form for further processing. This method is widely use for industrial applications that require high production volume and low cost. [4]
- Liquid metal infiltration: This process involved holding a porous pre-form of reinforcement within a mold and infiltrating it with molten metal that flows through interstices to fill the pores and produce a MMC as shown in Fig. 1.3. Generally, the pre-form is not wetted by the molten metal and a low controlled pressure is applied during the infiltration. Once the infiltration is complete, a high pressure is applied to reduce porosity. [9] Reinforcement materials include carbon, graphite and ceramics such as oxides, carbide or nitrides. Reinforcement forms include continuous fiber, discontinuous fiber and particulate. Metals commonly used include aluminum, magnesium and copper. The volume fraction of reinforcement varies from 40 to 70 vol% in order to withstand infiltration forces while maintaining sufficient permeability. [4]

1.1.4.2. Solid state processes

Solid state processing is generally employed to obtain better mechanical properties in MMCs, especially for discontinuously reinforced MMCs. The main reason is that reinforcement agglomeration and brittle reaction product formation can be avoided effectively by these processes compared with liquid-sate processes. [9] The most popular techniques of solid-state processing are describe as follows:

- Diffusion bonding: This process is used for consolidating alternate layers of

metal foils and reinforcement to produce single or multiple-ply composites. [9] This process is schematically illustrated in Fig. 1.4. Firstly, the composite elements are assembled by layering. Then, consolidation is achieved by applying a high pressure in a direction normal to the ply surfaces and a temperature sufficient to produce atomic diffusion of the matrix alloy. This step is usually performed in a vacuum environment. This method is used extensively to fabricate Al or Ti-based MMCs reinforced with SiC, B or other fibers.

- Powder metallurgy: It is the most common method for fabricating discontinuously reinforced MMCs. In this technique, powders of the metallic matrix and reinforcement are initially mixed and fed into a mold of the desired shape. Mixing can be carried out dry or in liquid medium. Pressure is then applied to further compact the powder mixture. The compact is then sintered at a temperature which is usually below the melting point of the matrix materials but sufficiently high to cause significant solid state diffusion. [4,9] As the wastage of materials is very low and secondary machining of the products is usually not required, so that it is suitable for high volume production of parts which require irregular edges.

1.1.4.3. In-situ techniques

In conventional methods, the reinforcements are produced separately and then added into the metallic matrix during the fabrication process. The final products are usually regarded as ex-situ MMCs. The size of reinforcement depends on the prepared powder size, which is typically tens of microns.

Recently, in-situ techniques have been developed in which reinforcements are formed in the metallic matrix by chemical reaction between precursors during the fabrication process. The in-situ MMCs have the following advantages compared with the ex-situ counterparts: [9,13-15]

- The in-situ formed reinforcements are usually thermodynamic stable in the matrix
- The size of in-situ formed reinforcement is finer and the distribution in the matrix is more uniform
- The wetting between the matrix and reinforcements is better. As the reinforcements are formed freshly during the fabrication process, the reinforcement/matrix interfaces are clean which can further improve the interfacial bonding

There are several examples of MMCs fabricated from in-situ techniques: Al-Al_2O_3 composites produced from the direct melt oxidation (DIMOX) process, [16] eutectic systems based on Cr and Ta, Fe-TiC composites produced from solidification of Fe-Ti-C melts, [9] TiB_2- reinforced Al alloy produced by the exothermic dispersion (XD) process, [17] boride-reinforced Al MMCs produced by the reactive spontaneous infiltration (RSI) process using power mixtures of TiN-B or Ti-B_4C. [18-20]

1.1.4.4. Rapid solidification (RS) techniques

Solidification refers to the process of formation of solid from liquid. Rapid solidification can be defined as a cooling from the liquid state within a very short time interval (order of milliseconds). Direct quenching is the simplest and earliest method to produce high rates of solidification in material processing. The most commonly used quenching media include water, NaCl-solution, lubricating oil and liquid nitrogen, the attainable cooling rate during quenching is ~10^5 ^{o}C/s. The resulting microstructures and distribution of the phases in the final product vary drastically with the cooling rate. The high cooling rate leads to significant undercooling of the melt and can result in non-equilibrium phase transitions and meta-stable phase retentions. [21-23]

Apart from direct quenching, a number of methods have been developed to

achieve rapid solidification. They can be classified into three main categories: [21]

- Casting of melt stream (usually by chill method)
- Spray method that involve fragmentation and atomization of a melt stream into droplets
- In-situ melting followed by rapid solidification that takes place at the surface of the heat sink

RS processing offers a way to breakthrough some of the limitations of conventional processing. For instance, it permits large departure from equilibrium constitution predicted by the phase diagrams and may result in:

- Significant extension of solid solubility
- Formation of metastable phases through non-equilibrium phase transitions
- Retention of disordered crystalline structures and intermetallics

There are other microstructural effects on the final product include:

- Changes in the shape and size of the phases
- Refinement of grain sizes
- Reduction of dendritic arm spacings

Due to the aforementioned compositional and structural differences, the materials produced by RS processes exhibit some special properties compared with traditional counterparts. In general, their hardness, ductilities, tensile strengths and high-temperature performances will be improved. [24] Therefore, more and more RS products are now available for engineering applications. For example, TiB_2 particulates-reinforced Fe-Al alloys and WC particles-reinforced Ni-based amorphous matrix composite were produced by the gas atomization technique and melt spinning technique, respectively. [21]

1.1.5. Applications

The applications of MMCs are versatile since there are many possible

combinations of metallic matrices and reinforcements. Nowadays, MMCs are gaining rapid prominence in application-driven industries, especially in automotive and aerospace sectors which have pressing demands on materials with excellent high temperature performances and wear resistance. [9]

1.1.5.1. Automotive applications

As the price of cruel oil and people's awareness of environmental protection have been rising rapidly in last decade, the automotive industry is currently facing technical challenges to improve energy efficiency and reduce vehicle emissions. Al-base and Mg-based MMCs are particularly promising materials because they can reduce the weight of the vehicle without sacrificing the strength, most importantly, they are cost effective. One of the important applications of MMCs is diesel piston crowns. It involves incorporation of short fibers of Al_2O_3 or Al_2O_3+SiO_2 in the crown of the piston. The replacement of nickel cast iron in conventional engine by fiber-reinforced Al-based MMC results in lighter, more abrasion-resistance and cheaper product. [8]

1.1.5.2. Aerospace applications

In this category, low density and other desirable features such as tailored thermal expansion and conductivity as well as high stiffness and strength are the main driving forces of using MMCs. Performance rather than cost is the dominant factor. [8] For example, MMCs find important applications in components for rockets or aircraft engines. Superalloys reinforced with metal fibers such as tungsten or ceramic fiber such as SiC or B_4N maintain their strength at high temperature, when permit engines to operate with better efficiency. Also, Ti-based MMCs reinforced with SiC fibers are widely used for turbine blades and disk. [1]

1.2. MMCs in this work

1.2.1. Metal matrices

1.2.1.1. Fe matrix

Iron is the fourth most abundant element on Earth and is the most common one in commercial metal products. It is a grayish metal which melts at 1525°C and boils at 2450°C. It has density of 7.85 g/cm^3 and very ductile when pure. It forms carbonates, chlorides, oxides, sulfides and other compounds. It oxidizes easily and is also attacked by many acids. Because pure iron is allotropic, it can exist as a solid in two different crystal forms. Up to 910°C, it has a body-centered cubic (BCC) structure and is identified as alpha (α) iron. Between 910 and 1400°C, the crystal structure is face-centered cubic (FCC) and is known as gamma (γ) iron. At 1400°C and up to its melting point, the structure becomes BCC again. The last form is called delta (δ) iron. The transformation from one allotropic from to another is reversible. [25-26]

Iron is the most used of all the metals, comprising over 90% of all the metal tonnage produced worldwide. Its combination of low cost and high tensile strength (1380 MPa) makes it indispensable in structural applications. Moreover, alpha (α) iron is a ferromagnetic material with magnetic properties such as high saturation magnetization (218 emu/g) and small coercive field (0.9 Oersted). It can be used as soft magnet which has applications such as cores for electromagnet, electric motors, transformers and generators. [1] However, the electrical resistance of pure iron is low that it is unsuitable for use in alternating-current (AC) magnetic circuits. Addition of small amount of aluminum (<8 wt%) to iron can increase electrical resistance and oxidation resistance. [26]

1.2.1.2. Fe_3Al matrix

Intermetallics refer to compounds of metals whose crystal structures are different from those of the constituent metals, and thus intermetallic phases and ordered alloys

are included. [28] Stoichiometric intermetallics have a fixed composition, while nonstoichiometric intermetallics have a range of composition and are sometimes called intermediate solid solutions. Some intermetallics possess ordered crystal structure in which the different atoms occupy specific rather than random lattice sites. [1]

The Al-Fe intermetallics are known as iron aluminides. There are two major types of iron aluminides, they are Fe_3Al and FeAl. Both have excellent oxidation and corrosion resistances because they form protective oxide film on the surface at elevated temperature. They are also low in cost and have low density and good strength. Their main drawbacks are poor ductility and brittle fracture at ambient temperatures and poor strength and creep resistance above 650°C. These compounds are being investigated as a potential replacement for stainless steels in selected applications in chemical, petroleum and coal industries. [25]

With reference to the Fe-Al phase diagram (Fig. 1.5), Fe_3Al is formed on cooling by ordering reactions that transform the BCC disordered solid solution (stable above 800°C) first into FeAl phase (stable between 800 to 550°C) and then into Fe_3Al. It is a nonstoichiometric intermetallic which can contain 24 to 33 at% Al at 400°C. It has ordered BCC crystal structure, namely, $D0_3$ structure (Fig. 1.6). It is now being considered for structural applications since it not only shows a comparable strength with iron alloys, but also has a high corrosion resistance in oxidizing and sulfidizing environments. Besides, it shows an outstanding magnetic permeability which makes it use useful as a magnetic materials. The magnetic properties can be further improved by partially substituting Al by Si which does not change the crystal structure. The Sudust alloys which are based on $Fe_3(Al,Si)$ have been widely used as magnetic head materials in magnetic recorders. [28]

1.2.1.3. Al matrix

Aluminum is the third most abundant element on the earth next to oxygen and silicon. It was discovered in 1727, but was obtained only in small amount until it was reduced electrolytically from bauxite (aluminum oxide) in 1885. Pure aluminum is a white metal with bluish tinge which melts at 660°C and boils at 2519°C. It has density of 2.69 g/cm^3 and tensile strength of 572 MPa, with electrical and thermal conductivities about two thirds that of copper. It is non-magnetic and has a FCC structure. It resists corrosion in many environments as a result of the presence of a thin aluminum oxide film. [25-26]

Pure aluminum can be used for a wide range of applications, including beverage cans, household appliances, electrical power transmission equipments and electronic components. However, pure aluminum is soft and lacks strength compared with those of iron for structural applications. Therefore, aluminum is usually alloyed with various elements such as iron, copper, magnesium, silicon or manganese to improve its mechanical properties. An alternative is to incorporate reinforcements such as borides, carbides, oxides or intermetallics into aluminum resulting in Al-base MMCs. [27]

1.2.2. Reinforcements

1.2.2.1. $FeAl_2O_4$

$FeAl_2O_4$ is commonly called hercynite, an iron aluminum oxide mineral of the spinel group, is a relatively rare mineral and has been little studied. It is a greenish gray mineral with melting point of 1780°C. It has a density of 4.3 g/cm^3 and Mohs hardness of 7.5. [30-32]

The unit cell of $FeAl_2O_4$ with an ideal spinel structure is illustrated in Fig. 1.7, where one eighth of the tetrahedral sites are occupied by Fe^{2+} cations and one half of the octahedral sites are occupied by Al^{3+} cations. As the magnetic moment of each

Fe^{2+} cation is 4 μ_B, there is a resultant moment of 32 μ_B per unit cell which is due to the eight Fe^{2+} cations. The lattice parameter of the unit cell is 8.15 Å and so the saturation magnetization is calculated to be 123 emu/g, which is higher than other magnetic ceramics such as magnetite (92 emu/g). [33] Hence, $FeAl_2O_4$ can be used in magnetic applications. However, the saturation magnetization can vary drastically with the deviation of stoichiometric ratio and the degree of inversion of the spinel structure.

1.2.2.2. Al_2O_3

Al_2O_3 is commonly called alumina. The natural crystalline mineral is called corundum. It is the most widely used oxide-type ceramic because it is plentiful, low in cost and better than most oxides in mechanical properties. Alpha (α) alumina with rhombohedral crystal structure is the most common form as it is thermodynamically stable. It melts at 2054°C and boils at ~3000°C. It has density of 3.98 g/cm^3, tensile strength of over 200 MPa and Mohs hardness of 9. It also exhibits high electrical resistance and dielectric strength, and is resistant to a wide variety of chemicals and is unaffected by air, water vapor and sulfurous atmospheres. Besides being used as electrical insulators and refractories, its high hardness and wear resistance make it suitable for abrasives and reinforcements in composites. [25, 29]

1.2.2.3. MgO

MgO is commonly called periclase. It melts at 2800°C and boils at 3600°C. It has FCC crystal structure with density of 3.58 g/cm^3, tensile strength of 96 MPa and Mohs hardness of 5.5. Refractory industry consumes a lot of MgO due to its extraordinary high melting point. Heating unit insulation is another major application of MgO as it exhibits good thermal and electrical resistance at elevated temperatures. [26,34-35] Recently, MgO is also being used as reinforcement in superconducting composites. [36]

1.2.2.4. $MgAl_2O_4$

$MgAl_2O_4$ is commonly called spinel, a magnesium aluminum oxide mineral of the spinel group. It is a colorless mineral when no impurity is present with melting point of 2135°C. It has density of 3.6 g/cm^3 and Mohs hardness of 7.8. It is formed by solid-state reaction between MgO and Al_2O_3 and is an excellent refractory showing high resistance to attack by slags and glass. [26, 30] Due to its high hardness, it is suitable to be used as reinforcements in composites.

The unit cell of $MgAl_2O_4$ having spinel structure is similar to that of $FeAl_2O_4$, the difference is that Mg^{2+} cations instead of Fe^{2+} cations occupy the tetrahedral sites. Unlike Fe^{2+} cations in $FeAl_2O_4$, Mg^{2+} cations carry no magnetic moment. Therefore, spinel is a non-magnetic material.

1.2.2.5. Al_3Fe / Al_6Fe

With reference to the Al-rich end of the Fe-Al phase diagram (Fig. 1.5), by cooling the hypereutectic melt containing 76.6 to 99.1 at% Al below the liquidus line, Al_3Fe would form as proeutectic phase. On the contrary, by cooling the hyporeutectic melt containing over 99.1 at% Al below the liquidus line, Al dendrites would form. In both cases, the melt would reached the eutectic composition (99.1 at% Al) at 655°C after the formation of proeutectic Al_3Fe or Al dendrite, eutectic transformation then occurs and Al-Al_3Fe eutectic forms. However, non-equilibrium eutectic transformation can be achieved by rapid solidification of the melt, in which metastable Al_6Fe form instead of Al_3Fe.

Al_3Fe is also known as $Al_{13}Fe_4$. It has monoclinic crystal structure with density of 3.84 g/cm^3; [37] Al_6Fe has orthorhombic crystal structure with density of 3.43 g/cm^3. [38] Similar to other Al-Fe intermetallics, they are hard, brittle and resistant to oxidation. Hence, they can act as effective reinforcements in composite if their size and distribution are carefully controlled.

1.3. Previous works

In recent years, there are several studies on fabrications of hercynite-containing composites by displacement reactions. Botta et al., Paesano et al. and Mei et al. have synthesized Fe-$FeAl_2O_4$-Al_2O_4 composites by ball-milling of Al-Fe_3O_4 powder, arc-melting of Fe-Al_2O_3 powder and reaction sintering of Al-Fe_2O_3 powder, respectively; [33,40-45] Dong et al. have also found $FeAl_2O_4$ in the composite coating fabricated by plasma spraying of Al-Fe_2O_3 powder. [46] However, hercynite is not the major product in the above studies and method has not been developed to extract hercynite.

Fe_3Al-based MMCs are of great industrial interest and various studies have been initiated for improving the mechanical properties. Subramanian et al. have produced a Fe_3Al-based MMC reinforced by in-situ formed Al_2O_3 particles from Fe-40Al and Fe_2O_3 powders by typical powder metallurgy method, however, the densities of the final products were unsatisfactory and high-cost hot isostatic pressing (HIP) technique was required for obtaining samples with higher density. [47-48] After that, Mukherjee et al. have tried to fabricate Fe_3Al-based MMC from Fe-Al-Al_2O_3 powder mixture in order to simplify the process and lower the cost, however, mechanical smearing of powder and HIP technique were required to attain acceptable density. [47] The main problem of using elemental powders of Fe and Al to form Al-Fe intermetallic matrix is that exothermic reaction occurs between Al and Fe during the heating process, that would result in pore formation which limits the density of the final product. [48] In addition, many studies have found that the wetting between the Fe_3Al matrix and Al_2O_3 particles were poor, which may lead to debonding at the Fe_3Al/Al_2O_3 interfaces and adversely affect the mechanical properties of the MMC products. [47,49-52]

The Al-rich side of the Al-Fe system is of considerable commercial interest. The reason is that during electrolytic extraction of aluminum from bauxite, iron inevitably

contaminates the aluminum and becomes the major impurity. [53] For hypereutectic Al-Fe system, it has already been reported that stable Al_3Fe forms during equilibrium solidification. In case of rapid solidification, the eutectic point shifts to higher values of iron content such that the melt may solidify in hypoeutectic manner. Also, the formations of metastable phases such as Al_6Fe or Al_9Fe_2 become dominant instead of Al_3Fe. [53-56] Similar to most of the intermetallic compounds, Al-Fe intermetallics are hard and brittle in nature. Hence, their size and distribution would have great influence on the mechanical properties of the resulting product. For example, when they form plate-like structures within the matrix, they would act as stress concentration defects which deteriorate the tensile properties. [53] In contrast, if they are small in size and evenly distributed within the matrix, they would reinforce the matrix. Recently, there are several studies on reducing the size of Al-Fe intermetallics by rapid solidification techniques. Lee et al. [56], Seo et al. [57], Liang et al. [58], Lendvai et al.[59] and Jones et al. [60] have done that by plasma spraying, droplet emulsion, water quenching, mold casting and splat cooling techniques, respectively. An alternative method to miniaturize the Al-Fe intermetallics is the addition of elements such as manganese, magnesium, sodium or lithium. However, the formations of side products limit the development of this method. [53, 61]

1.4. Objectives and current works

In order to meet the industrial demands, the first objective of this work was to investigate simple routes to produce Al-Fe MMCs. Although there have been many studies about the fabrication of Al-Fe MMC systems by sintering of Al and Fe_3O_4, the displacement reactions between Al and Fe_3O_4 and the formations of different phases have rarely been studied. Therefore, the second objective was to clarify the reaction mechanisms and set up models of phase transformations. Furthermore, the

relationships between the sample processing, microstructures, and magnetic and mechanical properties were studied in this work.

Three types of MMC systems were studied, they were Fe-based MMC reinforced by magnetic hercynite, Fe_3Al-based MMC reinforced by Al_2O_3, MgO or $MgAl_2O_4$, and Al-based MMC reinforced by Al-Fe intermetallics and Al_2O_3. All samples were produced by the typical powder metallurgy routes which are simple and low-cost.

The Fe-based MMC containing hercynite was synthesized by sintering of an Al-Fe_3O_4 powder mixture. Hercynites were extracted from the final product by arc-melting and their values of saturation magnetization were measured.

The Fe_3Al-Al_2O_3 MMC was synthesized by sintering of a Fe-Al-Fe_3O_4 powder mixture. As the wetting between Fe_3Al matrix and Al_2O_3 particle was found to be poor, therefore, displacement reaction between Mg and Al_2O_3 was utilized to form MgO instead of Al_2O_3 in the Fe_3Al-MgO MMC. In addition, $MgAl_2O_4$ having higher hardness than MgO was used as reinforcements to further improve the mechanical properties of the MMC product.

The Al-based MMC was synthesized by sintering of an Al-Fe_3O_4 powder mixture. The displacement reactions between Al and Fe_3O_4 took place and liquid (Al, Fe) with hypereutectic composition containing Al_2O_3 particles was obtained. In order to study the effects of cooling rate on the microstructures and mechanical properties, the liquid was cooled down to room temperature by different routes, namely furnace-cooling and NaCl-solution-quenching.

1.5. Thesis layout

A general introduction of metal matrix composites (MMCs) and the background of this work have been given in this chapter. In chapter 2, the sample preparation and characterization techniques will be described. In chapter 3-5, the experimental results

of the three types of MMC systems with different metallic matrices and reinforcements will be discussed. The systems are Fe-based MMC reinforced by magnetic hercynite, Fe_3Al-based MMC reinforced by Al_2O_3, MgO or $MgAl_2O_4$, and Al-based MMC reinforced by Al-Fe intermetallics and Al_2O_3, respectively. Reaction mechanisms will be proposed and described for each system. Finally, conclusions will be made and future works will be suggested in chapter 6.

References

1. D. R. Askeland, The science and engineering of materials, PWS Publishing Company, Boston, Third edition, 1994, p. 266-267, 527-528, 556, 655-656
2. Q. C. Jiang, H. Y. Wang, B. X. Ma, Y. Wang, F. Zhao, J. Alloys Comp. 386 (2005) p. 177-181
3. L. G. Chen, S. J. Lin, S. Y. Chang, Compos. Sci. Technol. 66 (2006) p. 1793-1802
4. D. B. Miracle, Composites Sci. Tech. 65 (2005) p. 2526-2540
5. L. D. Wang, W. D. Fei, F. Zheng, D. K. Yao, Mater. Chem. Phys. 82 (2003) p. 608-612
6. W. D. Callister, Fundamentals of materials science and engineering: an interactive etext, Wiley, New York, 2001, S-163, 185-186
7. J. A. Jacobs, T. F. Kilduff, Engineering materials technology: structures, processing, properties & selection, Prentice Hall International, N. J., Second Edition, 1994, p. 433-499
8. K. K. Chawla, Composite materials: science and engineering, Springer, New York, 1998, p. 164-211
9. S. Suresh, A. Mortensen and A. Needleman, Fundamentals of metal-matrix composites, Butterworth-Heinemann, Boston, 1993, p. 2-42, 297-325
10. D. Hull and T. W. Clyne, An introduction to composite materials, Cambridge University Press, Cambridge, 1996, p. 271-293
11. K. U. Kainer, Metal matrix composites: custom-made materials for automotive and aerospace engineering, Wiley-VCH, Weinheim, 2006, p. 1-11
12. http://www.dunand.northwestern.edu/research/images/marcus1.jpg
13. P. Yu, C. J. Deng, N. G. Ma, D. H. L. Ng, J. Mater. Res. 19 (2004) p. 1187-1196

14. P. Yu, C. J. Deng, N. G. Ma, D. H. L. Ng, Mater. Lett. 58 (2004) p. 679-682
15. P. Yu, C. J. Deng, N. G. Ma, M. Y. Yau, D. H. L. Ng, Acta Mater. 51 (2003) p. 3445-3454
16. V. R. S. Murthy and B. S. Rao, J. Mater. Sci. 30 (1995) p. 3091
17. Z. Y. Ma, J. H. Li, M. Luo, X. G. Ning, Y. X. Lu, J. Bi and Y. Z. Zhang, Scripta Metall. Mater. 31 (1994) p. 635
18. E. Taheri-Nassaj, M. Kobashi and T. Choh, Scripta Mater. 34 (1996) p. 1257
19. E. Taheri-Nassaj, M. Kobashi and T. Choh, Scripta Mater. 37 (1997) p. 605
20. S. C. Tjong and Z. Y. Ma, Mater. Sci. and Eng. 29 (2000) p. 49-113
21. T. S. Srivatsan, T. S. Sudarshan and E. J. Lavernia, Prog. Mater. Sci. 39 (1995) p. 317-409
22. H. Jones, J. Mater. Sci. 19 (1984) p. 1043-1076
23. H. Jones, Mater. Sci. and Eng. A 304-306 (2001) p. 11-19
24. Rapidly-Solidified Aluminum Alloys-Status and Prospects, NMAB-368, National Academy Press, Washington DC, 1981
25. M. Schwartz, Encyclopedia of materials, parts, and finishes, CRC Press, Boca Raton, 2002, p. 37-48, 321-324, 329-330, 375, 730-731
26. D. R. Lide, CRC handbook of chemistry and physics, CRC Press, Cleveland, Ohio, 84th Edition, 2003-2004, p.4-3, 4-16, 4-17
27. http://en.wikipedia.org/wiki/Aluminum
28. G. Sauthoff, Intermetallics, VCH, Weinheim, 1995, p. 5-7, 84-87
29. http://en.wikipedia.org/wiki/Alumina
30. A. N. Winchell, Elements of optical mineralogy: an introduction to microscopic petrography, Wiley Eastern, New Delhi, 1968, p.58-89
31. http://franklin-sterlinghill.com/dunn/ch22/hercynite.stm
32. G. A. Slack, Phys. Rev. 134 (1964), p. 1268-1280

33. P. M. Botta, R. C. Mercader, E. F. Aglietti and J. M. Porto Lopez, Scr. Mater. 48 (2003) p. 1093-1098

34. http://en.wikipedia.org/wiki/MgO

35. J. F. Shackelford, W. Alexander, CRC materials science and engineering handbook, CRC Press, Boca Raton , Third edition, 2001, p. 616-619

36. P. Yang, C. M. Lieber, Science 273 (1996) p. 1836

37. P. J. Black, Acta Cryst., 8 (1955) p. 43-48

38. L. K. Walford, Acta Cryst., 18 (1965) p. 287-291

39. Binary alloy phase diagrams second edition plus updates on CD-ROM, ASM International, USA, 1996

40. P. M. Botta, P. G. Bercoff, E. F. Aglietti, H. R. Bertorello, J. M. Porto Lopez, J. Mater. Sci. 37 (2002) p. 2563-2568

41. P. M. Botta, E. F. Aglietti, J. M. Porto Lopez, Mater. Chem. Phys. 76 (2002), p. 104-109

42. P. M. Botta, E. F. Aglietti, J. M. Porto Lopez, J. Mater. Synth. Process. 8 (2000) p. 345-350

43. P. M. Botta, E. F. Aglietti, J. M. Porto Lopez, Thermo. Acta 363 (2000) p. 143-147

44. J. Mei, R. D. Halldearn and P. Xiao, Scr. Mater. 41 (1999) p. 541-548

45. Paesano Jr., C. K. Matsuda, J. B. M. da Cunha, M. A. Z. Vasconcellos, B. Hallouche and S. L. Silva, J. Magn. Magn. Mater. 264 (2003) p. 264-274

46. Y. Dong, D. Yan, J. He, X. Z. Li, W. Feng and H. Liu, Surf. Coat. Technol. 179 (2004) p. 223-228

47. S. K. Mukherjee and S. Bandyopadhyay, Composites Part B, 28B (1997) p. 45-48

48. S. Gedevanishvili and S. C. Deevi, Mater. Sci. Eng., A325 (2002) p. 163-176

49. J. H. Schneibel and S. C. Deevi, Mater. Sci. Eng., A364 (2004) p. 166-170

50. R. Subramanian, C. G. McAkmey, J. H. Schneibel, L R. Buck and P. A. Menchhofer, Mater. Sci. Eng., A254 (1998) 119-128

51. R. Subramanian, C. G. McAkmey, L R. Buck, J. H. Schneibel, Mater. Sci. Eng., A239-240 (1997) 640-646

52. S. K. Mukherjee and S. Bandyopadhyay, Mater. Sci. Eng., A202 (1995) 123-127

53. C. McL. Adams, C. W. Tan and L. M. Hogan, J. Cryst. Growth, 51 (1981) p.525-533

54. R. M. K. Young and T. W. Clyne, Scr. Metal. 15 (1981) p. 1211-1216

55. A. Griger, V. Stefániay, E. Kovács-Csetényi and T. Turmezey, Key Eng. Mater. 44-45 (1990) p. 17-30

56. J. Lendvai, Key Eng. Mater. 44-45 (1990) p. 1-16

57. J. M. Lee, S. B. Kanf, T. Sato, H. Tezuka and A. Kamio, Mater. Sci. Eng. A343 (2003) p. 199-209

58. H. S. Seo, W. Y. Yoon, M. H. Kim, E. P. Yoon and K. H. Kim, J. Mater. Sci. 37 (2002) p. 4481-4486

59. D. Liang and H. Jones, Mater. Sci. Eng. A173 (1993) p. 109-114

60. H. Jones, Mater. Sci. Eng. 5 (1969) p.1-18

61. Z. Zhou and R. D. Li, Acta Metall. Sin. 6 (2003) p. 608-612

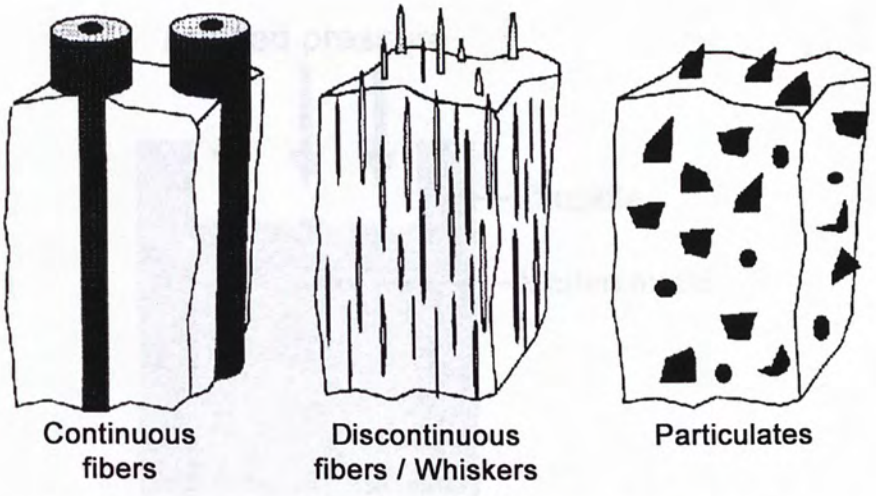

Fig. 1.1. Different types of reinforcements in composite materials. [10]

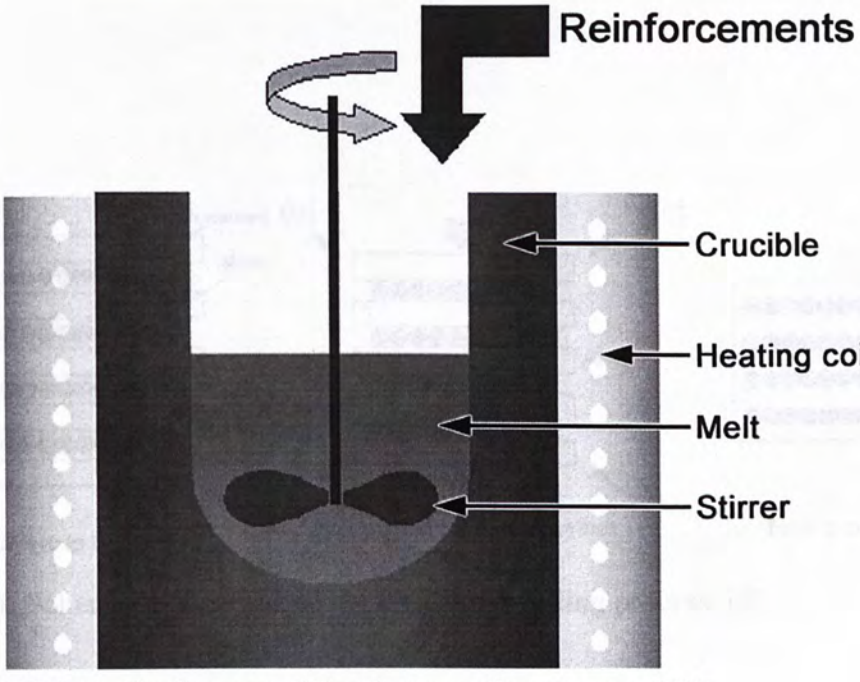

Fig. 1.2. Schematic diagram of the slurry casting process. [11]

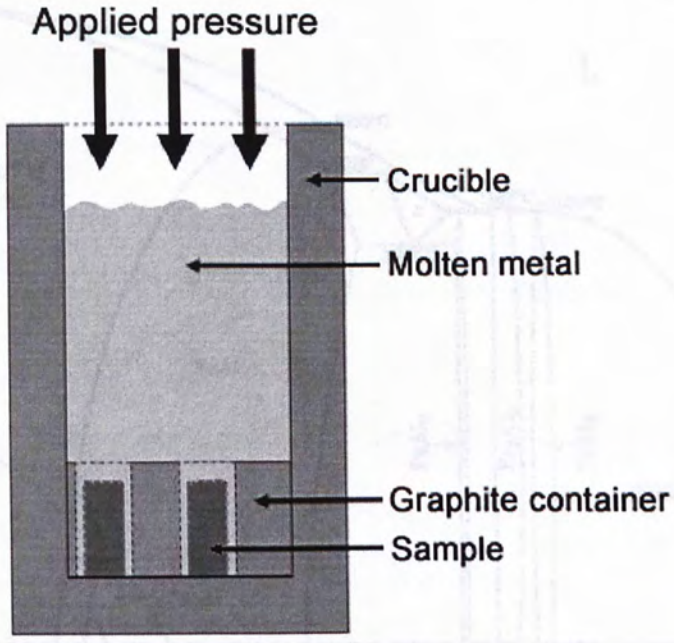

Fig. 1.3. Schematic diagram of the liquid metal infiltration process. [12]

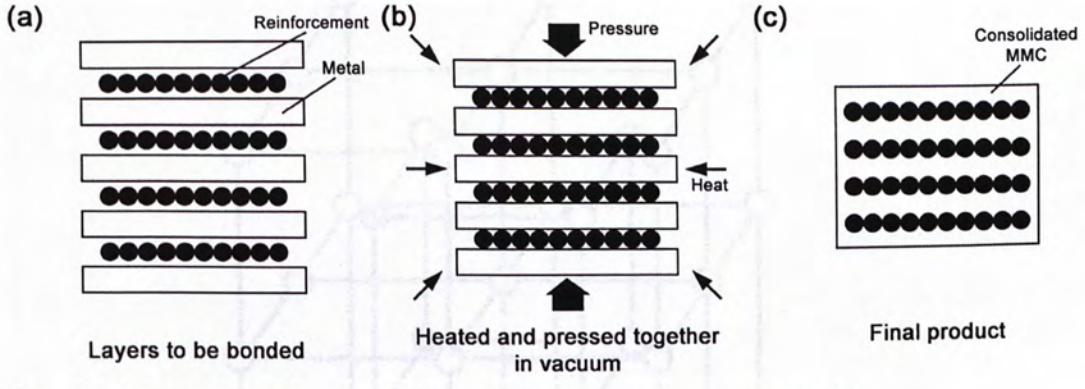

Fig. 1.4. Schematic diagrams of the diffusion bonding process. [8]

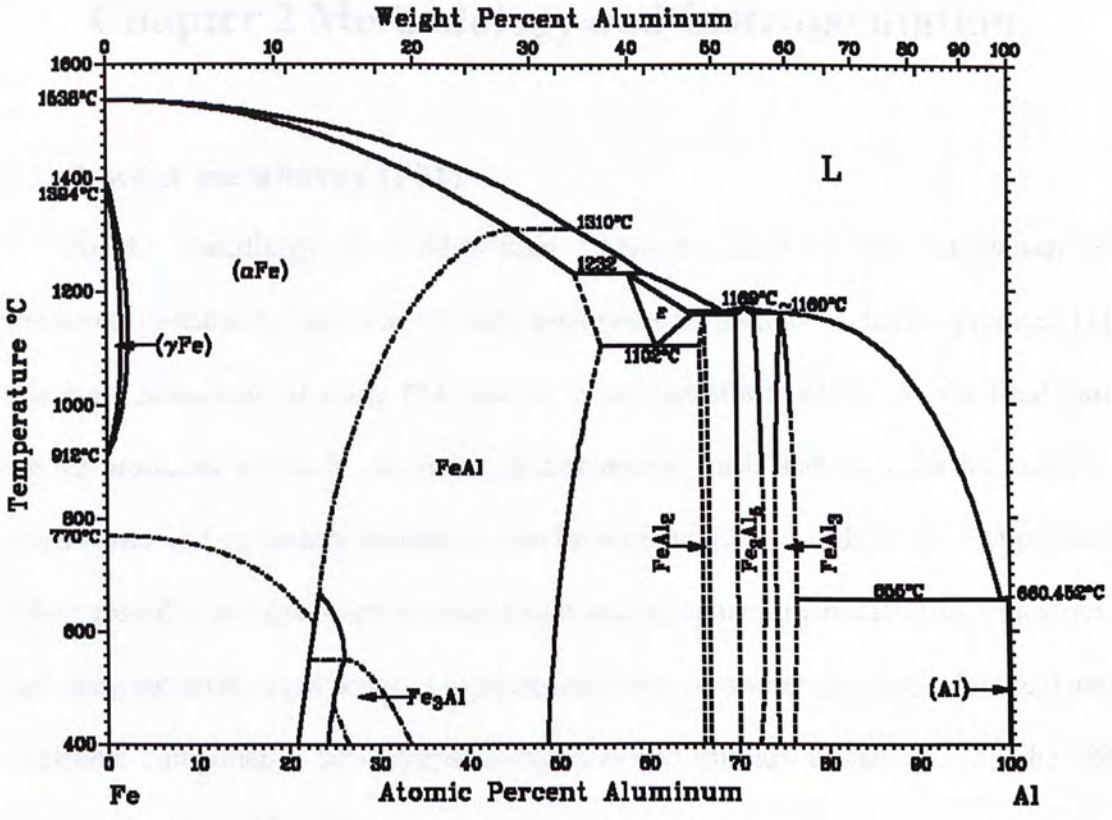

Fig. 1.5. Fe-Al phase diagram. [39]

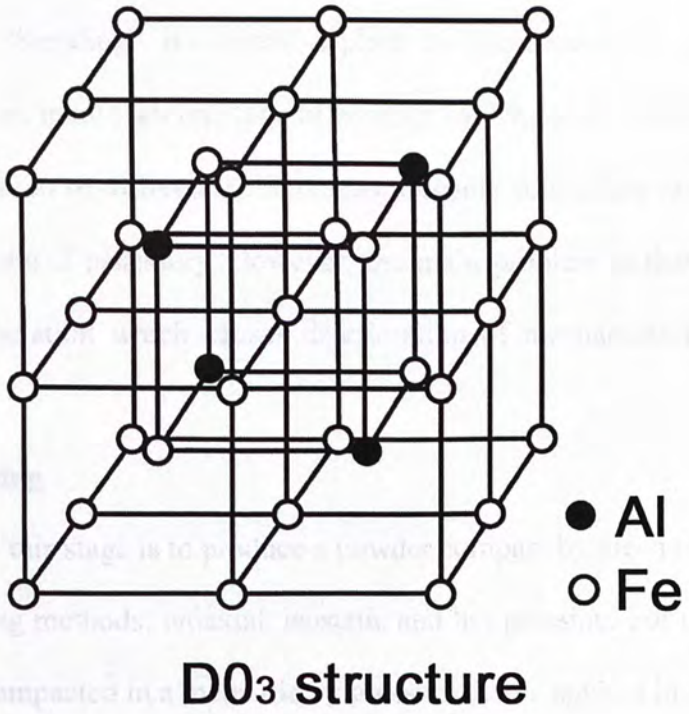

Fig. 1.6. The $D0_3$ crystal structure of Fe_3Al. [25]

Chapter 2 Methodology and Instrumentation

2.1. Powder metallurgy (PM)

Powder metallurgy is a fabrication technique involves the compaction of powdered precursors, followed by heat treatments to produce a denser product. [1] The main advantage of using PM process is its cost-effectiveness. As the final part can be produced to nearly the required dimensions, such that the material usage is much better and secondary treatments can be avoided. [2] Nowadays, the PM process is being used to produce parts in production and equipment manufacturing industries, including automotives, business machines, aircrafts, consumer products, electrical and electronic components, agricultural equipments and military ordnances. [3] The PM process consists of three major processing stages, they are mixing, compacting and sintering.

2.1.1. Mixing

The term "blending" is strictly applied to one-component operation, while "mixing" involves more than one type of powder. [4] The aim of mixing is to achieve uniform distribution of different components. Organic substances are added to act as binder or lubricant if necessary. However, the main problem is that they may leave residual contamination which causes deterioration of mechanical properties of the composite. [5]

2.1.2. Compacting

The aim of this stage is to produce a powder compact by mean of pressing. There are three pressing methods: uniaxial, isostatic and hot pressing. For uniaxial pressing, the powder is compacted in a metal die by pressure that is applied in a single direction (Fig. 2.1). The shape of the compact is limited by the configuration of the die.

However, this method is simple, fast and inexpensive. For isostatic pressing, the powder mixture is contained in a rubber envelop and the pressure is applied by a fluid isostatically. Although this method is more expensive and time-consuming, parts with more complicated shapes can be obtained compared with uniaxial pressing. For hot pressing, the pressing and heat treatment are performed simultaneously. This method is generally used for materials with very high melting points. Besides, it is utilized when pores and grain growth are undesirable. Since the die must be heated and cooled during the process, so that it is expensive to fabricate and has a short lifetime. Owning to its high cost and long processing time, its applications are limited at the present. [1]

2.1.3. Sintering

After compacting, the powder compact is heated in a protective atmosphere to cause the particles to weld together. During this process, the compact shrinks and experiences a reduction in porosity and an improvement in mechanical integrity. This heating process is called sintering. [1-2]

The sintering temperature is usually below the melting point of the metal, and the welding of the particles occurs by atomic diffusion. [2] The mechanism is illustrated in Fig. 2.2. After compacting, many powder particles touch one another. During the initial stage of sintering, necks form along the contact regions between adjacent particles and interstices of particles become pores. As sintering progresses, the pores become smaller and more spherical in shape. The reduction of total particle surface area and so the surface energy is the main driving force of sintering. [1]

In some cases where the powders have a melting range or different melting points, the sintering may be carried out at a temperature that is sufficiently high to generate a small amount of liquid phases which can assist the diffusion process. The process is referred to liquid phase sintering. [2]

2.2. Sample preparation

2.2.1. Mixing and compacting

In this work, the samples were prepared by PM technique. Reactant powders with calculated ratios were weighed with an electronic balance. The powders were then mixed and ground for ~30 min in a mortar to ensure uniform distribution. The powder mixtures were put into a 10 mm diameter steel die and cold-pressed under 1200 MPa for 10 min to form compacts with diameter of 10 mm and thickness of ~3 mm. The pressure was applied by the SPX Power Team hydraulic press.

2.2.2. Tube furnace sintering

After compacting, the samples were placed on alumina boats in the middle of an alumina tube and before the entire system was inserted into a furnace. The sintering temperatures were set according to the results of the DTA/DSC curves of the green samples and the sintering duration ranged from 1 to 6 hours. When sintering sample at temperatures lower than 1200°C, the CARBOLITE CTF12/65/550 tube furnace was used; for temperatures higher than 1200°C, the THERMOLYNE F59340CM-33 tube furnace was used. Before the heating process, the alumina tube was evacuated with a rotary pump and purged with 99.995% purity argon gas and the process was repeated two times. During sintering, argon gas was allowed to flow into one end of the alumina tube and flow out from another end, and atmospheric pressure was maintained in the system. The aims of using the argon atmosphere were:

- To prevent reactions between samples and components in the ambient such as oxygen, nitrogen and water vapor
- To prevent accumulation of vapor or gaseous products

For furnace cooling, the samples were cooled to room temperature inside the furnace with the power turned off; for rapid cooling, one end of the alumina tube was opened and the sample inside was quickly pulled out and then quenched with

saturated NaCl-solution.

2.2.3. Arc melting

Apart from tube furnace sintering, some samples were prepared by arc melting at a higher temperature. The MRF BJ-3500-VG arc melting furnace was used. It consists of a chamber, tungsten electrode, water-cooled copper stage, rotary pump and 99.995% purity argon supply.

The samples were firstly placed on the cooper stage inside the chamber. The chamber was then evacuated with the rotary pump and purged with argon gas twice. After that, a current was applied between the tungsten electrode and the copper stage and an electric arc was generated in the argon atmosphere. The arc flowing through the samples generated tremendous amount of heat by resistive heating and the attainable temperature was ~2500°C. The samples were then cooled down to room temperature on the copper stage within a few seconds. All the arc-melted sample were heated with a current of 80 A for 30 s.

2.3. Sample characterization

After cold-pressing, differential thermal analysis (DTA) or differential scanning calorimetry (DSC) were used to analyze the green samples to determine the temperatures at which the chemical reactions occurred. The samples sintered by either tube furnace or arc-melting were characterized by X-ray diffractometry (XRD), optical microcopy (OM), scanning and transmission electron microscopy (SEM and TEM) and energy dispersive X-ray spectrometry (EDS). The values of saturation magnetization (m_s) and Vickers hardness numbers (VHNs) of selected samples were measured by vibrating sample magnetometer (VSM) and microhardness tester, respectively. The flow diagram of the experimental procedures was summarized in Fig. 2.3 and the instrumentation was introduced as follows:

2.3.1. Differential thermal analysis (DTA) and differential scanning calorimetry (DSC)

The PERKIN ELMER DTA 7 differential thermal analyzer was used in this work. It is capable to reveal changes during the heating or cooling of a sample which involve evolution or absorption of energy. The sample and a chemically and thermally inert reference material (calcinated alumina) are placed on two separated alumina crucibles inside a chamber. The thermocouples under the two crucibles are connected in opposition and their temperature difference ΔT is amplified and plotted against temperature. The peak area on this plot can be converted into enthalpy change. The maximum operation temperature is ~1300°C.

The differential scanning calorimeter used in this work was PERKIN ELMER DSC 7 Pyris 1. Unlike DTA, the sample and reference crucibles have separate resistive heater. When a temperature difference develops between the two crucibles, an automatic control loop adjusts the power outputs to eliminate the difference. The difference of power output is plotted against temperature. Exothermic and endothermic changes signify enthalpy decrease and increase in the sample, respectively. Similar to the DTA curve, the positions of peaks/troughs indicate the temperatures at which physical or chemical reactions occur. In general, the sensitivity and temperature accuracy of DSC are better than those of DTA, however, the maximum operation temperature is much lower (~600°C) because the crucibles were made with aluminum.

In the DTA and DSC analyses, the samples with mass of ~10 mg were cut out from a green compact and heated up to a target temperature at a rate of 5°C/min, followed by cooling at the same rate to room temperature. During the scanning, 99.9995% purity argon gas at a rate of 25 ml/min was purged into the chamber to provide an inert atmosphere.

2.3.2. X-ray diffractometry (XRD)

The samples were ground to powder form to be analyzed with X-ray diffractometry (XRD) for phase identification. The HUBER Powder diffractometer V612365 equipped with quartz monochromator and NaI scintillation counter tube was used in this work. The X-ray was generated by the RIGAKU RU-300 rotating anode target X-ray generator. The anode material was copper that generated Cu Kα radiation with a wavelength of 1.5406Å.

In our experiments, the accelerating voltage and current of the generator were set to be 40 kV and 160 mA, respectively. The angle 2θ was scanned from 25°-80° with step size of 0.04° and was held for 5 s for each step. The angles and intensities of the obtained diffraction patterns were matched with standard patterns from JCPDS - International Centre for Diffraction Data for phase identifications.

2.3.3. Scanning electron microscopy (SEM)

SEM observations were made on the cross-sections of the samples that were diamond-polished to a finish of 0.25 μm. The LEO 1450VP scanning electron microscope was used in this work. The filament was made with tungsten and the accelerating voltage used was 15 kV. The sample chamber was pump to a high vacuum ($<10^{-5}$ torr) during the operation. A secondary electron (SE) detector (maximum resolution is up to 30 nm) and a backscattered electron (BSE) detector were installed for microstructural observations. It also equipped with an energy dispersive X-ray spectroscope (EDS) to perform elemental analyses.

2.3.4. Transmission electron microscopy (TEM)

Electron-transparent samples were prepared for TEM observations. Small pieces of samples with diameters smaller than 3 mm were mechanically cut from the bulks. Then, they were grinded with SiC papers to foils with thickness smaller than 100 μm and diamond-polished with GATAN 656 dimple grinder to a finish of 0.25 μm. The

foils were further thinned with a GATAN 691 ion miller for about 6 h until a tiny hole appeared in the center of the foil. The microstructures and crystallography of the samples were characterized by a PHILIPS CM120 transmission electron microscope. The electron source was a LaB_6 filament and the accelerating voltage used was 120 kV. Bright-field images, selected-area electron diffraction (SAED) patterns and converging beam electron diffraction (CBED) patterns were obtained. Elemental analyses were performed by using the EDS equipped on the TEM.

2.3.5. Microhardness test

The Vickers hardness test uses a 136° pyramidal diamond indenter that forms a square indent on the sample with preset test force. After the indentation with holding time of 15 s, the indenter is removed leaving an indent in the sample that appears square-shaped on the surface. The size of the indent is determined by measuring the two diagonals of the square indent with a calibrated optical microscope. The Vickers hardness number (VHN) is a function of the test force divided by the surface area of the indent. The average of the two diagonals is used in the following formula to calculate the Vickers hardness.

$$HV = 1.854 \times \text{test force} / (\text{averaged indent diagonal})^2$$

The Vickers hardness is the quotient obtained by dividing the load in kgf by the area in mm^2 of indent.

In this work, the VHNs of the samples were obtained by a BUEHLER Micromet 2103 microhardness tester at room temperature. The sample surfaces were diamond polished to a finish of 0.25 μm to give a flat surface for accurate measurements. Each value is an average of at least 5 points which were chosen randomly from the sample surfaces.

2.3.6. Vibrating sample magnetometer (VSM)

The VSM is based on Faraday's law which states that an electromotive force

(emf) will be induced in a coil when there is a change in flux linking the coil. A flux change can be generated by bringing an object with a magnetization (m) into a coil, and the amplitude of the induced emf would be directly proportional to m.

A Lakeshore 7300 vibrating sample magnetometer was used in this work and all the measurements were performed at room temperature. The sample was placed in the region between the poles of an electromagnet and was subjected to a sinusoidal motion with a known frequency. The corresponding emf was induced in stationary pickup coils. The coils were connected with a lock-in amplifier for signal amplification. By varying the current flow through the electromagnet, m of the sample was plotted against magnetic field (H) and the hysteresis loop was obtained. The values of saturation magnetization (m_s) of the samples were determined from the hysteresis loops.

References

1. W. D. Callister, Fundamentals of materials science and engineering: an interactive e-text, Wiley, New York, 2001, S-122-123, 145-148
2. G.. Dowson, Powder metallurgy: the process and its products, Bristol, 1990, p.1-10
3. M. Schwartz, Encyclopedia of materials, parts, and finishes, CRC Press, Boca Raton, 2002, p. 613-614
4. G.. S. Upadhyaya, Powder metallurgy technology, Cambridge International Science Publishing, 2002, p. 30-36
5. S. Suresh, A. Mortensen and A. Needleman, Fundamentals of metal-matrix composites, Butterworth-Heinemann, Boston, 1993, p. 23-25

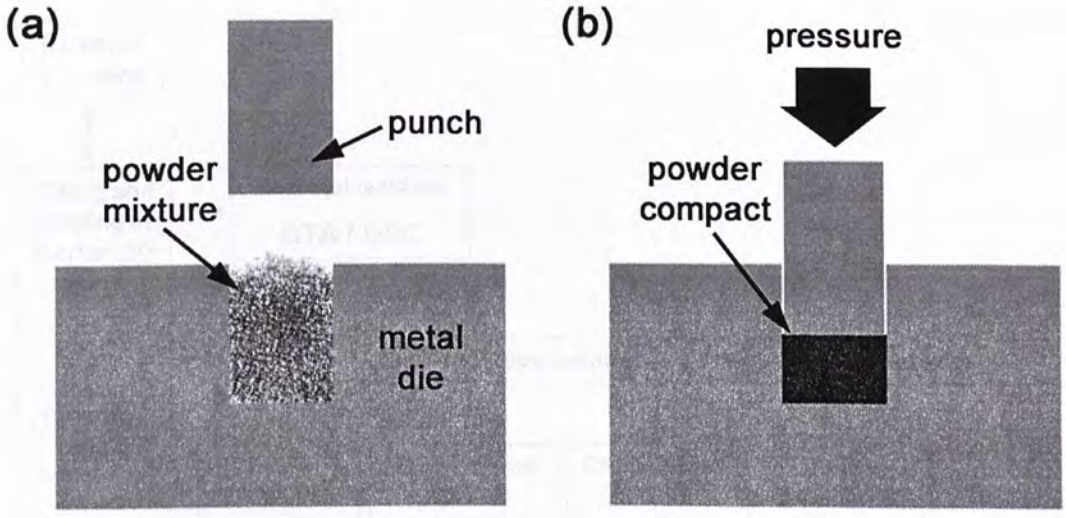

Fig. 2.1. Schematic diagram of uniaxial cold-pressing process. [2]

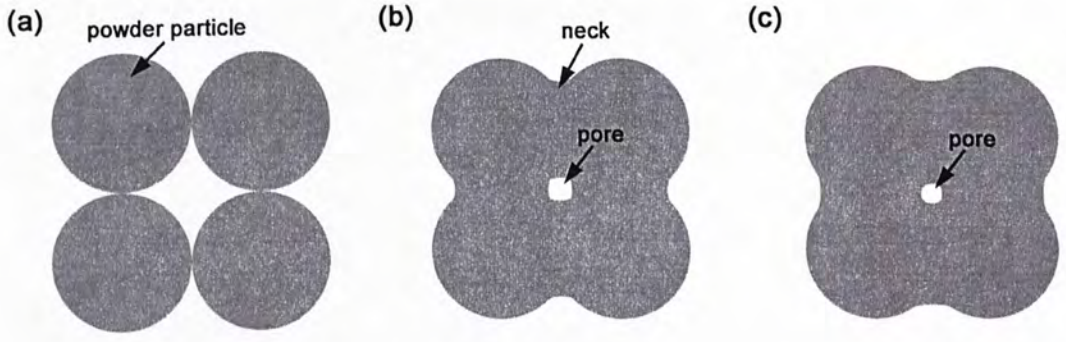

Fig. 2.2. Microstructural changes occur during sintering. (a) Powder particles after compacting. (b) Welding of particles and formation of pore. (c) Further coalescence of particles and reduction of pore size. [1]

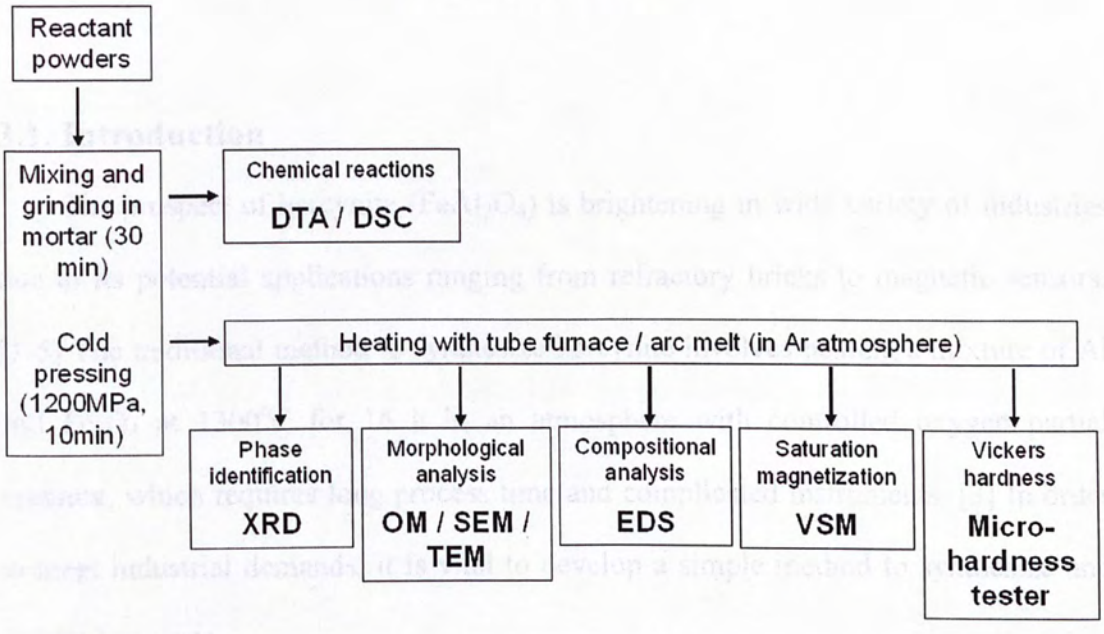

Fig. 2.3. Flow diagram of the experimental procedures.

Chapter 3 Synthesis of magnetic hercynite in Fe-based MMC

3.1. Introduction

The prospect of hercynite ($FeAl_2O_4$) is brightening in wide variety of industries due to its potential applications ranging from refractory bricks to magnetic sensors. [1-5] The traditional method to synthesize hercynite involves heating a mixture of Al and Fe_3O_4 at 1300°C for 16 h in an atmosphere with controlled oxygen partial pressure, which requires long process time and complicated instruments. [3] In order to meet industrial demands, it is vital to develop a simple method to synthesize and extract hercynite.

For hercynite with a normal spinel structure, all Fe^{2+} ions occupy the tetrahedral sites and all Al^{3+} ions occupy the octahedral sites. However, the spinel structure can be partially inverse due to a small difference in site energies, hence, Fe^{2+} ions and Al^{3+} ions can be found in octahedral sites and tetrahedral sites, respectively. [6] In addition, as a result of the formation processes, some Al^{3+} ions in the hercynite can be displaced by Fe^{3+} ions. [1] The chemical formula of hercynite in the samples is hence written as $Fe^{2+}_{1-y}Al^{3+}_{y}[Fe^{2+}_{y}Al^{3+}_{2-y-x}Fe^{3+}_{x}]O^{2-}_{4}$, where x and y depend on the deviation from the stoichiometric ratio the degree of inversion of the spinel structure, respectively. It should be noted that ions in tetrahedral sites and octahedral sites interact anti-ferromagnetically with each other, such that x and y are critically related to the net magnetic moment of the synthesized hercynite, which is an important parameter of magnetic materials.

In this work, reaction sintering was used to synthesize iron-hercynite composites form Al-Fe_3O_4 powder compact. The advantages are that both the Al and Fe_3O_4

powders are low-cost and readily available, more importantly, the following reaction occurs during sintering:

$$2Al_{(s)} + Fe_3O_{4\,(s)} \rightarrow 2Fe_{(s)} + FeAl_2O_{4\,(s)} \ldots\ldots (3)$$

where the subscript s refers to the solid form of the substance. Reaction 3 is highly exothermic (ΔH = -905 kJ/mol), [9] it makes the sintering process extremely energy-efficient. This chapter reports the fabrication and characterization of this composite. A model is proposed to explain the formation of hercynite during sintering. Extraction of hercynite by arc-melting is described. Results of saturation magnetization and Vickers hardness measurements of hercynite are also presented.

3.2. Experiments

Samples to be investigated in this work were prepared from commercial powders of aluminum (99.7% purity, <44 μm, Strem) and iron(II,III) oxide (98% purity, <5 μm, Aldrich). Al-Fe_3O_4 mixture with a molar ratio of 2:1 was cold-pressed into 3-mm-thick pellets with a diameter of 10 mm. DTA was conducted on a small piece of cut sample to determine the temperatures at which the chemical reactions between Al and Fe_3O_4 took place. After DTA, the green samples were being sintered separately in a tube furnace for 6 h in argon atmosphere with temperatures slightly above the DTA troughs/peaks appeared. In another experiment, a green sample was being arc-melted by a melting furnace in argon atmosphere. XRD was used to determine the phases in the sintered samples. Microstructural and elemental analyses were conducted by SEM and EDS.

3.3. Results and discussion

3.3.1. DTA and XRD results

The DTA curve of the Al-Fe_3O_4 sample is shown in Fig. 3.1. An endothermic trough at ~660°C corresponded to the melting of Al. Three exothermic peaks were found at 825, 1066 and 1282°C. Based on these results, the samples were being sintered separately for 6 h at 700, 900, 1100 and 1350°C before they were furnace-cooled to room temperature.

The diffraction patterns of the green sample and the sintered samples are shown in Fig. 3.2. The 2θ angles and intensities of the obtained diffraction patterns were matched with the standard patterns from JCPDS - International Centre for Diffraction Data for phase identifications. A summary of the XRD results is listed in Table 3.1. Peaks in the pattern of the green sample corresponded to those of Al and Fe_3O_4. No additional peak was found in the pattern of the sample sintered at 700°C, which implies that molten Al has not reacted with Fe_3O_4 at that temperature. In the pattern of the sample sintered at 900°C, peaks corresponded to Al, Al_2O_3 and FeO were observed. The absence of Fe_3O_4 and the appearances of Al_2O_3 and FeO indicated that all Fe_3O_4 had been reduced by Al to form Al_2O_3 and FeO. Peaks corresponded to Al_2O_3, FeO, Fe and $FeAl_2O_4$ were identified for the sample sintered at 1100°C. Thus, a reasonable claim is that FeO was further reduced by Al to form Al_2O_3 and Fe, and some Al_2O_3 reacted with FeO to form $FeAl_2O_4$. This claim would be justified in latter sessions. As expected in reaction 3, peaks corresponded to Fe and $FeAl_2O_4$ were found for the sample sintered at 1350°C, it suggests that all Al_2O_3 and FeO reacted to form $FeAl_2O_4$.

The sample prepared by arc-melting contained a shinny and a dark portion, the corresponding diffraction patterns are shown in Fig. 3.3. Pattern of the shinny portion corresponded to Fe, and $FeAl_2O_4$ peaks were detected in the pattern taken from the dark portion.

3.2.2. SEM and EDS results

3.2.2.1. Green sample

The SEM micrograph of the green Al-Fe_3O_4 compact is shown in Fig. 3.4. The dark grains were Al, having a size distribution from a few to tens of microns. They were surrounded by the Fe_3O_4 particles with size smaller than 1 μm.

3.2.2.2. Sample sintered at 700°C

Fig. 3.5a is a SEM micrograph that shows the microstructure of the sample sintered at 700°C. The size and distribution of the Al grains in the Fe_3O_4 matrix are similar to those observed in the green sample (Fig. 3.4) and no reaction product was observed. However, as the Al melted beyond 660°C, some Fe_3O_4 particles migrated into the peripheries of the Al.

3.2.2.3. Sample sintered at 900°C

Fig. 3.5b shows the SEM micrograph of the sample sintered at 900°C. The EDS analyses revealed that the matrix was composed of ~50 at% Fe and ~50 at% O, the dark grains mainly consisted of Al while the white particles inside with size smaller than 10 μm contained ~40 at% Al and ~60 at% O. With reference to the XRD results (Fig. 3.3), it is apparent that the matrix, dark grains and white particles are FeO, Al and Al_2O_3 respectively. Evidently, Al reacted with Fe_3O_4 to form Al_2O_3 and FeO at ~900°C.

3.2.2.4. Sample sintered at 1100°C

The SEM micrograph of the sample sintered at 1100°C is shown in Fig. 3.5c. It is noticeable that the Al grains disappeared and voids with size ~tens of microns were formed in the FeO matrix. Two layers of reaction products with thickness of several microns have deposited on the wall of the void. According to the EDS results, the white layer was identified to be Al_2O_3 as it consisted of ~40 at% Al and ~60 at% O. For the dark layer, EDS analyses revealed that it was $Fe_{1+x}Al_{2-x}O_4$ ($0.24<x<0.35$). Furthermore, networks of bright phase were found in the FeO matrix. EDS results

also indicated that it consisted of Fe with a few at% O. It is reasonable to deduce that it is Fe with a little amount of dissolved FeO. From these results, it can be confirmed that Al further reduced FeO to form Al_2O_3 and Fe until all Al was used up, and it was accompanied by the formation of small amount of hercynite.

3.2.2.5. Sample sintered at 1300°C

Fig. 3.5d is a SEM micrograph that shows the microstructure of the sample sintered at 1350°C. Voids with size ~tens of microns were found. A dark layer of reaction product with thickness ranging from several to tens of microns around the voids was found to be $Fe_{1+x}Al_{2-x}O_4$ ($0.47<x<0.52$) by EDS analyses (Fig. 3.6). The EDS results also revealed that the bright phase was Fe. Comparing it with the 1100°C-sintered sample (Fig. 3.5c), the Al_2O_3 layer deposited on the wall of the void and the FeO phases in the matrix disappeared. On the contrary, the thickness of $Fe_{1+x}Al_{2-x}O_4$ layer increased and Fe replaced FeO to form the matrix. These results suggest that chemical reaction between Al_2O_3 and FeO have taken place to form hercynite. It is noticeable that the hercynite was further deviated from the stoichiometric ratio as the sintering temperature increased from 1100 to 1350°C.

3.2.2.6. Arc-melted sample

The photograph of the arc-melted sample is shown in Fig. 3.7a. During the melting process, ignition of the pellet by the arc was observed due to the occurrence of reaction 3, which generated tremendous amount of heat. Moreover, the molten sample segregated into two portions readily at elevated temperature. From the photograph (Fig. 3.7a), it can be seen that the solidified product consists of a shinny and a dark portions. With reference to the XRD results (Fig. 3.3), they corresponded to iron and hercynite respectively. The EDS analyses revealed that the formula of hercynite was $Fe_{1+x}Al_{2-x}O_4$ ($0.39<x<0.43$). Arc-melting of Al-Fe_3O_4 sample will provide a simple mean to extract hercynite.

3.3.3. Reaction mechanisms

Taking all the results of DTA, XRD and those from the microstructural and elemental analyses into consideration, it is possible to postulate the reactions that occurred during sintering. Fig. 3.8 shows a series of schematic diagrams to illustrate the different stages of reactions and the evolution of the microstructure in the sample during sintering.

The green sample was composed of Al powders that distributed in the Fe_3O_4 matrix. When the sample was heated to the temperature where the DTA trough was located (660°C), Al powder was melted and some Fe_3O_4 particles migrated into its periphery (Fig. 3.8a). No chemical reaction was involved at this stage. As the reactants were Al and Fe_3O_4 with a ratio of 2:1, such that the melting process of Al in the sample can be described by the following equation

$$6Al_{(s)} + 3Fe_3O_{4\,(s)} \rightarrow 6Al_{(l)} + 3Fe_3O_{4\,(s)} \ldots\ldots (3.1)$$

where the subscripts s and l refer to the solid and liquid form of the substance, respectively.

When the temperature was at where the first DTA peak was located (825°C), Fe_3O_4 reacted with Al to form FeO and Al_2O_3 until all the Fe_3O_4 was consumed. The newly-formed Al_2O_3 at the Al/Fe_3O_4 interface moved towards the molten Al (Fig. 3.8b). Since no Al_2O_3 particle was found in the FeO matrix (Fig. 3.5b), it is reasonable to deduce that O atoms in the Fe_3O_4 matrix diffused towards the Al/Fe_3O_4 interface during the reaction. The reaction can be represented by the following equation

$$6Al_{(l)} + 3Fe_3O_{4\,(s)} \rightarrow 4Al_{(l)} + Al_2O_{3\,(s)} + 9FeO_{(s)} \ldots\ldots (3.2)$$

By sintering the sample with the temperature where the second DTA peak was found (1066°C), FeO further reduced by Al to form Fe and Al_2O_3. Similar to the previous stage, O atoms in the FeO matrix diffused towards the Al/FeO interface

during the reaction, as no Al_2O_3 particle was found in the FeO matrix (Fig. 3.5c). Since Al was consumed after the reaction, so that voids were left in the FeO matrix. The newly-formed Al_2O_3 and Fe deposited on the wall of the void. The reaction can be described by the following equation

$$4Al_{(l)} + Al_2O_{3\,(s)} + 9FeO_{(s)} \rightarrow 6Fe_{(s)} + 3Al_2O_{3\,(s)} + 3FeO_{(s)} \ldots\ldots (3.3)$$

This reaction was highly exothermic (ΔH = -1757 kJ/mol). [9] The heat released during the reaction initiated the reaction between Al_2O_3 and FeO to form $FeAl_2O_4$ (Fig. 3.8c). Although the Al_2O_3 layer and FeO were separated by a thin layer of iron, it is possible for the FeO to diffuse across the iron layer. This claim is supported by the EDS results, which revealed the presence of FeO in the layer of iron located between the Al_2O_3 and FeO. As the newly-formed $FeAl_2O_4$ was in contact with the iron layer, therefore, we postulated that Fe atoms in the iron layer diffused into the $FeAl_2O_4$ and displaced some of the Al atoms, which were vaporized at such a high temperature. This postulate explains the deviated stoichiometric ratio of the hercynite in the sintered sample.

When the sample was sintered at the temperature where the third DTA peak was located (1282°C), FeO acquired sufficient thermal energy to diffuse across both the iron and hercynite layers, it reached and reacted with the Al_2O_3 layer to form $FeAl_2O_4$ (Fig. 3.8d). The formation of the $FeAl_2O_4$ in the sample can be expressed by the following equation

$$6Fe_{(s)} + 3Al_2O_{3\,(s)} + 3FeO_{(s)} \rightarrow 6Fe_{(s)} + 3FeAl_2O_{4\,(s)} \ldots\ldots (3.4)$$

Thereafter, Fe atoms in the adjacent iron layer diffused into the newly-formed $FeAl_2O_4$ and caused the deviation of the stoichiometric ratio. The deviation was larger compared with that of the previous stage. This could be explained by two factors: first the increase in temperature from 1100 to 1350°C and second the heat released in the

reaction 3.4 (ΔH = -175 kJ/mol) [9]. Both factors provide more thermal energy to the system which accelerated the diffusion of Fe atoms and vaporization of Al atoms. Hence, more Al atoms in the hercynite were replaced by Fe atoms resulting in larger stoichiometic ratio deviation.

3.3.4. Thermodynamic model for the reactions

A thermodynamic model was established to calculate the enthalpy changes of reactions 3.1 to 3.4. The experimental values obtained by the DTA curve were compared with the calculated values to further study the reaction process. The analytical method suggested by Yu et al. for the Al-NiO system was utilized in this work. [7] According to this method, we plotted the enthalpies of the reactants and products in each stage of the reactions against the temperatures, their differences at the temperatures where the DTA peaks were located would be the enthalpy changes of the reactions. The enthalpy h(T) of each substance at temperature T was obtained by the following expressions [8]

$$h(T) = h(298) + \int_{298}^{T} c_p(T)dT \qquad (T < T_m)$$

$$h(T) = h(298) + \int_{298}^{T_m} c_p(T)dT + \Delta h_m + \int_{T_m}^{T} c_p(T)dT \qquad (T \geq T_m)$$

where h(298) is the enthalpy of the substance at 298K (25°C), c_p is the heat capacity at T, T_m is the melting point and Δh_m is the latent heat of fusion of the substance. By summing up the enthalpies of all substances, the total enthalpies H(T) of the reactants and the products were obtained

$$H(T) = n_1 h_1(T) + n_2 h_2(T) + \ldots$$

where n is the number of mole of each substance in the reactants or in the products.

Fig. 3.9 is the plot showing the enthalpies of the reactants and the products of the Al-Fe_3O_4 sample as functions of temperature. The thermodynamic data used in the

calculations were taken form Barin et al. [9] For the sake of simplicity, we assumed that the enthalpy of hercynite was a constant regardless of the deviation of the stoichiometric ratio. Such an assumption was based on the fact that the energy difference between Al-occupied and Fe-occupied sites is small. [10] From the plot, the enthalpy changes of reactions 3.1 to 3.4 were calculated to be 75, -988, -2051 and -204 J/g respectively. On the contrary, the enthalpy changes of the endothermic trough and the three exothermic peaks were 69, -211, -1050 and -1844 J/g respectively according to the DTA curve (Fig. 3.1). By simple calculations, the overall enthalpy change of the sample during sintering was found to be -3168 J/g by thermodynamic analysis, while the value was -3036 J/g by DTA. The agreement of the two values (error< 10%) suggested that all the reactions completed after heating to 1350°C in the DTA chamber. The DTA trough at 660°C corresponded to the reaction 3.1 (melting of Al) as the calculated and experimental enthalpies are rather close. The enthalpy changes of the first and the second DTA peaks are significantly smaller than that of the reactions 3.2 (reduction of Fe_3O_4 by Al) and 3.3 (reduction of FeO by Al) respectively, it implies that the displacement reactions had not been completed. For the third peak, the enthalpy change is much larger than that of reaction 3.4 (formation of $FeAl_2O_4$), the extra heat released can be attributed to the resumptions of the displacement reactions. During the DTA analysis, the sample was being heated at a constant rate of 5°C/min. Due to the absence of isothermal stages at the temperatures where the first and the second DTA peaks were found, there was no sufficient time for the reaction products of reactions 3.2 and 3.3 to move away from reaction interfaces, they hindered Al from further reactions with Fe_3O_4 or FeO. At the temperature where the third DTA peak was located, fluidity of Al increased such that the reaction products could move away from the interfaces and further reactions could take place.

3.3.5. Saturation magnetization

Saturation magnetizations were measured from the sample sintered at 1350°C, and from the hercynite prepared by arc-melting using a VSM at room temperature. The values obtained were m_s^f and m_s^a, where superscripts f and a refer to the samples sintered at 1350°C and prepared by arc-melting, respectively. We found that m_s^f(overall) was 70 emu/g and m_s^a(hercynite) was only 4 emu/g. With reference to reaction 3.4, the sample sintered at 1350°C contained iron and hercynite with a molar ratio of 2:1. It is known that the m_s of iron is 218 emu/g. [10] By simple calculations, m_s^f(hercynite) was found to be 3 emu/g. The m_s of hercynite $FeAl_2O_4$ with normal spinel structure is 123 emu/g. [1]

In order to explain the difference between the measured and the literature values, we first considered the x value. It was proportional to the amount of Al atoms displaced by Fe atoms. The hercynite could be expressed as $Fe^{2+}[Al^{3+}_{2-x}Fe^{3+}_x]O^{2-}_4$. The cations outside the square bracket occupied the tetrahedral sites while those inside occupied the octahedral sites. Ions in tetrahedral sites and octahedral sites interacted anti-ferromagnetically. The values of x for the hercynite in the sample sintered at 1350°C and that prepared by arc-melting were 0.50 and 0.41. The magnetic moments of Fe^{2+} and Fe^{3+} ions are 4 and 5 μ_B, respectively. The calculated values of m_s^f(hercynite) and m_s^a(hercynite) were 56 and 42 emu/g, respectively, which were much larger than the measured values. Therefore, we have to take the degree of inversion of the spinel structure y into consideration. The value of y was proportional to the number of Fe^{2+} ions exchanged their sites with Al^{3+} ions. The hercynite could be expressed as $Fe^{2+}_{1-y}Al^{3+}_y[Fe^{2+}_yAl^{3+}_{2-y-x}Fe^{3+}_x]O^{2-}_4$. By using the measured values of m_s^f(hercynite) and m_s^a(hercynite), the values of y were found to be 0.17 and 0.23 for hercynite in the sample sintered at 1350°C and that prepared by arc-melting,

respectively. Yagnik et al. have determined that the value of y for the hercynite prepared by sintering the Fe_2O_3-Al_2O_3-Fe mixture in H_2-CO_2 atmosphere was 0.23 by using Mössbauer spectroscopy, [11] which was in agreement with our calculated y values.

3.3.6. Microhardness

Hardness measurements were performed on both hercynite and iron prepared by arc-melting. The Vickers hardness numbers (VHNs) were obtained by a microhardness tester with 50gf load indenter at room temperature. Each value reported was an average of 5 points selected randomly from different positions of the sample. It is found that the VHN of the hercynite is 1108±19, and that of the iron is 144±9. The micrographs of the indents in the hercynite and iron taken by an optical microscopy are shown in Fig. 3.10. Dong et al. have reported that the VHN of hercynite was 985, [12] which was rather close to our result. It is noted that hercynite possesses very high VHN, especially among common magnetic materials such as iron, nickel, cobalt, hematite and magnetite. [13] It makes it suitable for applications in high-strength magnetic devices.

3.4. Conclusions

Three stages of reactions were identified in the sintering of the Al-Fe_3O_4 system with a molar ratio of 2:1 and the reaction mechanism was proposed. The first stage was initiated at ~900°C, in which Fe_3O_4 reacted with Al to form FeO and Al_2O_3. FeO was further reduced to form Fe and Al_2O_3 at ~1100°C in the second stage. The third stage occurred at ~1350°C where Al_2O_3 and FeO reacted to form hercynite. The final composite contained iron and hercynite. Fe atoms in the iron layer diffused into the newly-formed hercynite and displaced some Al atoms at elevated temperatures, causing the deviation from the stoichiometric ratio.

Ignition of reactants (Al and Fe_3O_4) and segregation of molten iron and hercynite were observed during the arc-melting of the green compact. It provides a simple method to extract pure hercynite.

In accordance with the thermodynamic analysis, the proposed reaction mechanism is consistent with the DTA results. It was also found that the absence of isothermal process during the DTA analysis hindered Al from further reactions with Fe_3O_4 or FeO. The displacement reactions resumed at higher temperatures due to the increased fluidity of Al.

The saturation magnetizations of hercynites obtained in this work were smaller than the literature value. This can be explained by the deviation of the stoichiometric ratio x and the degree of inversion of the spinel structure y. For the hercynite prepared by tube-furnace sintering at 1350°C, x = 0.50 and y = 0.17; for that prepared by arc-melting, x = 0.41 and y = 0.23. The hardness of hercynite was measured to be 1108.

References

1. P. M. Botta, R. C. Mercader, E. F. Aglietti and J. M. Porto Lopez, Scr. Mater. 48 (2003) p. 1093-1098
2. P. M. Botta, P. G. Bercoff, E. F. Aglietti, H. R. Bertorello, J. M. Porto Lopez, J. Mater. Sci. 37 (2002), p. 2563-2568
3. P. M. Botta, E. F. Aglietti, J. M. Porto Lopez, Mater. Chem. Phys. 76 (2002), p. 104-109
4. P. M. Botta, E. F. Aglietti, J. M. Porto Lopez, J. Mater. Synth. Process. 8 (2000) p. 345-350
5. P. M. Botta, E. F. Aglietti, J. M. Porto Lopez, Thermo. Acta 363 (2000) p. 143-147
6. Paesano Jr., C. K. Matsuda, J. B. M. da Cunha, M. A. Z. Vasconcellos, B. Hallouche and S. L. Silva, J. Magn. Magn. Mater. 264 (2003) p. 264-274
7. P. Yu, C. J. Deng, N. G. Ma, and D. H. L. Ng, J. Mater. Res. 19 (2004), p. 1187-1196
8. T. Lyman, Metallography, Structures and Phase Diagrams, Metal Handbook, Materials Park (OH), ASM International, Ohio, 8th Edition, 1973, p. 262
9. I. Barin, F. Sauert, E. Schultze-Rhonhof and W. S. Sheng, Thermochemical Data of Pure Substances, VCH, Weinheim, Federal Republic of Germany, 1989, p. 17, 48, 536, 561, 564-565
10. J. Mei, R. D. Halldearn and P. Xiao, Scr. Mater. 41 (1999), p. 541-548
11. C. M. Yagnik, H. B. Mathur, J. Phys. C: Solid State Phys. 1 (1968), p. 469-472
12. Y. Dong, D. Yan, J. He, X. Z. Li, W. Feng and H. Liu, Surf. Coat. Technol. 179 (2004) p. 223-228

13. D. R. Lide, CRC handbook of chemistry and physics, CRC Press, Cleveland, Ohio, 84th Edition, 2003-2004, p.117-125, 149-155

Table 3.1. Summary of the XRD results: phases in the Al-Fe_3O_4 green sample and the samples sintered at 700, 900, 1100 and 1350°C.

Samples	Phases					
	Al	Fe_3O_4	Al_2O_3	FeO	Fe	$FeAl_2O_4$
Green	√	√				
Sintered at 700°C	√	√				
Sintered at 900°C	√		√	√		
Sintered at 1100°C			√	√	√	√
Sintered at 1350°C					√	√

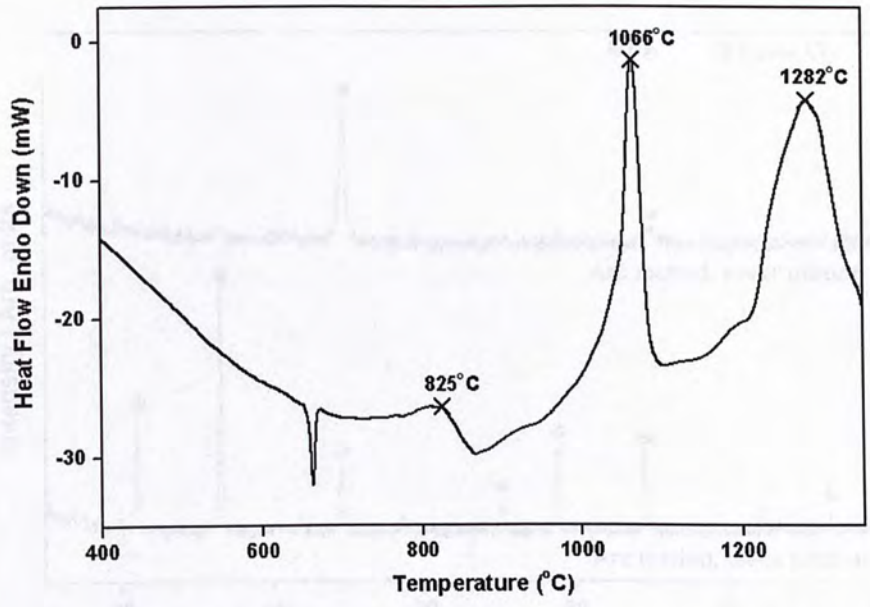

Fig. 3.1. DTA curve of the Al-Fe_3O_4 sample (molar ratio of 2:1) shows three exothermic peaks at 825, 1066 and 1282°C. The changes in enthalpy ΔH related to the three peaks are -211, -1050 and -1844 J/g, respectively.

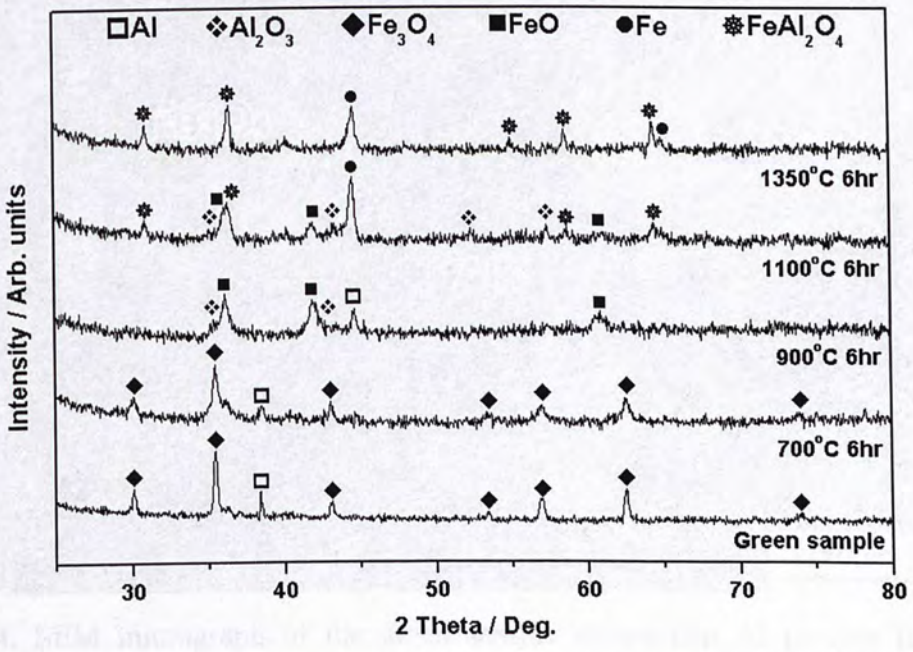

Fig. 3.2. XRD patterns of the green sample and the samples sintered at 700, 900, 1100 and 1350°C.

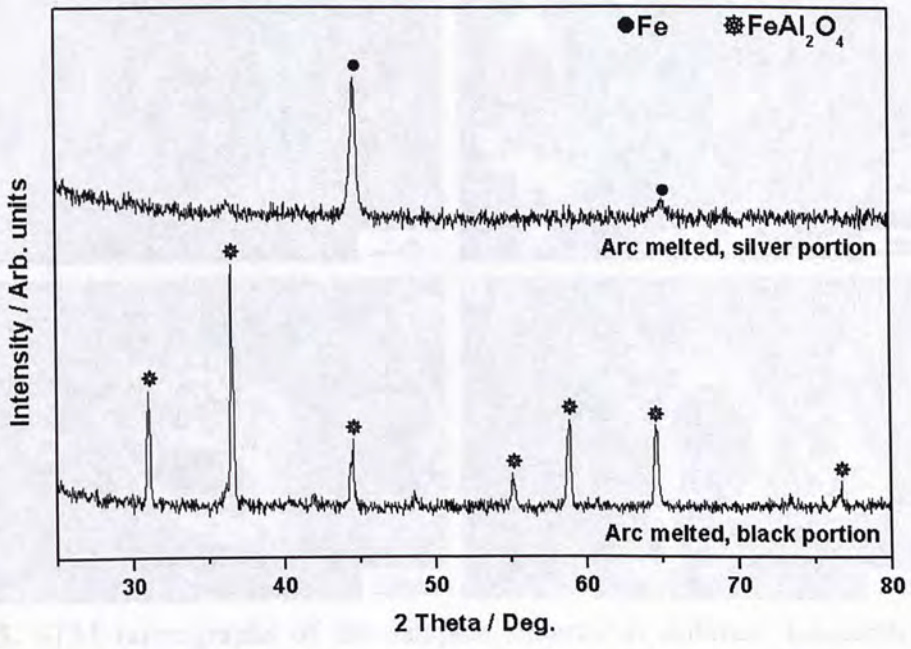

Fig. 3.3. XRD patterns of the silver and black portions of the arc-melted sample.

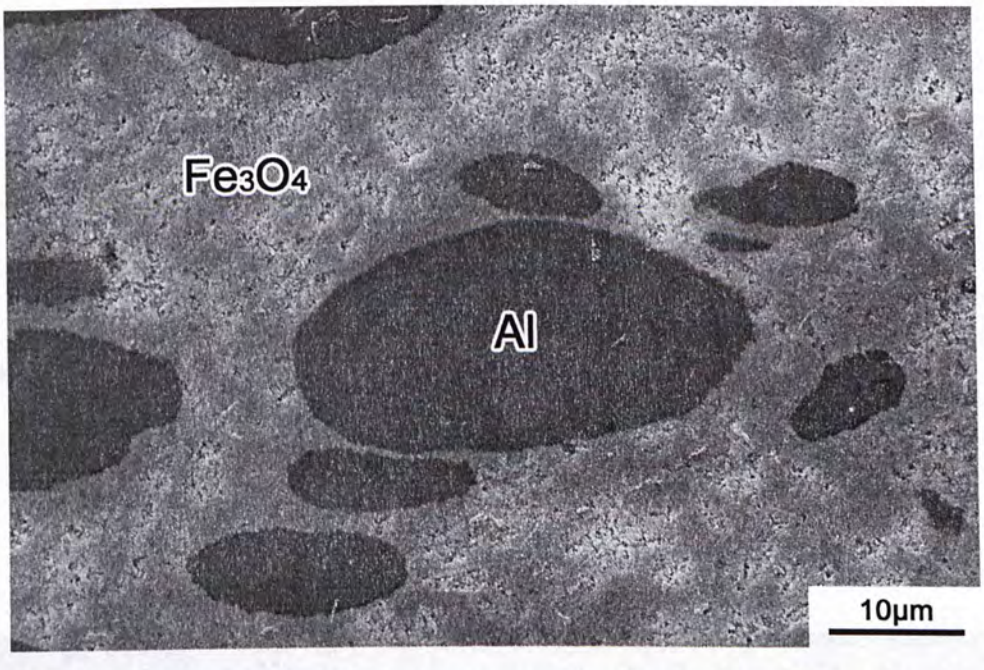

Fig. 3.4. SEM micrograph of the green sample shows that Al powder (dark) is distributed in the Fe_3O_4 matrix (bright).

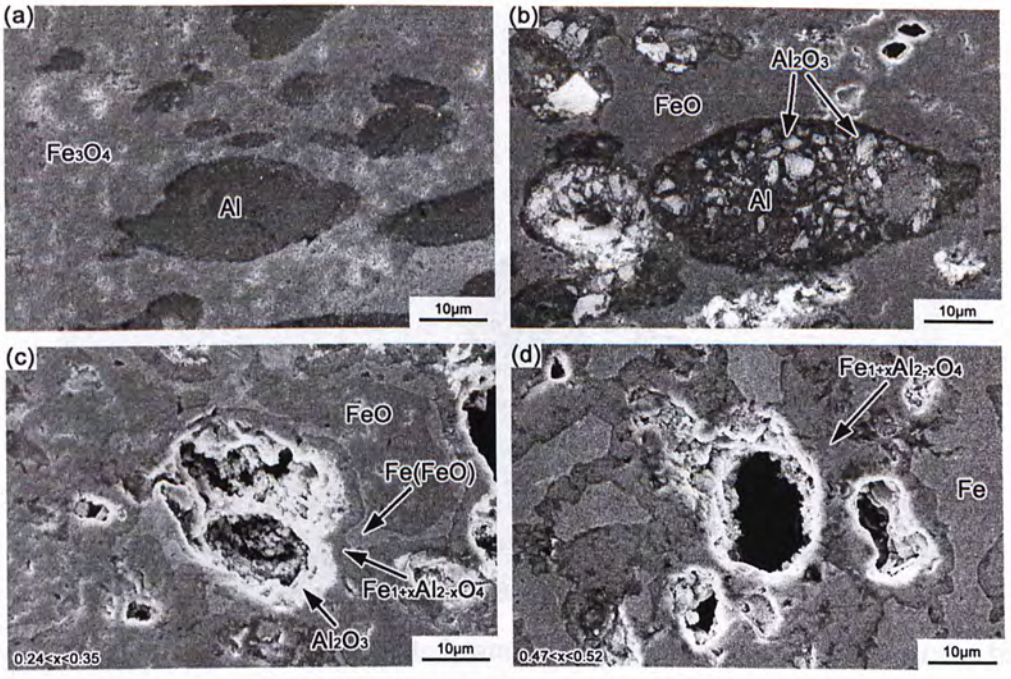

Fig. 3.5. SEM micrographs of the samples sintered at different temperatures. (a) 700°C: Al grains are distributed in the Fe_3O_4 matrix. (b) 900°C: Al_2O_3 particles are found in the Al grains. The matrix is composed of FeO. (c) 1100°C: Al_2O_3 and hercynite layers are deposited on the wall of the void. Networks of Fe(FeO) are found in the FeO matrix. (d) 1350°C: Zone surrounding the voids is hercynite. The matrix contains mainly Fe.

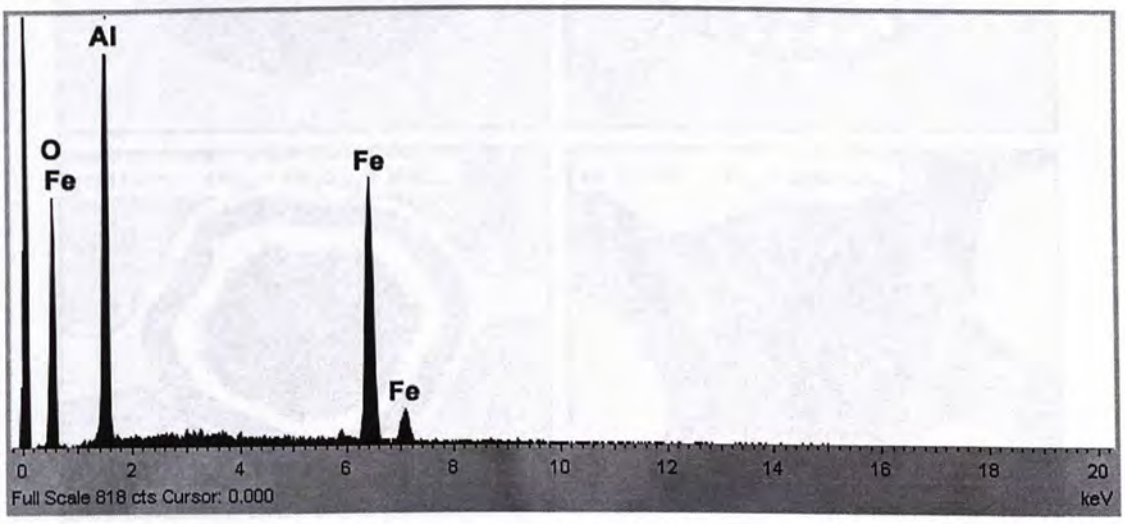

Fig. 3.6. EDS spectrum of the layer surrounding the voids of the sample sintered at 1350°C.

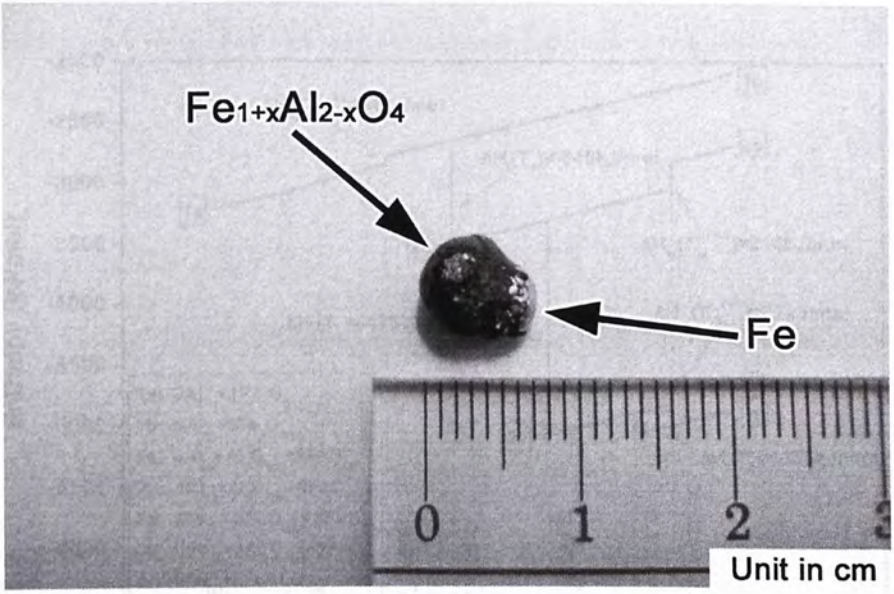

Fig. 3.7. Photograph of the arc-melted sample which consists of a silver and a black portions.

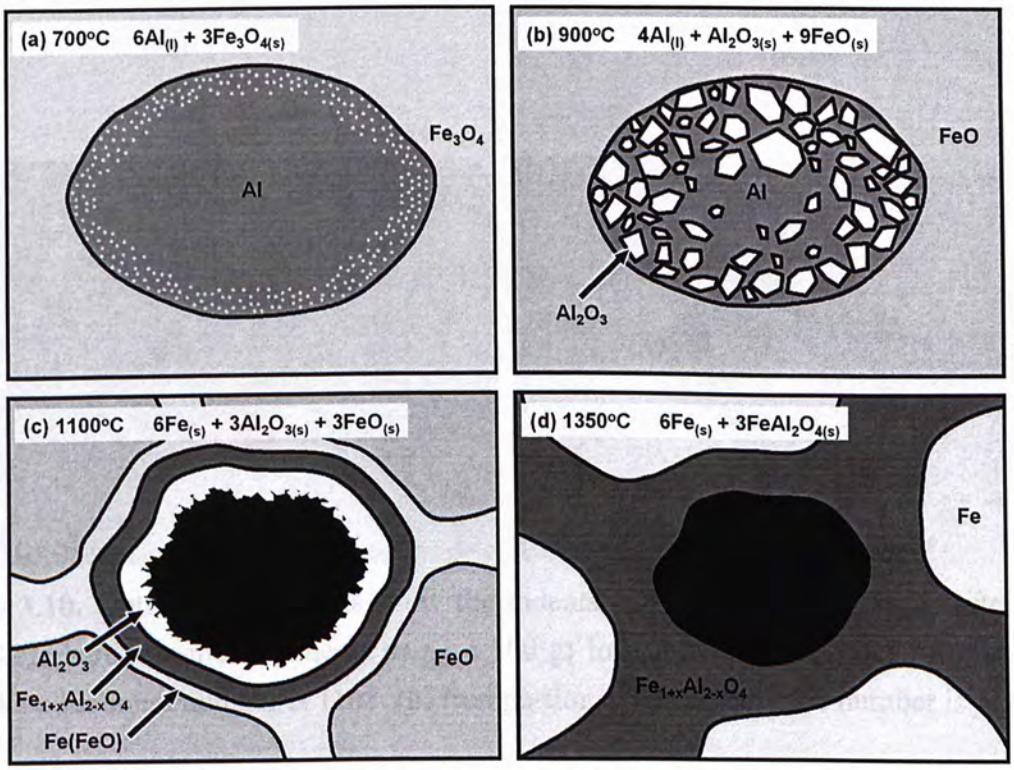

Fig. 3.8. A series of schematic diagrams illustrate the reactions in the Al-Fe_3O_4 sample as the temperature was raised from 700 to 1350°C.

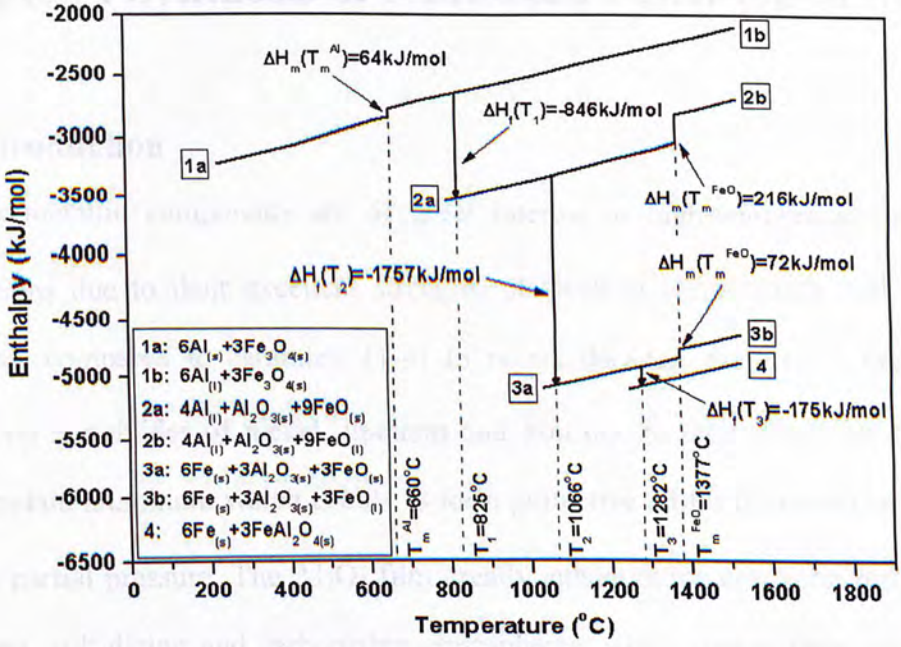

Fig. 3.9. The enthalpies of the reactants and the products of the Al-Fe_3O_4 sample as functions of temperature.

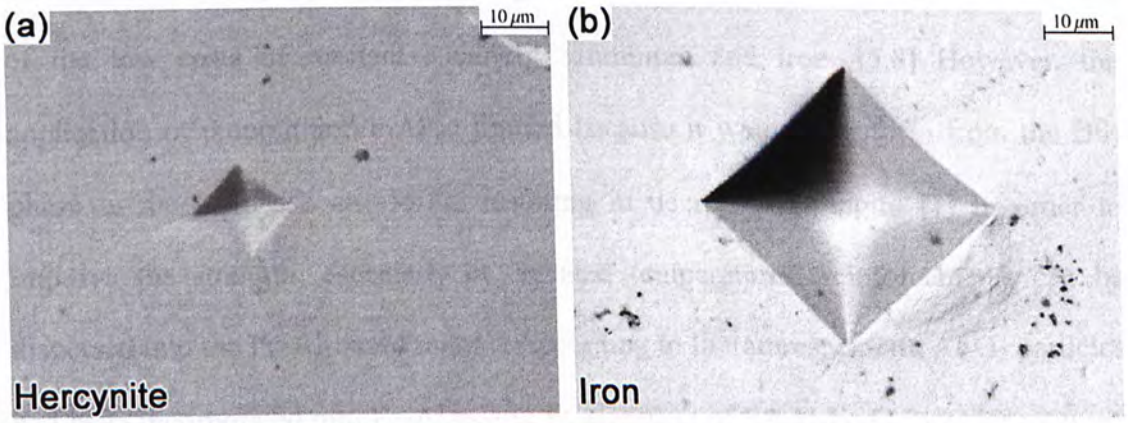

Fig. 3.10. Optical micrographs show the indents in the arc-melted sample after the Vickers hardness measurements using a 100 gf load indenter. (a) Hercynite portion: Vickers hardness number is 1108. (b) Iron portion: Vickers hardness number is 114.

Chapter 4 Synthesis of reinforced Fe_3Al-based MMC

4.1. Introduction

Intermetallic compounds are of great interest in high-temperature structural applications due to their excellent strengths at elevated temperatures and superior ductilities compared to ceramics. [1-4] In recent decades, there have been many studies on aluminides of nickel, titanium and iron due to their attractive attributes. They contain aluminum which is able to form protective Al_2O_3 film even at very low oxygen partial pressure. The Al_2O_3 film greatly enhances the corrosion resistance in oxidizing, sulfidizing and carbonizing atmospheres, which makes them suitable for applications such as components of coal gasification, gas turbine, heater and reactors. [5] They also have lower densities than most stainless steels, which is a critical advantage in the aerospace applications. [6-7]

Fe_3Al is one of the most intriguing aluminides in industrial perspective because of the low costs of reactants, namely, aluminum and iron. [5,8] However, the application of monolithic Fe_3Al is limited because it would transform from the $D0_3$ phase to the B_2 phase at ~550°C resulting in decreased strength. [1] In order to improve the strength, especially at elevated temperatures, reinforcements can be dispersed into the Fe_3Al-based matrix. According to literatures, ex-situ Al_2O_3 particles had been incorporated into Fe_3Al matrix by sintering of Fe-Al-Fe_2O_3 powder mixture, however, the wetting between the Fe_3Al/Al_2O_3 interfaces was poor. [8-10] Besides, the exothermic reaction between Fe and Al during sintering resulted in pores formation, which limited the relative density of the final product. [11] Fe_3Al-based MMC reinforced by in-situ Al_2O_3 particles had also been produced by sintering of iron aluminide and Fe_2O_3 powders. [6-7] However, the production cost was high due

to the higher cost of iron aluminide powder compared with Al and Fe powders. Also, there was no substantial improvement in wettability between Fe_3Al and Al_2O_3.

In this work, the Fe_3Al matrix was synthesized from elemental Fe and Al powders. Three kinds of in-situ oxides formed by the reaction sintering were used as reinforcements. Apart from Al_2O_3, MgO was used to evaluate whether the wettability between the matrix and the reinforcement could be improved. To further improve the mechanical properties of the MMC products, $MgAl_2O_4$ having larger hardness value than MgO was also studied. This chapter reports the fabrication and characterization of these MMCs. Models are proposed to explain the formations of oxides and Fe_3Al matrix during sintering. Comparison of microhardness and densities of MMCs with their pure Fe_3Al counterparts are also presented.

4.2. Experiments

Samples to be investigated in this work were prepared from commercial powders of iron (99.5% purity, <10μm, Alfa), aluminum (99.7% purity, <44 μm, Strem), magnesium (99% purity, <44 μm, Strem), iron(II,III) oxide (98% purity, <5 μm, Aldrich) and aluminum oxide (99+% purity, calcined, 1-2 μm, IL). Details of sample preparation are described as follows:

1. For the Al_2O_3-reinforced sample, Fe-Al-Fe_3O_4 mixture with a molar ratio of 25:23:4 was cold-pressed into 3-mm-thick pellets with a diameter of 10 mm. DTA was conducted on a small piece of cut sample to determine the temperatures at which the displacement reactions between Al and Fe_3O_4, and the chemical reaction between Al and Fe took place. After DTA, the green samples were being sintered separately in a tube furnace for 3 h in argon atmosphere with temperatures slightly above the DTA troughs/peaks appeared.

2. For the MgO-reinforced sample, Fe-Al-Mg-Al_2O_3 mixture with a molar ratio of 27:5:6:2 was used instead. Al_2O_3 and Mg powders were mixed and ground with a mortar for ~10 min before adding Fe and Al powders. As Mg is soft and ductile, it coated the Al_2O_3 powder after this process, therefore, the displacement reaction between Mg and Al_2O_3 was facilitated. A small piece of powder compact was analyzed by the DSC to determine the temperatures at which the displacement reactions between Mg and Al_2O_3, and the chemical reaction between Al and Fe took place. The green samples were then treated with two-step sintering. In the step-one sintering, disintegrated samples containing MgO particles were obtained after heat treatment for 1 h at temperature slightly above the DSC peak appeared. After that, the samples were grinded and re-pressed into pellets. The Fe_3Al matrix was then formed after the step-two sintering.
3. The preparation of the $MgAl_2O_4$-reinforced sample was similar to that of the MgO-reinforced sample, the relative amount of Mg in the Fe-Al-Mg-Al_2O_3 mixture was reduced and the molar ratio was 45:13:3:4. After the step-one sintering, some Al_2O_3 remained as the amount of Mg was insufficient to reduce all Al_2O_3 to MgO. The remaining Al_2O_3 then further reacted with MgO and formed $MgAl_2O_4$ during the step-two sintering.

The sintered samples were grinded into powders for XRD analyses to determine the phases presented. The 2θ angles and intensities of the obtained diffraction patterns were matched with the standard patterns from JCPDS - International Centre for Diffraction Data for phase identifications. In general, fluorescence occurs when iron-containing phases are being illuminated by X-ray and the signals of some other phases could be over-shadowed. In order to avoid this problem, the sample powders were treated with a magnet to separate iron-rich portion (Fig. 4.1), or in another

alternative, samples were leached with 2M $FeCl_3$ ethanol-based solution to extract reinforcements from the iron-rich Fe_3Al matrix (Fig. 4.2). Microstructural and elemental analyses were conducted by SEM and EDS. The Vickers hardness and the densities of the sintered samples were measured by microhardness tester and Archimedes's method, respectively, and the results were compared with those of their pure Fe_3Al counterparts.

4.3. Results and discussion

4.3.1. Al_2O_3-reinforced samples

4.3.1.1. DTA and XRD results

The DTA curve of the Fe-Al-Fe_3O_4 sample is shown in Fig. 4.3. Three exothermic peaks were found: a sharp peak at 654°C, and two board peaks at 1045 and 1343°C. Based on these results, the samples were being sintered separately for 3 h at 660, 900, 1030 and 1400°C before they were furnace-cooled to room temperature.

The XRD patterns of the green sample and the sintered samples are shown in Fig. 4.4. Peaks in the pattern of the green sample corresponded to those of Fe, Al and Fe_3O_4. The absence of Al peak and the appearance of Fe_2Al_5 peaks in the XRD pattern of the sample sintered at 660°C implied that molten Al had reacted with Fe at that temperature to form Fe_2Al_5. In the pattern of the sample sintered at 900°C, peaks corresponded to Fe_3O_4 disappeared. A reasonable explanation was that Fe_3O_4 had been reduced by Fe_2Al_5 to form FeO and Al_2O_3. The absence of FeO and Al_2O_3 peaks might be attributed to their amorphous status or the strong background caused by fluorescence. To verify this deduction, the sample powder was leached with $FeCl_3$ solution to remove Fe and Fe_2Al_5, and no peak was found in the pattern of the extract (Fig. 4.5). Furthermore, the EDS results indicated that it contained Fe, Al and O (Fig. 4.6). When the extract was heated at 1400°C for 1 h, Al_2O_3 and FeO peaks were

detected by XRD. Therefore, the sample sintered at 900°C was confirmed to have amorphous FeO and Al_2O_3. In the pattern of the 1100°C sintered sample, Fe_3Al peaks were found, which indicates that Al in the Fe_2Al_5 had diffused to Fe to form Fe_3Al. Peaks corresponded to Al_2O_3 and Fe_3Al were identified for the sample sintered at 1400°C. The result was further confirmed by the pattern of the powder extracted by $FeCl_3$ solution in which Al_2O_3 peaks were found (Fig. 4.5). These results indicated that the displacement reactions have completed after sintering at 1400°C.

4.3.1.2. SEM and EDS results

4.3.1.2.1. Green sample

The SEM micrographs of the green Fe-Al-Fe_3O_4 compact are shown in Fig. 4.7. The dark grains were Al, having a size distribution from a few to tens of microns. The Fe grains appeared bright and were smaller than 10μm. The particles with size smaller than 1 μm were Fe_3O_4.

4.3.1.2.2. Sample sintered at 660°C

Fig. 4.8. contains two SEM micrographs with different scales that show the microstructure of the sample sintered at 660°C. The EDS analyses showed that the grains appeared dark consisted of ~14 at% Fe and ~86 at% Al, the light grains were mainly composed of Fe while the particles between the grains contained ~43 at% Fe and ~57 at% O. With reference to the XRD results, it was apparent that the dark grains, light grains and particles were Fe_2Al_5, Fe and Fe_3O_4 respectively. Therefore, it was evident that Al reacted with Fe to form Fe_2Al_5 at ~660°C.

4.3.1.2.3. Sample sintered at 900°C

Fig. 4.9. shows the SEM micrographs of the sample sintered at 900°C. The coalescence of Fe_2Al_5 (dark) and Fe (bright) grains was observed as their boundaries became blurred. There were some white and black particles with sub-micron size located between the grains. According to the EDS analyses, the white particles mainly

contained Al and O while the black particles consisted of Fe and O. The $FeCl_3$ solution was used to remove the Fe_2Al_5 and Fe and the SEM micrograph of the extract was shown in Fig 4.12a. With reference to the XRD and EDS results, the black and white particles were identified to be amorphous FeO and Al_2O_3, respectively, where were the products of the reaction between Fe_3O_4 and Fe_2Al_5.

4.3.1.2.4. Sample sintered at 1100°C

The SEM micrographs of the sample sintered at 1100°C are shown in Fig. 4.10. It was noticeable that the Fe_2Al_5 and Fe grains welded together and formed the continuous matrix. There were some white particles and black particles embedded in the matrix, their amounts increased and decreased, respectively, compared with the sample sintered at 900°C (Fig. 4.9). According to the EDS results, the matrix consisted of ~75 at% Fe and ~25 at% Al, the white particles mainly contained Al and O while the black particles consisted of Fe and O. With reference to the XRD results, it was apparent that the matrix was Fe_3Al while the black and white particles were amorphous FeO and Al_2O_3, respectively. From these results, it can be confirmed that more FeO was reduced to form Fe and Al_2O_3, and Al had diffused from Fe_2Al_5 to Fe resulting in the formation of Fe_3Al matrix beyond ~1100°C.

4.3.1.2.5. Sample sintered at 1400°C

Fig. 4.11. is a set of SEM micrographs showing the microstructure of the sample sintered at 1400°C. Agglomerates of white particles with size smaller than a few microns were found in the Fe_3Al matrix. The $FeCl_3$ solution was used to remove the Fe_3Al and the SEM micrograph of the extract was shown in Fig 4.12b. Taking the XRD results into account, the white particles were determined to be crystalline α-Al_2O_3. Therefore, it was evident that FeO was further reduced by Fe_3Al to form Al_2O_3 at ~1400°C, and this reaction was followed by the crystallization of amorphous Al_2O_3. It was noticed that some voids were created by the detachment of Al_2O_3 from

the agglomerates during the polishing process and the number and size of these defects increased with increasing polishing time according to OM observations. This phenomenon was attributed to the poor wetting between Fe_3Al and Al_2O_3, this claim was further supported by the fact that Al_2O_3 formed agglomerates instead of distributed evenly in the Fe_3Al matrix.

4.3.1.3. Reaction mechanisms

The reactions that occurred at temperature where DTA peaks were located could be deduced based on the results of DTA, XRD and those from the microstructural and elemental analyses.

The green sample was composed of Fe, Al and Fe_3O_4 powder. When the sample was heated to the temperature where the first DTA peak was located (654°C), the highly exothermic reaction between Al and Fe was triggered forming Fe_2Al_5. The reaction could be represented by the following equation

$$2Fe_{(s)} + 5Al_{(s)} \rightarrow Fe_2Al_{5\,(s)} \ldots\ldots (4.1)$$

where the subscripts s refers to the solid form of the substance.

After sintering at ~900°C (near the beginning of the second exothermic peak), Fe_3O_4 reacted with Fe_2Al_5 to form amorphous FeO and Al_2O_3. As the temperature increased to ~1100°C (near the end of the second exothermic peak), more amorphous Al_2O_3 formed as FeO was further reduced by iron aluminides, at the same time, Fe_3Al matrix formed as Al had diffused from Fe_2Al_5 to Fe. When the sample was sintered at the temperature where the third DTA peak was found (1343°C), the displacement reactions completed and were followed by the crystallization of Al_2O_3. These two reactions were exothermic and contributed to the second and third DTA peaks. In fact, the displacement reaction was a two-step process, the Fe_3O_4 transformed into FeO before it was totally reduced to Fe and can be described by the following equations

$$2Al_{(\text{in } Fe_2Al_5)} + 3Fe_3O_{4\,(s)} \rightarrow 9FeO_{(s,\ amporhous)} + Al_2O_{3\,(s,\ amorphous)} \ldots\ldots (4.2)$$

$$2Al_{(\text{in } Fe_3Al)} + 3FeO_{(s,\ amporhous)} \rightarrow 3Fe_{(s)} + Al_2O_{3\,(s,\ amorphous)} \ldots\ldots (4.3)$$

According to the Fe-Al binary phase diagram (Fig. 1.5), Fe_3Al is a nonstoichiometric intermetallic (contains 24 to 33 at% Al at 400°C). Therefore, even though its Al content decreased after reacting with FeO, its crystal structure remained unchanged.

4.3.2. MgO-reinforced samples

4.3.2.1. DSC and XRD results

The DSC curve of the Fe-Al-Mg-Al_2O_3 sample is shown in Fig. 4.13. Two endothermic troughs and one exothermic peak were found at 437, 450 and 456°C, respectively. Based on these results, the samples were being sintered for 1 h at 480°C (step-one sintering) before they were furnace-cooled to room temperature.

The green sample disintegrated and became a fragile pellet after the step-one sintering (Fig. 4.14a). The diffraction patterns of the sample powder treated by a magnet are shown in Fig. 4.14b. As expected, peaks in the pattern of the iron-rich portion corresponded to those of Fe. On the contrary, Fe_2Al_5 and MgO peaks were found in the pattern of the iron-deficient portion. These results indicated that Al_2O_3 was reduced by Mg to form MgO, and Al reacted with Fe to form Fe_2Al_5 during the step-one sintering. After the step-two sintering at 1000°C for 3h, the reinforcements were extracted from the Fe_3Al matrix with $FeCl_3$ solution and they were identified to be MgO in the diffraction pattern (Fig. 4.15a). However, $MgAl_2O_4$ peaks instead of MgO peaks were found in the diffraction pattern of the extract using higher sintering temperatures, it implies that MgO is unstable in the Fe_3Al matrix above 1000°C.

4.3.2.2. SEM and EDS results

4.3.2.2.1. Green sample

The SEM micrographs of the green Fe-Al-Mg-Al_2O_3 compact are shown in Fig. 4.16. The grains appeared dark were Al, having a size distribution from a few to tens of microns. The Fe grains appeared bright and were smaller than 10μm. The particles with size ~tens microns were Al_2O_3. The Al_2O_3 particles were enclosed by a dark layer of substance with thickness of a few microns, which was identified to be Mg by EDS analyses.

4.3.2.2.2. Step-one sintered sample (after re-pressing)

After step-one sintering (480°C for 1h), the fragile sample was ground and re-pressed. Fig. 4.17. contains SEM micrographs that show the microstructure of the re-pressed sample. According to the EDS analyses, the black particles contained ~50 at% Mg and ~50 at% O, the bright grains were mainly composed of Fe while the grains appeared slightly darker consisted of ~14 at% Fe and 86 at% Fe. With reference to the XRD results, they should be MgO, Fe and Fe_2Al_5, respectively. Therefore, it is reasonable to deduce that Mg reacted with Al_2O_3 to form MgO and Al reacted with Fe to form Fe_2Al_5 during the step-one sintering.

4.3.2.2.3. Step-two sintered sample

Fig. 4.18. shows the SEM micrographs of the sample sintered at 1000°C. The Fe_2Al_5 and Fe grains fused together to form the matrix composed of bright grains. Some dark particles having sub-micron size were located at the grain boundaries and those having size of ~tens microns embedded in the matrix. According to the EDS analyses, the matrix consisted of ~75 at% Fe and ~25 at% Al. The matrix was removed by the $FeCl_3$ solution the SEM micrograph of the extract was shown in Fig 4.15b, the EDS results revealed that the extract contained ~50 at% Mg and ~50 at% O. It is apparent that the matrix and the dark particles are Fe_3Al and MgO, respectively, which were the tow phases identified in the XRD spectra (Fig. 4.15a).

4.3.2.3. Reaction mechanisms

The reactions that occurred during the two-step sintering could be deduced from the results of DSC, XRD and those from the microstructural and elemental analyses.

Firstly, two endothermic troughs were found in the DSC curve at 437 and 450°C, which match with the melting points of $Al_{12}Mg_{17}$ and Al_3Mg_2, respectively. As the green sample consisted of Fe, Al and Mg and Al_2O_3 powders, therefore, the two troughs can be attributed to the reactions between Al and Mg forming $Al_{12}Mg_{17}$ and Al_3Mg_2, which melted immediately and absorbed heat from the ambient. When the sample was heated to 456°C, the exothermic DSC peak was located. Due to the presence of MgO after sintering at 480°C, it is reasonable to deduce that displacement reaction between Mg (existed in molten Al_3Mg_2) and Al_2O_3 occurred at 456°C forming MgO. The Fe and Al were expected to react and form Fe_2Al_5 at ~654°C form the results of the Al_2O_3-reinforced system, however, Fe_2Al_5 was found after the step-one sintering. This discrepancy can be explained by two factors. First, heat released during the formation of MgO provided extra energy to trigger the reaction between Fe and Al. Second, the Al existed in molten Al_3Mg_2 instead of solid Al powder may increase its reactivity. The reactions occurred during the step-one sintering are represented by the following equations

$$3Mg_{(l,\,in\,Al_3Mg_2)} + Al_2O_{3\,(s)} \rightarrow 3MgO_{(s)} + 2Al_{(l)} \ldots\ldots (4.4)$$

$$2Fe_{(s)} + 5Al_{(l,\,in\,Al_3Mg_2)} \rightarrow Fe_2Al_{5\,(s)} \ldots\ldots (4.5)$$

where the subscripts s and l refer to the solid and liquid form of the substance, respectively. Since reactions 4.4 and 4.5 are exothermic and molten Al_3Mg_2 was present during the step-one sintering, such that some Mg in Al_3Mg_2 vaporized due to its low vapor pressure, the Mg vapor then caused the sample to disintegrate and become a fragile pellet after the process. The observation of a Mg layer on the alumina boat holding the sample supports this claim.

The subsequent step-two sintering at 1000°C after the re-pressing caused the diffusion of Al from Fe_2Al_5 to Fe forming the Fe_3Al matrix. Furthermore, as the temperature was further increased, MgO reacted with Al in Fe_3Al to form $MgAl_2O_4$ by the following reactions

$$2Al_{(\text{in } Fe_3Al)} + 3MgO_{(s)} \rightarrow Al_2O_{3\,(s)} + 2Mg_{(g)} \ldots\ldots (4.6)$$

$$MgO_{(s)} + Al_2O_{3\,(s)} \rightarrow MgAl_2O_{4\,(s)} \ldots\ldots (4.7)$$

where the subscript g refer to the gaseous form of the substance. Mg vapor was produced via reaction 4.6. Continuous conversion of MgO to Al_2O_3 would occur provided that the Fe_3Al/MgO interface was exposed to flowing gas environment, where Mg vapor would be continuously swept away by the flowing gas. [3] However, since the MgO was embedded in the Fe_3Al matrix in our case, such that the reaction stopped when the interface had saturated with Mg vapor. Hence, some MgO was unreacted and reaction 4.7 was possible.

P. Shem et al. [3] found experimentally that that molten Al reacted with MgO to form Al_2O_3 starting at ~800°C, while Misra et al. [13] calculated that the reaction between FeAl and MgO was thermodynamically infeasible unless the temperature had exceeded 1000°C. In our work, as Al existed in Fe_3Al, its reactivity should lie between those of pure Al and FeAl. Therefore, it is reasonable that reaction 4.6 occurred at temperatures beyond 1000°C in our system.

4.3.3. $MgAl_2O_4$-reinforced samples

4.3.3.1. DSC and XRD results

In case of the $MgAl_2O_4$-reinforced system, the DSC curve of the green sample was the same with that of the MgO-reinforced system except that the area of the troughs/peak areas decreased as the amount of Mg had decreased. The diffraction

patterns of the step-one sintered samples of the two systems are also similar, the only difference is that the intensities of MgO peaks decreased. Unexpectedly, no Al_2O_3 peak was detected. Three different temperatures (900, 1200 and 1400°C) were used for the step-two sintering to study the formation of $MgAl_2O_4$ and the XRD patterns of the sample extracts were shown in Fig 4.20a. For the extract of the sample sintered at 900°C, small $MgAl_2O_4$ peaks were found in the diffraction pattern. The $MgAl_2O_4$ signal intensities increased substantially for those sintered at 1200 and 1400°C. These results imply that the formation of $MgAl_2O_4$ started at 900°C, and this process proceeded and the crystallinity of $MgAl_2O_4$ increased at higher temperatures.

4.3.3.2. SEM and EDS results

4.3.3.2.1. Green sample and step-two sintered sample (after re-pressing)

The microstructure of the green compact is the same with that of the MgO-reinforced system except that the Mg coating enclosing the Al_2O_3 particles was thinner.

Fig. 4.21. shows the SEM micrographs of the re-pressed sample after the step-one sintering. Similar to those of the MgO-reinforced system (Fig 4.17), Fe (bright) and Fe_2Al_5 (dark) grains were observed. According to the EDS analyses, the white particles contained ~40 at% Al and 60 at% of O while the black layer at their peripheries was consisted of ~50 at% Mg and ~50 at% O. It is evident that the particles are Al_2O_3 enclosed by a MgO layer. The thickness of the MgO layer was estimated to be ~1 μm, which could significantly shield Al_2O_3 from X-ray illumination, such that no Al_2O_3 peak was found in the diffraction pattern.

4.3.3.2.2. Step-two sintered samples

Fig. 4.22. contains two SEM micrographs at different scales that show the microstructure of the sample sintered at 900°C. White particles having size of ~tens of microns were found in the matrix composed of Fe_3Al grains. The EDS analyses

revealed that the center of the white particles contained ~40 at% Al and ~60 at% O, the signal intensities of Al decreased while that of Mg increased when probing towards the periphery, where consisted of ~50 at% Mg and ~50 at% O. These results imply that MgO started to react with Al_2O_3 and form $MgAl_2O_4$ at their interface. As the newly-formed $MgAl_2O_4$ was possibly poorly-crystalline, and it was covered by the MgO layer, so that its corresponding peaks were weak in the diffraction pattern (Fig. 4.20a).

The SEM micrographs of the sample sintered at 1200°C are shown in Fig. 4.23. The coalescence of Fe_3Al grains was observed and the white grains (Al_2O_3 enclosed by $MgAl_2O_4$ and MgO) appeared in the 900°C-sintered sample turned into grey grains with size up to ~30 μm. The EDS analyses showed that the grey grains contained ~14 at% Mg, ~30 at% Al and ~56 at% O. With reference to the XRD results of the extracted grains, they were identified to be $MgAl_2O_4$. It is noted that the peak intensities were stronger than those of the 900°C-sintered sample, which can be attributed to the higher yield and better crystallinity of $MgAl_2O_4$.

Fig. 4.24. are SEM micrographs of the sample sintered at 1400°C showing that the reinforcements distributed more uniformly in the Fe_3Al matrix compared with the 1200°C-sintered sample. Furthermore, the reinforcements extracted by $FeCl_3$ solution were found to be consisted of grey particles with size smaller than ~2 μm (Fig. 4.20b). The XRD results showed that the reinforcements were $MgAl_2O_4$ and the crystallinity of $MgAl_2O_4$ was further improved (Fig. 4.20a).

4.3.3.3. Reaction mechanisms

The reactions occurred during the step-one sintering are similar to that of the MgO-reinforced system. $Al_{12}Mg_{17}$ and Al_3Mg_2 formed as the temperature reached 437 and 450°C, respectively. When the sample was heated to 456°C, displacement reaction between Mg (existed in molten Al_3Mg_2) and Al_2O_3 occurred and formed MgO

(Reaction 4.4). Since the relative amount of Mg was less compared with the MgO-reinforced system, only the surface of Al_2O_3 grains was reduced by Mg and the center was unreacted, resulting in Al_2O_3 grains enclosed by a MgO layer. The Fe and Al reacted and formed Fe_2Al_5 at the same time (Reaction 4.5).

The reaction between MgO and Al_2O_3 started to take place and form poorly-crystalline $MgAl_2O_4$ during the step-two sintering at 900°C, and Fe_3Al grains were formed as Al had diffused from Fe_2Al_5 to Fe. When temperature increased to 1200°C, the coalescence of Fe_3Al grains occurred, and the reaction between MgO and Al_2O_3 completed and the resulting $MgAl_2O_4$ started to crystallize. The crystallization of $MgAl_2O_4$ continued as temperature rose to 1400°C, this process caused the $MgAl_2O_4$ to break down into small crystallites which distributed more uniformly in the Fe_3Al matrix compared with the poorly-crystalline form. Other than $MgAl_2O_4$ crystallization, no other reaction was observed, such that $MgAl_2O_4$ was determined to be chemically stable in Fe_3Al matrix up to 1400°C.

4.3.4. Microhardness and densities

Hardness and density measurements were performed on the MgO-reinforced and $MgAl_2O_4$-reinfoced samples, which were sintered at 1000 and 1400°C, respectively. For sake of comparison, the values were also obtained from their pure Fe_3Al counterparts sintered at the same temperature. No data is available for the Al_2O_3-reinforced sample due to the voids resulted from the detachment of reinforcement during polishing, which hindered indent measurement and increased the porosity.

The Vickers hardness numbers (VHNs) were obtained by a microhardness tester with 500gf load indenter at room temperature. Each value reported was an average of 10 points selected randomly from different positions of the sample. The results were

presented in Table 4.1 and the optical micrographs of the indents are shown in Figs. 25-26. It is found that the hardness of the MgO-reinforced and $MgAl_2O_4$-reinfoced samples improved by 22% and 20% compared with their Fe_3Al counterparts. Due to the decomposition of MgO beyond 1000°C, no comparison could be made for the MgO-reinforced and $MgAl_2O_4$-reinfoced samples sintered with the same temperature. Nevertheless, the VHN of the $MgAl_2O_4$-reinfoced sample (185±8) was significantly higher than that of the MgO-reinforced sample (143±5), it is reasonable due to the higher sintering temperature and hardness of reinforcements. The more uniform distribution of reinforcements in the $MgAl_2O_4$-reinfoced sample was not only shown in SEM and OM micrographs (Figs. 18,24,25-26), but was also reflected by the smaller standard deviation of the VHN.

The apparent density of the samples was measured by the Archimedes' method. According to the method, a body immersed in fluid experiences buoyancy equal to the weight of the fluid displaced. The apparent density is given by:

$$\rho = \frac{M_a}{M_a - M_f}\rho_f$$

where M_a and M_f are the weights of the sample in air and in fluid, respectively. ρ_f is the density of the fluid. In our work, the fluid used was water and the measurements were performed after the trapped air was released from the surface pores in a low-pressure desiccator for about 1 h. The results were averaged over 5 measurements and were summarized in Table 4.2.

The MgO-reinforced and $MgAl_2O_4$-reinforced samples were measured to be 95% and 98% of their theoretical densities (TD), which are significantly higher than their pure Fe_3Al counterparts. Moreover, due to the reduced porosity, the standard derivations of the VHNs of are also smaller. These results match with the OM micrographs shown in Figs. 4.25-26, where the pores could be clearly distinguished

from the reinforcements under the dark-field mode. According to the study of the sintering behavior of Fe and Al powders by Gedevanishvilli et al., it was very difficult to achieve densities in range 90-99% of TD by pressureless sintering due to the reaction between Fe and Al powders forming Fe_2Al_5. [11] First, the swelling of the sample occurred as the reaction was highly exothermic in nature, resulting in increased overall sample volume. Second, the composition of the sample changed from Fe-Al to Fe-Fe_2Al_5 which has higher density. As the overall sample volume and the compositional phase density increased simultaneously, therefore, a lot of pores were produced after the reaction. The size of the pores were too large to be eliminated in the subsequence sintering, that limited the densities if the final products.

In our works, the two-step sintering not only provided MgO or $MgAl_2O_4$ as reinforcements, it was also proven to be an effective approach to improve the sample density. After the abrupt formation of Mg vapor during the step-one sintering, the sample became a fragile pellet which could be grinded into powder and re-pressed easily. The pores formed during the Fe_2Al_5 formation were eliminated after the repressing. In contrast, the Fe and Fe_2Al_5 phases weld together after the reaction for pure Fe_3Al system, and further treatments would be difficult to conduct. The schematic diagrams comparing the conventional sintering and two-step sintering were shown in Fig. 4.27.

4.4. Conclusions

The Fe_3Al-based MMCs were reinforced by Al_2O_3, MgO or $MgAl_2O_4$. The Al_2O_3-reinforced MMC was synthesized by sintering of a Fe-Al-Fe_3O_4 mixture. At ~640°C, Al reacted with Fe to form Fe_2Al_5. The Fe_3O_4 was reduced by Fe_2Al_5 to amorphous FeO and Al_2O_3, and then to Fe and Al_2O_3 via a two-step displacement reactions occurred at temperatures beyond ~900°C. Meanwhile, diffusion of Al from

Fe_2Al_5 to Fe resulted in the formation of Fe_3Al matrix. At 1400°C, all the reactions completed and a Fe_3Al-Al_2O_3 MMC was obtained. The wetting between Fe_3Al matrix and Al_2O_3 particle was found to be poor.

In order to improve the mechanical properties of the MMC products, displacement reaction between Mg and Al_2O_3 was utilized to form MgO instead of Al_2O_3 in the Fe_3Al matrix. The second type, Fe_3Al-MgO MMC was produced by a two-step sintering of a Fe-Al-Mg-Al_2O_3 mixture. During the step-one sintering at 480°C, liquid Al_3Mg_2 formed and reacted with Al_2O_3 and Fe to form MgO and Fe_2Al_5. A fragile sample containing Fe, Fe_2Al_5 and MgO was obtained due to the abrupt formation of Mg vapor during the process. After re-pressing and the step-two sintering, Fe_3Al matrix was formed and the Fe_3Al-MgO MMC was produced. To avoid the decomposition of MgO in the Fe_3Al matrix, the sintering temperature was limited to 1000°C. Similarly, the third type, Fe_3Al-$MgAl_2O_4$ MMC was synthesized by decreasing the relative amount of Mg. Residual Al_2O_3 reacted with MgO to form $MgAl_2O_4$ during the step-two sintering at 1400°C. In accordance with the Vickers hardness and density measurements, the Fe_3Al-MgO and Fe_3Al-$MgAl_2O_4$ MMCs sintered at 1000 and 1400°C, respectively, were significantly harder and denser than their pure Fe_3Al counterparts, these improvements can be attributed to the presence of reinforcements and two-step sintering technique.

References

1. K. Suganuma, J. Alloys Compd., 197 (1993) p. 29-34
2. H. Gong, Y. Yin, X. Wang and Y.Liu, Mater. Res. Bull., 39 (2004) p. 513-521
3. A. K. Misra, Metall. Trans. A, 21A (1990) p. 441-446
4. J. Li, Y. Yin and H. Ma, Tribo. Inter., 38 (2005) p. 15-163
5. C. G McKamey, C. T. Liu, J. V. Cathcart, S. A. David and E. H. Lee, Evaluation of Mechanical and Metallurgical Properties of Fe3Al-Based Aluminides, ORNL/TM-10125, Oak Ridge National Laboratory, Oak Ridge, Tennessee, Martin Marietia Energy Systems, Inc., 1986, p. 1-29
6. R. Subramanian, C. G. McAkmey, J. H. Schneibel, L R. Buck and P. A. Menchhofer, Mater. Sci. Eng., A254 (1998) p. 119-128
7. R. Subramanian, C. G. McAkmey, L R. Buck, J. H. Schneibel, Mater. Sci. Eng., A239-240 (1997) p. 640-646
8. S. K. Mukherjee and S. Bandyopadhyay, Composites Part B, 28B (1997) p. 45-48
9. S. K. Mukherjee and S. Bandyopadhyay, Mater. Sci. Eng., A202 (1995) p. 123-127
10. J. H. Schneibel and S. C. Deevi, Mater. Sci. Eng., A364 (2004) p. 166-170
11. S. Gedevanishvili and S. C. Deevi, Mater. Sci. Eng., A325 (2002) p. 163-176
12. Binary alloy phase diagrams second edition plus updates on CD-ROM, ASM International, USA, 1996
13. P. Shen, H. Fujii, T. Matsumoto and K. Nogi, Acta. Mater., 52 (2004) p. 887-898
14. Binary alloy phase diagrams second edition plus updates on CD-ROM, ASM International, USA, 1996

Table 4.1. Vickers hardness numbers (VHNs) of the MgO-reinforced and $MgAl_2O_4$-reinfoced samples, which were sintered at 1000 and 1400°C, respectively. VHNs of pure Fe_3Al samples, prepared by similar heat treatment, are also shown for comparison.

Sample	Sintering temperature (°C)	VHN
Fe_3Al-based MMC reinforced by MgO	1000	143±8
Pure Fe_3Al	1000	117±14
Fe_3Al-based MMC reinforced by $MgAl_2O_4$	1400	185±5
Pure Fe_3Al	1400	154±13

Table 4.2. Apparent densities of the MgO-reinforced and $MgAl_2O_4$-reinfoced samples, which were sintered at 1000 and 1400°C, respectively. Values of pure Fe_3Al samples, prepared by similar heat treatment, are also shown for comparison.

Sample	Sintering temperature (°C)	Apparent density (g/cm^3)	Theoretical density (g/cm^3)	% of theoretical density
Fe_3Al-based MMC reinforced by MgO	1000	5.65	5.97	95%
Pure Fe_3Al	1000	5.72	6.57	87%
Fe_3Al-based MMC reinforced by $MgAl_2O_4$	1400	5.83	5.94	98%
Pure Fe_3Al	1400	5.94	6.57	90%

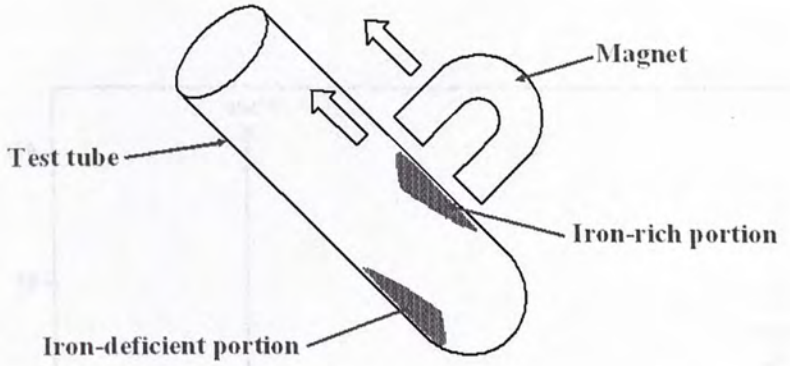

Fig. 4.1. Schematic diagram illustrates how the sample powders were treated with a magnet to separate iron-rich portions for XRD analyses.

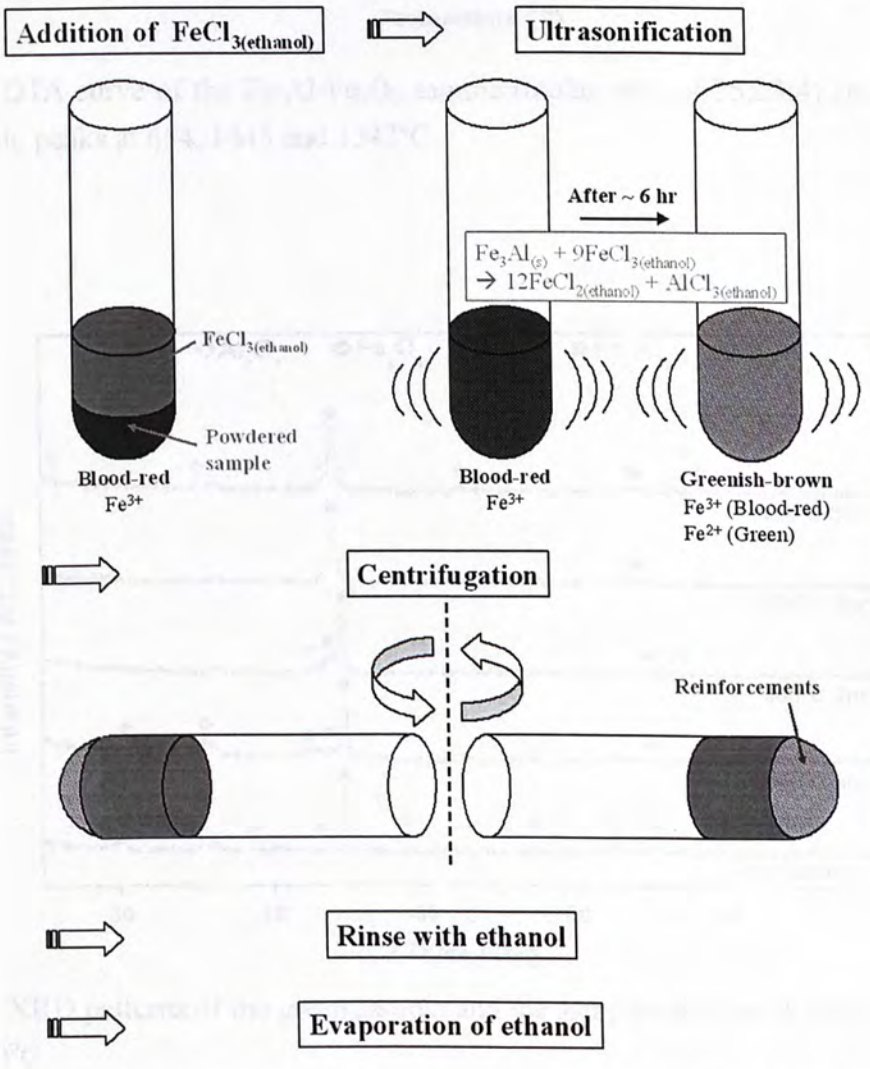

Fig. 4.2. Schematic diagrams illustrate how the sample powders were treated with $FeCl_3$ solution to extract reinforcements from Fe_3Al matrix for XRD analyses.

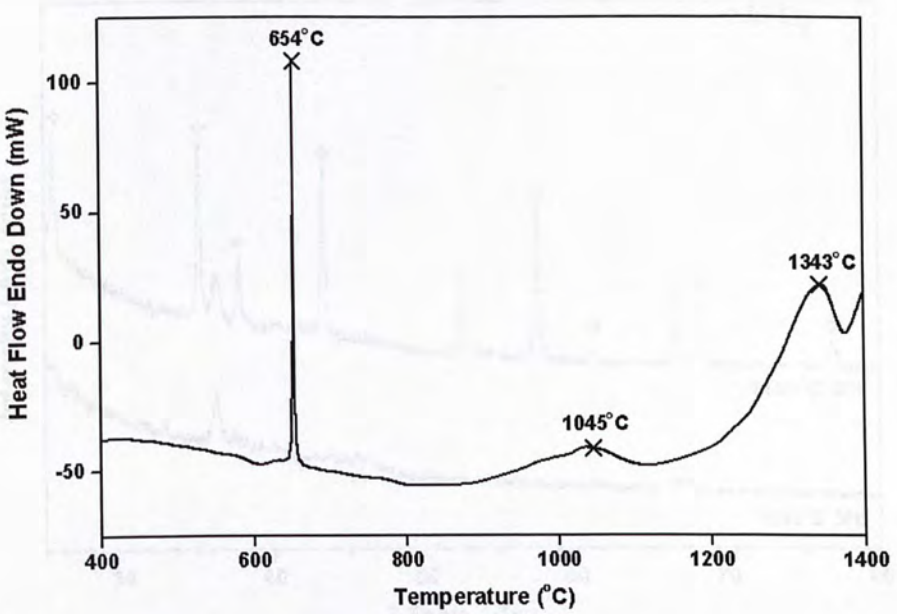

Fig. 4.3. DTA curve of the Fe-Al-Fe_3O_4 sample (molar ratio of 25:23:4) shows three exothermic peaks at 654, 1045 and 1343°C.

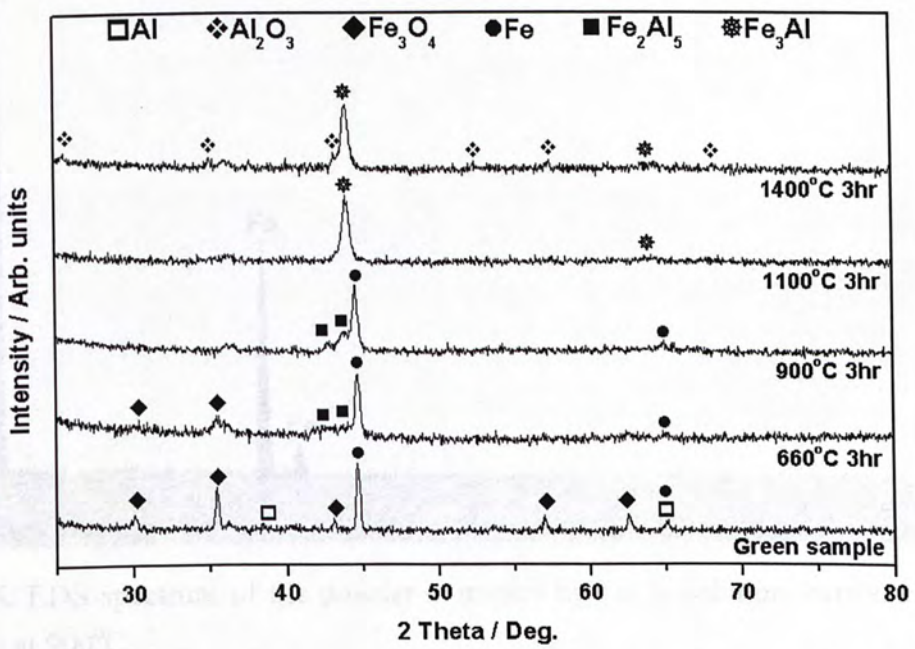

Fig. 4.4. XRD patterns of the green sample and the samples sintered at 660, 900, 1100 and 1400°C.

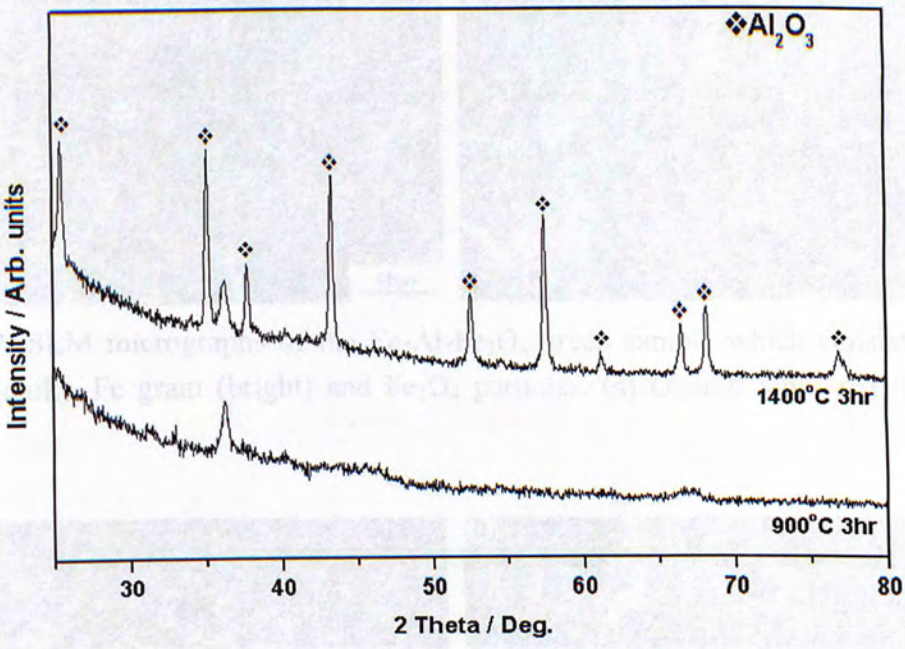

Fig. 4.5. XRD patterns of the powders extracted by $FeCl_3$ solution from the sample sintered at 900 and 1100°C (peaks at ~36° are background signals).

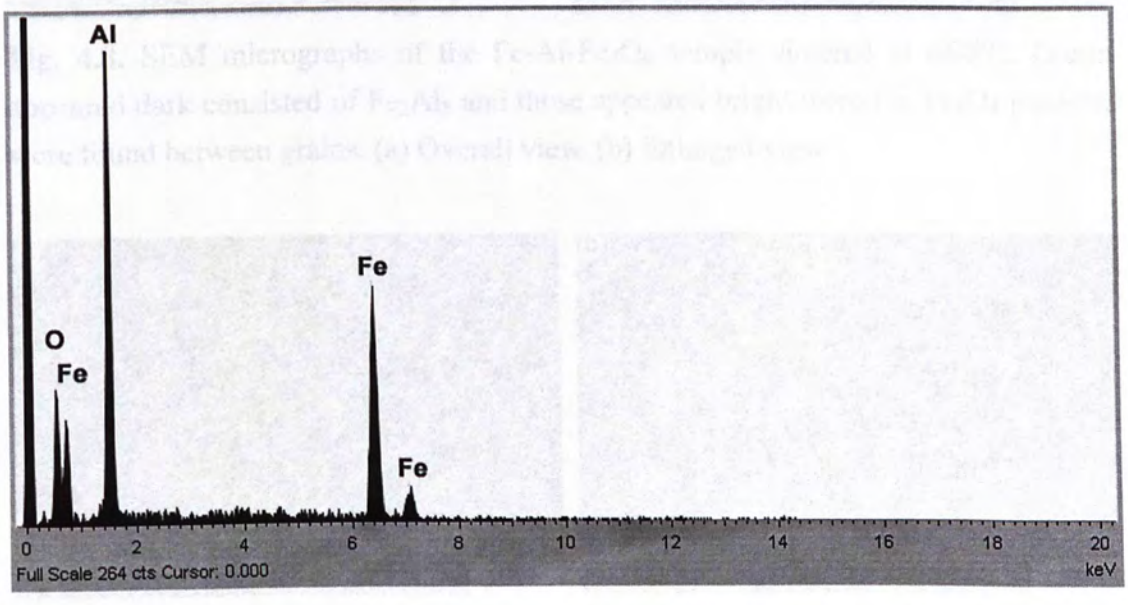

Fig. 4.6. EDS spectrum of the powder extracted by $FeCl_3$ solution form the sample sintered at 900°C.

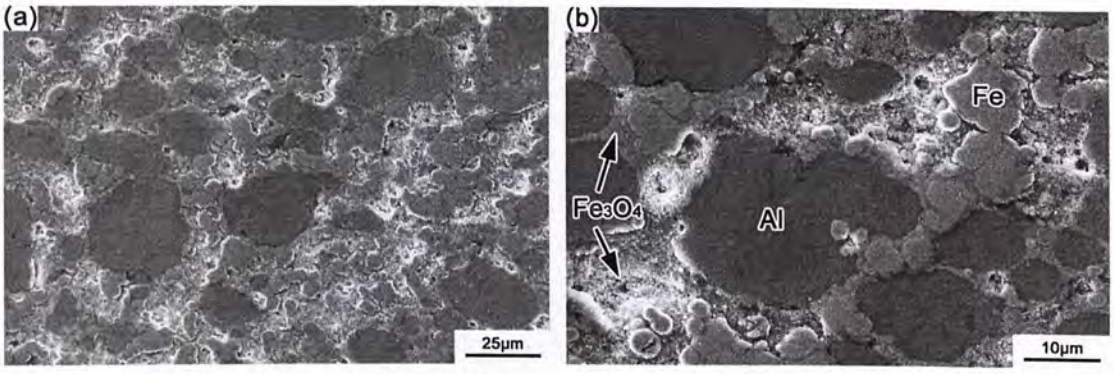

Fig. 4.7. SEM micrographs of the Fe-Al-Fe_3O_4 green sample which consists of Al grains (dark), Fe grain (bright) and Fe_3O_4 particles. (a) Overall view. (b) Enlarged view.

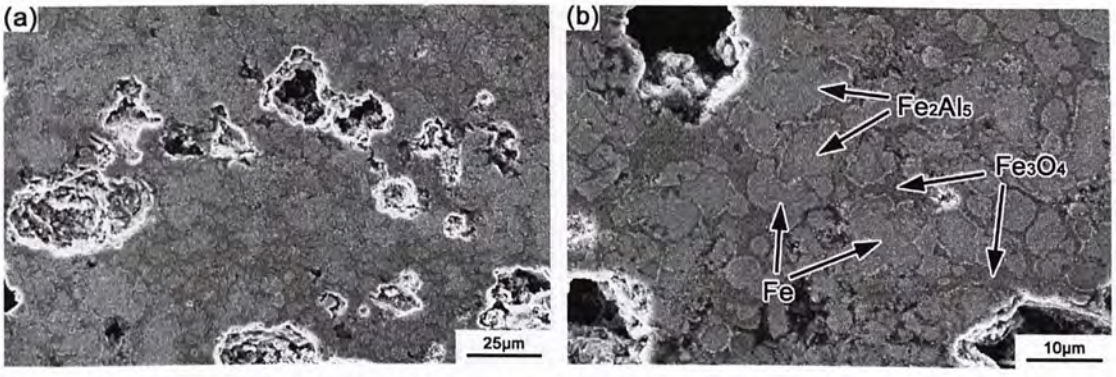

Fig. 4.8. SEM micrographs of the Fe-Al-Fe_3O_4 sample sintered at 660°C. Grains appeared dark consisted of Fe_2Al_5 and those appeared bright were Fe. Fe_3O_4 particles were found between grains. (a) Overall view. (b) Enlarged view.

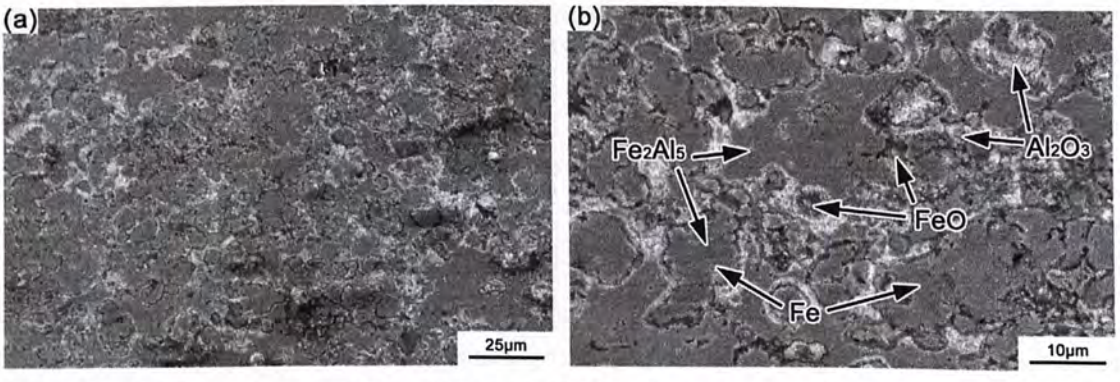

Fig. 4.9. SEM micrographs of the Fe-Al-Fe_3O_4 sample sintered at 900°C. The coalescence of Fe_2Al_5 (dark) and Fe (bright) grains was observed. The black and white particles in the matrix were amorphous FeO and Al_2O_3, respectively. (a) Overall view. (b) Enlarged view.

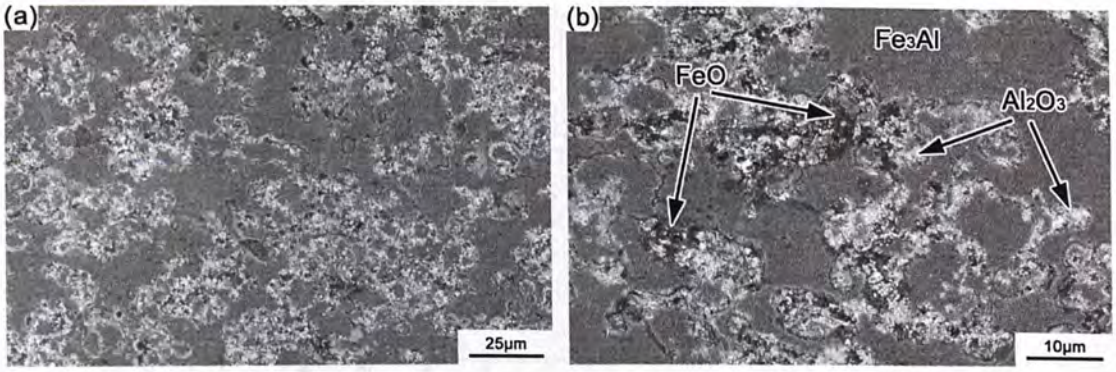

Fig. 4.10. SEM micrographs of the Fe-Al-Fe_3O_4 sample sintered at 1100°C. The matrix consisted of Fe_3Al. The black and white particles embedded in the matrix were amorphous FeO and Al_2O_3, respectively. (a) Overall view. (b) Enlarged view.

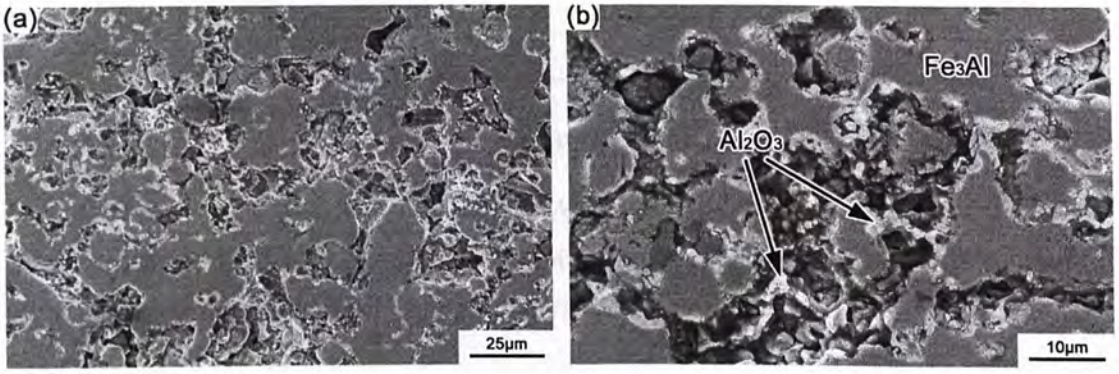

Fig. 4.11. SEM micrographs of the Fe-Al-Fe_3O_4 sample sintered at 1400°C. The matrix consisted of Fe_3Al. The white particles embedded in the matrix were crystalline Al_2O_3. (a) Overall view. (b) Enlarged view.

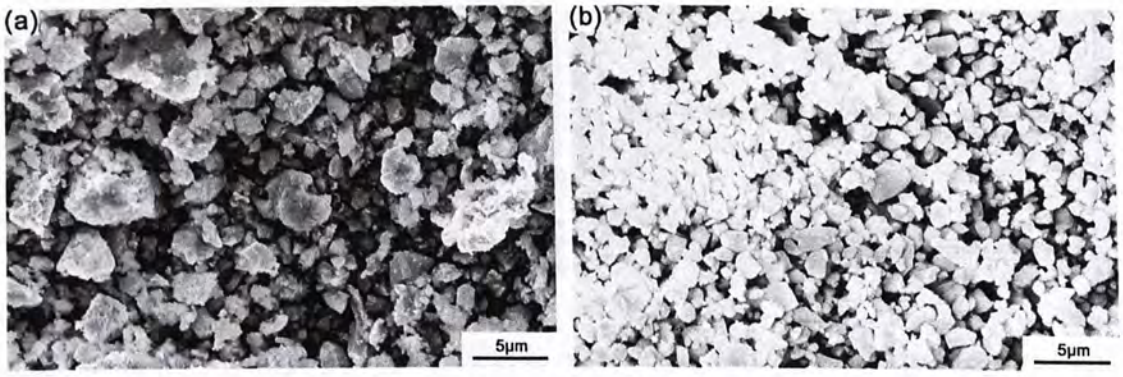

Fig. 4.12. SEM micrographs of the reinforcements extracted by $FeCl_3$ solution. (a) From the sample sintered at 900°C. (b) From the sample sintered at 1400°C.

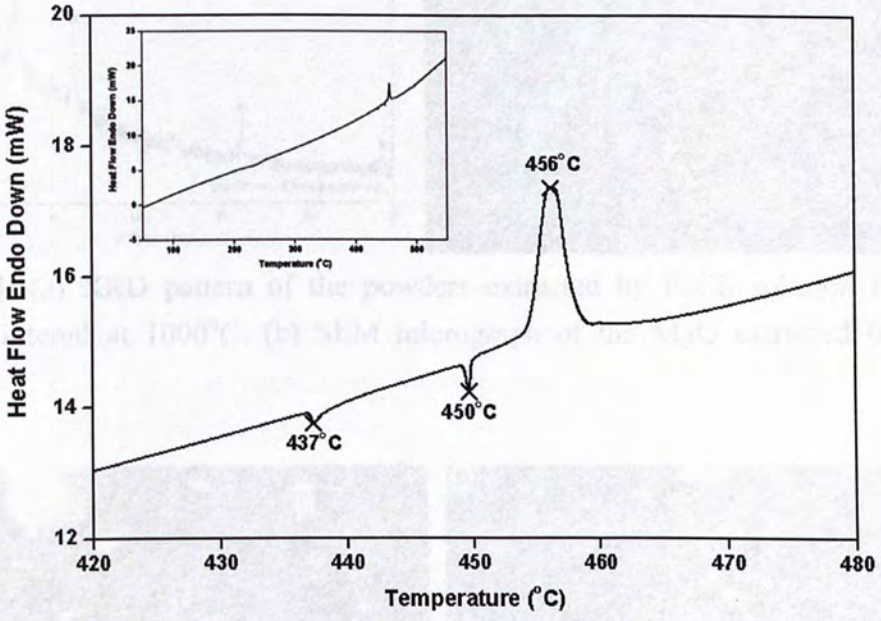

Fig. 4.13. DSC curve of the Fe-Al-Mg-Al_2O_3 sample ranging from 420 to 480°C (molar ratio of 27:5:6:2) shows two endothermic troughs at 437 and 450°C, and an exothermic peaks at 456°C. The inset shows the entire curve.

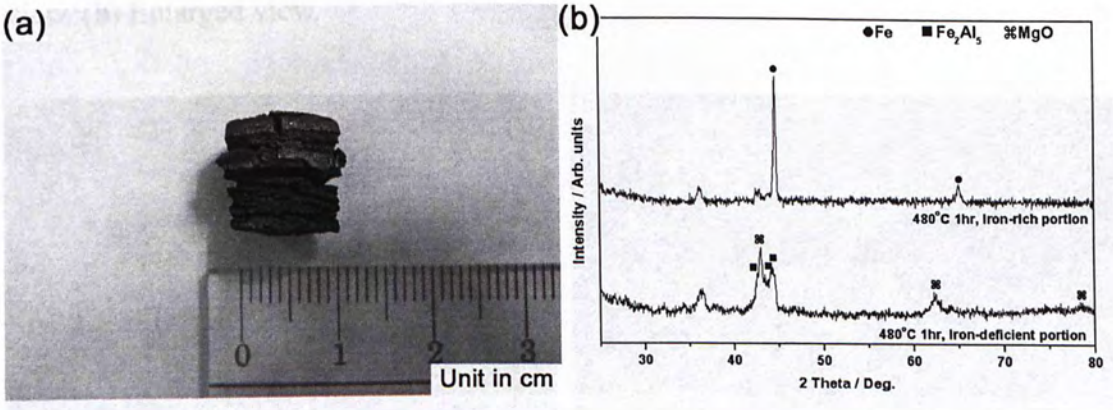

Fig. 4.14. (a) Photograph of the sample sintered at 480°C which disintegrated and became a fragile pellet. (b) XRD patterns of the sample powder treated with a magnet to separate iron-rich portion and iron deficient portion.

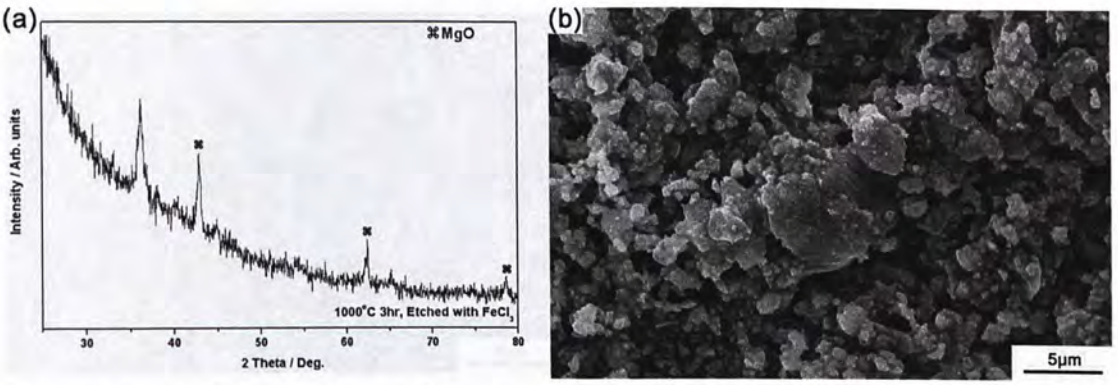

Fig. 4.15. (a) XRD pattern of the powders extracted by $FeCl_3$ solution from the sample sintered at 1000°C. (b) SEM micrograph of the MgO extracted by $FeCl_3$ solution.

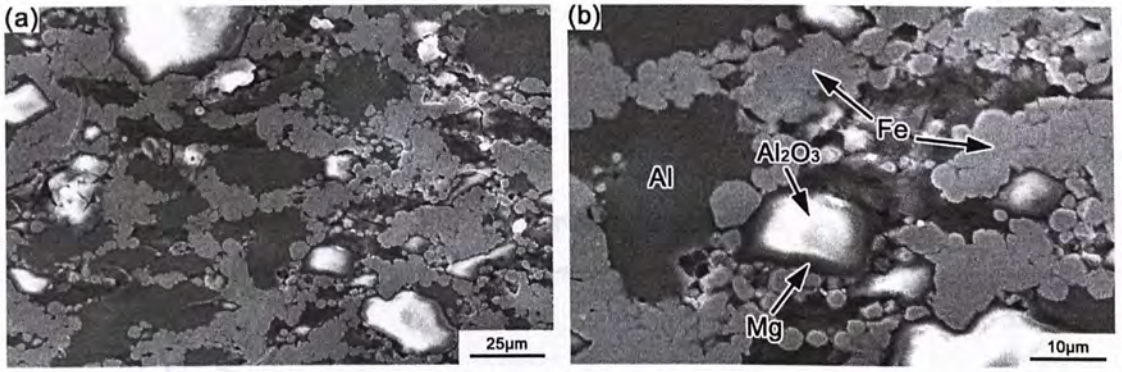

Fig. 4.16. SEM micrographs of the Fe-Al-Mg-Al_2O_3 green sample which consists of Al grains (dark), Fe grain (bright) and Al_2O_3 particles enclosed by Mg. (a) Overall view. (b) Enlarged view.

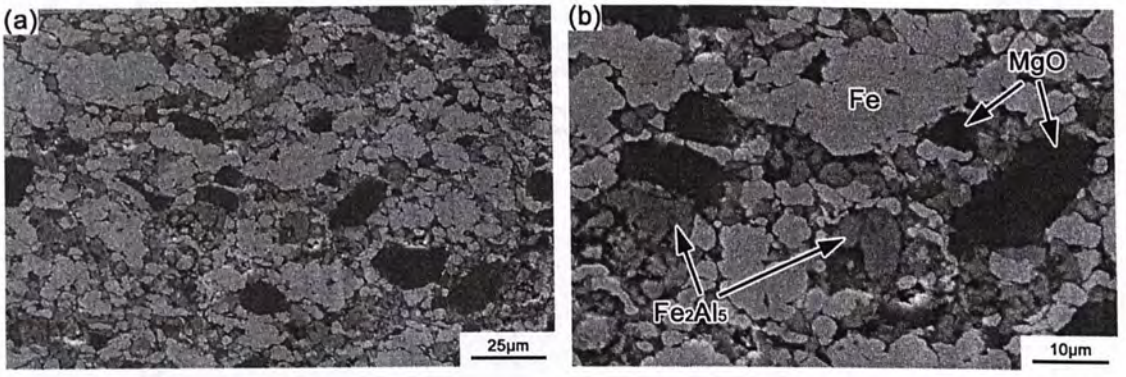

Fig. 4.17. SEM micrographs of the step-one sintered (480°C for 1h) sample after repressing. The black particles were MgO, the bright grains were Fe while the grains appeared slightly darker were Fe_2Al_5. (a) Overall view. (b) Enlarged view.

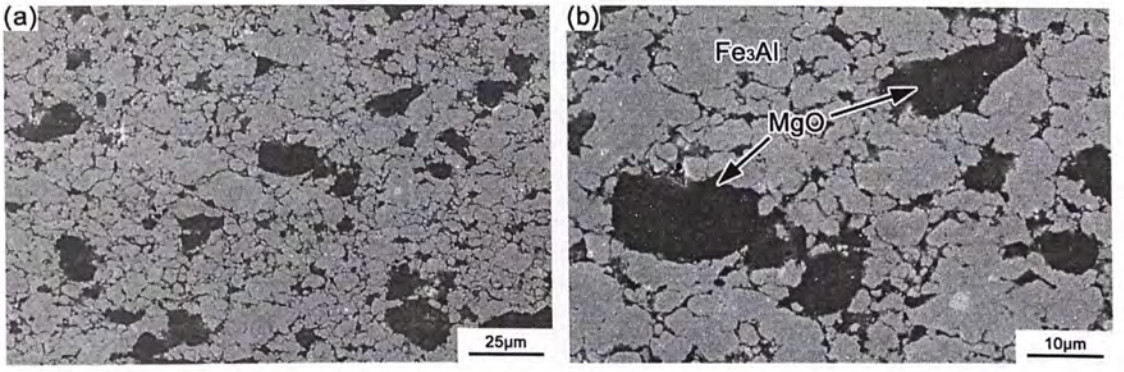

Fig. 4.18. SEM micrographs of the re-pressed sample sintered at 1000°C. The coalescence of Fe_2Al_5 (dark) and Fe (bright) grains was observed. The black and white particles between the grains were amorphous FeO and Al_2O_3, respectively. (a) Overall view. (b) Enlarged view.

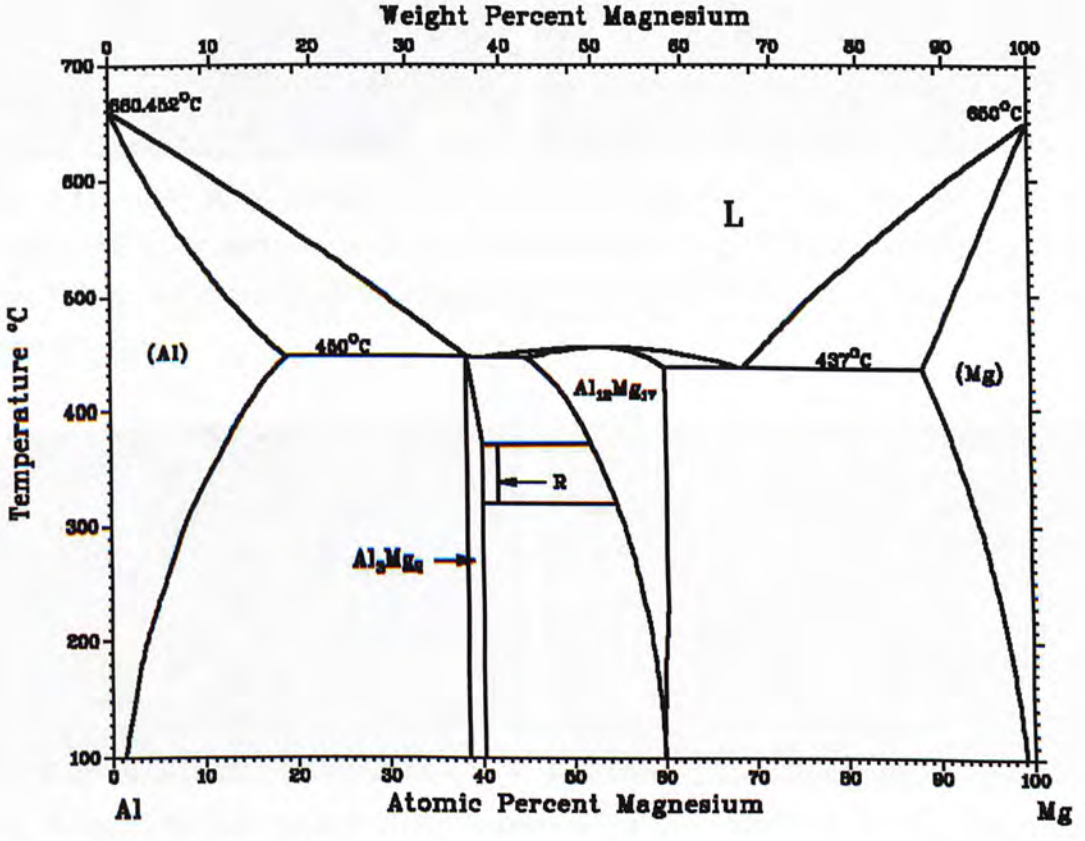

Fig. 4.19. Al-Mg phase diagram. [14]

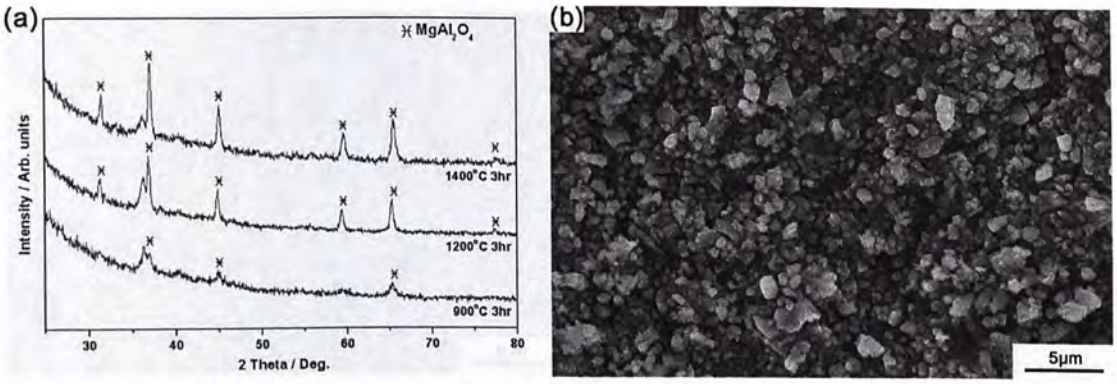

Fig. 4.20. (a) XRD patterns of the powders extracted by $FeCl_3$ solution from the sample sintered at 900, 1200 and 1400°C. (b) SEM micrograph of the $MgAl_2O_4$ extracted by $FeCl_3$ solution from the sample sintered at 1400°C.

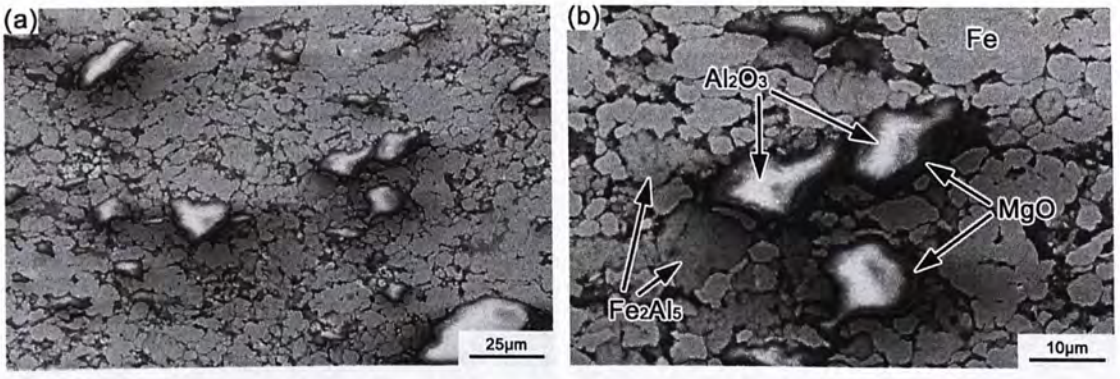

Fig. 4.21. SEM micrographs of the re-pressed sample after step-one sintering at 480°C. The white particles were Al_2O_3 coated by a layer of MgO, the bright grains were Fe while the grains appeared slightly darker were Fe_2Al_5. (a) Overall view. (b) Enlarged view.

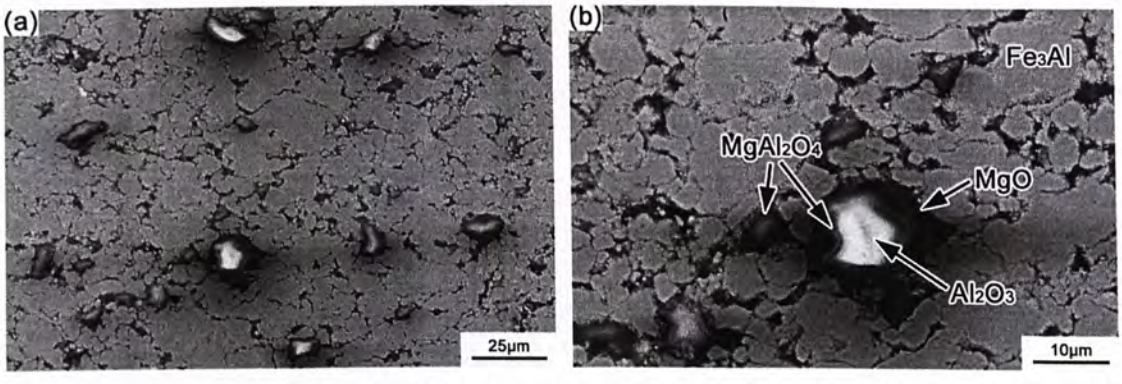

Fig. 4.22. SEM micrographs of the re-pressed sample sintered at 900°C. The Al_2O_3 particles (white) coated by MgO layer (black) were observed in the Fe_3Al matrix. Al_2O_3 and MgO started to react and form $MgAl_2O_4$ (grey). (a) Overall view. (b) Enlarged view.

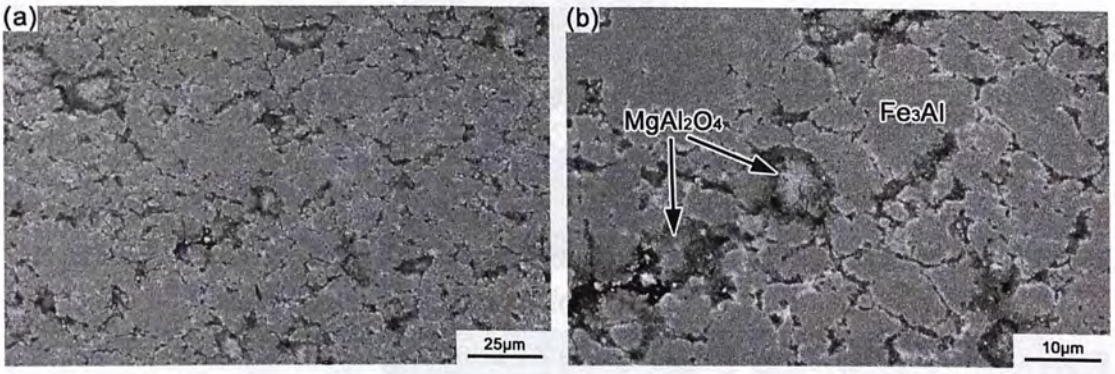

Fig. 4.23. SEM micrographs of the re-pressed sample sintered at 1200°C. The further coalescence of Fe_3Al grains was observed. All Al_2O_3 and MgO have reacted to form $MgAl_2O_4$, which started to crystallize at that temperature. (a) Overall view. (b) Enlarged view.

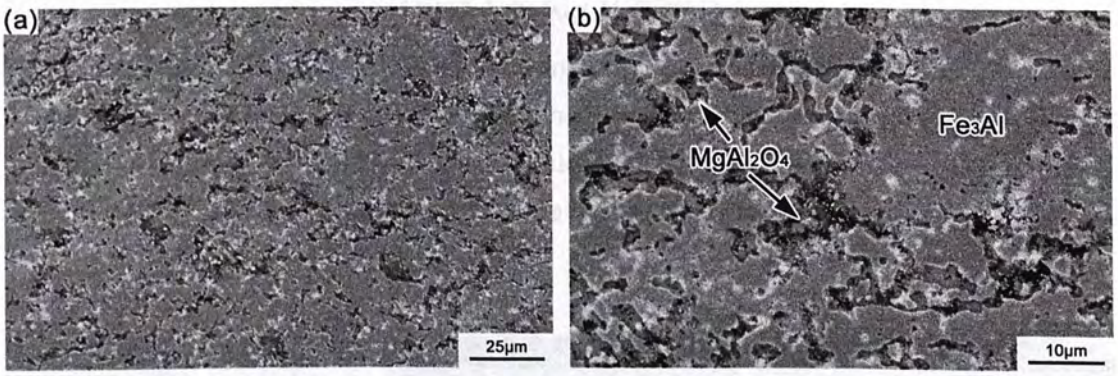

Fig. 4.24. SEM micrographs of the re-pressed sample sintered at 1400°C. The $MgAl_2O_4$ further crystallized and dispersed more uniformly in the Fe_3Al matrix. (a) Overall view. (b) Enlarged view.

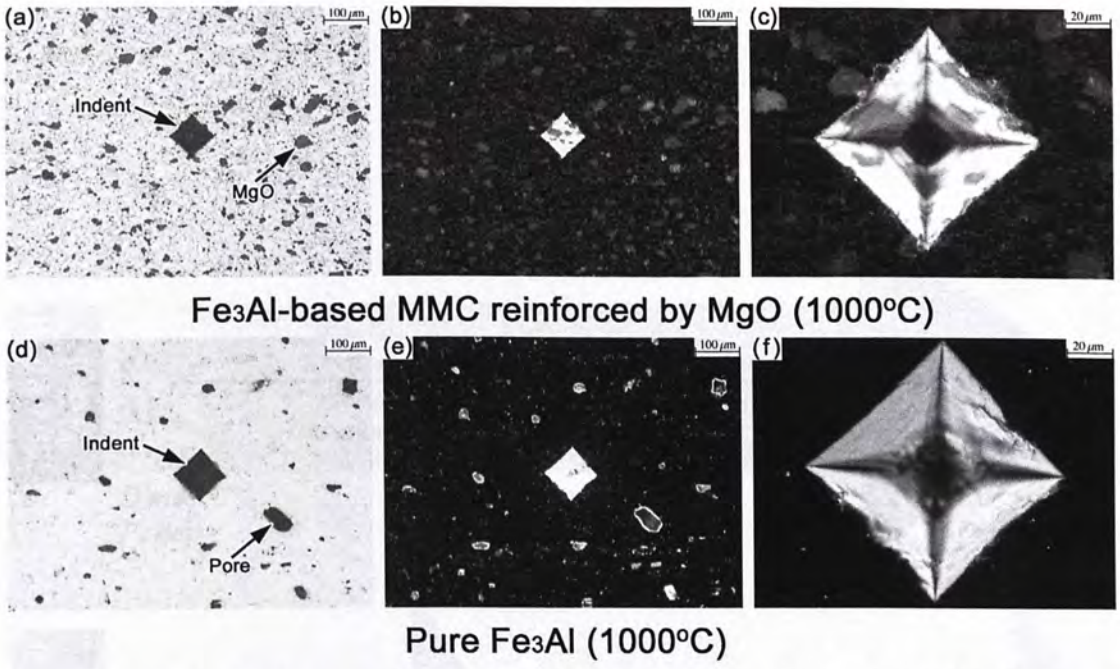

Fig. 4.25. Optical micrographs show the indents in the Fe_3Al-based MMC reinforced by MgO and pure Fe_3Al after the Vickers hardness measurements. (a and d) Overview, bright-field mode. (b and e) Overview, dark-field mode. Pores were distinguished from reinforcements. (c and f) Enlarged view, dark-field mode.

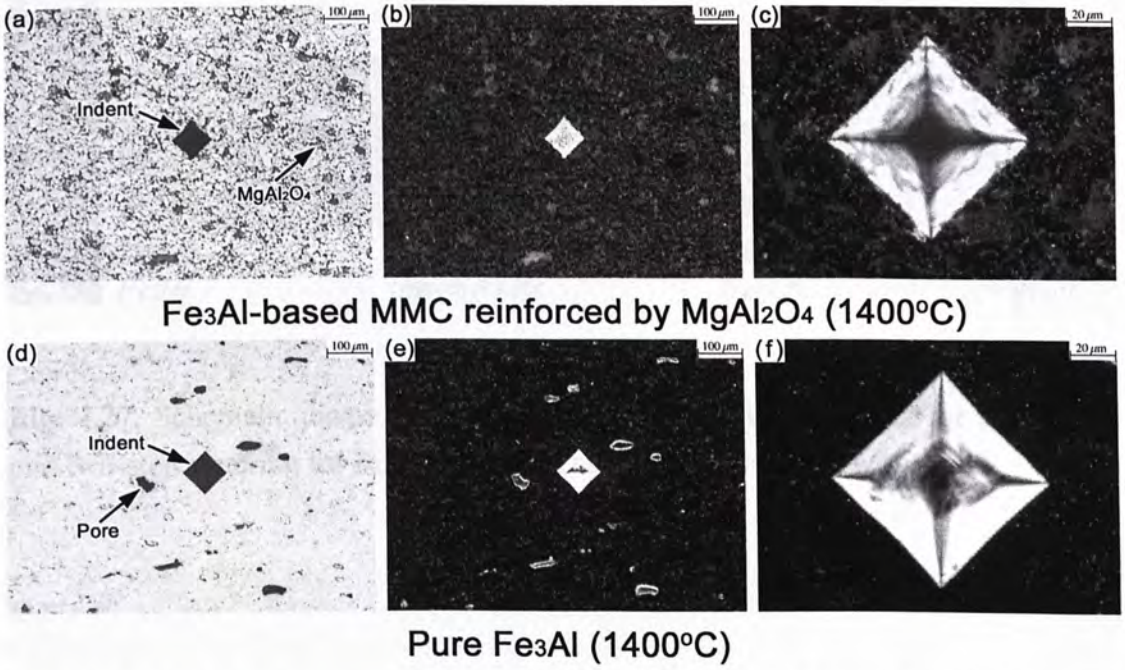

Fig. 4.26. Optical micrographs show the indents in the Fe_3Al-based MMC reinforced by $MgAl_2O_4$ and pure Fe_3Al after the Vickers hardness measurements. (a and d) Overview, bright-field mode. (b and e) Overview, dark-field mode. Pores were distinguished from reinforcements. (c and f) Enlarged view, dark-field mode.

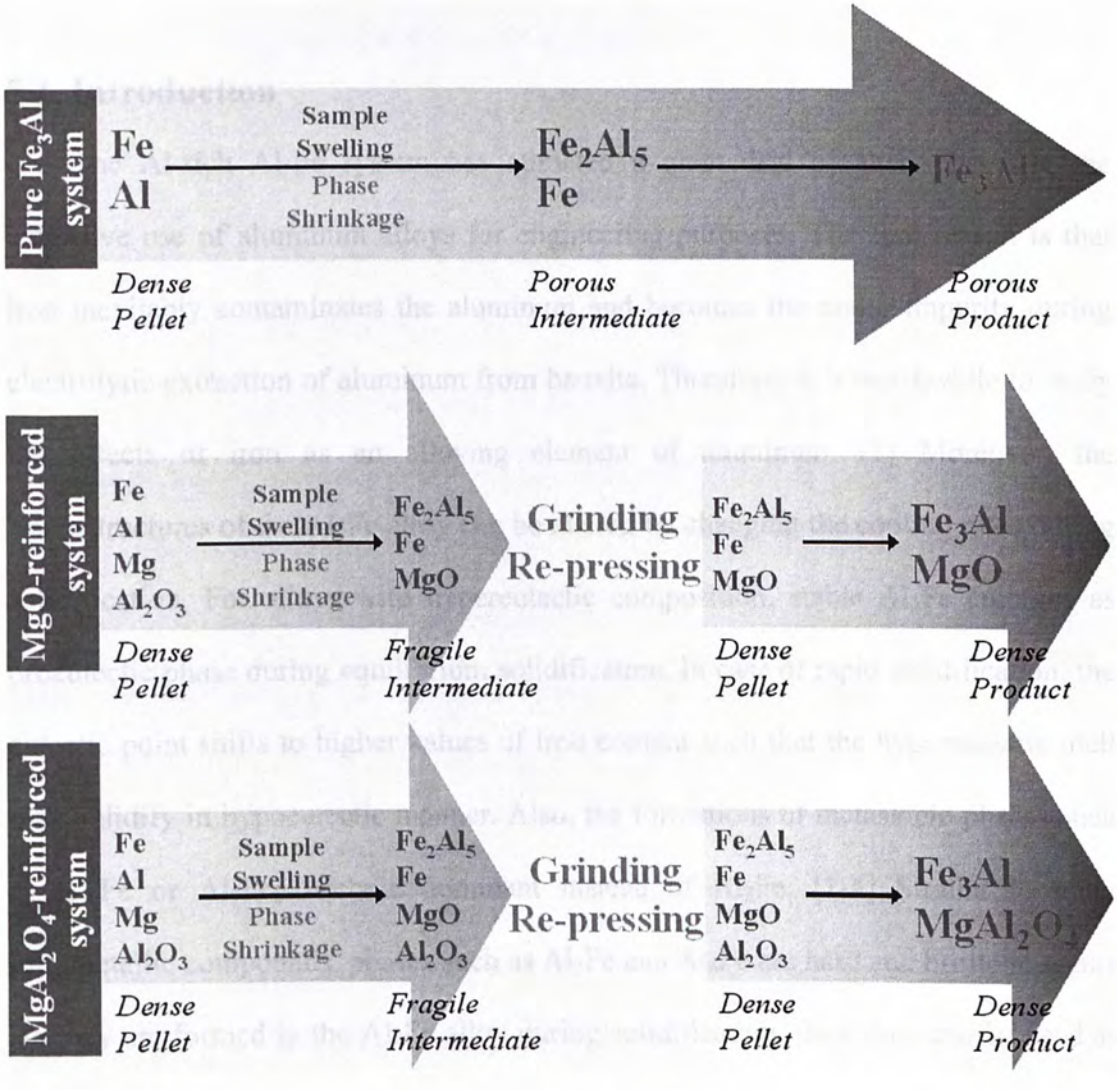

Fig. 4.27. Schematic diagrams comparing the conventional sintering for pure Fe_3Al and two-step sintering for MgO-reinforced / $MgAl_2O_4$ reinforced MMCs.

Chapter 5 Formation of Al-Fe intermetallics in Al-based MMC

5.1. Introduction

The Al-rich Al-Fe system has attracted a great deal of attentions after the extensive use of aluminum alloys for engineering purposes. The first reason is that iron inevitably contaminates the aluminum and becomes the major impurity during electrolytic extraction of aluminum from bauxite. Therefore, it is worthwhile to study the effects of iron as an alloying element of aluminum. [1] Moreover, the microstructures of the Al-Fe alloy can be altered by changing the cooling rates during solidification. For alloys with hypereutectic composition, stable Al_3Fe emerges as proeutectic phase during equilibrium solidification. In case of rapid solidification, the eutectic point shifts to higher values of iron content such that the hypereutectic melt may solidify in hypoeutectic manner. Also, the formations of metastable phases such as Al_6Fe or Al_9Fe_2 become dominant instead of Al_3Fe. [1-4] Similar to other intermetallic compounds, phases such as Al_3Fe and Al_6Fe are hard and brittle in nature. As they are formed in the Al-Fe alloy during solidification, thus, they can be used as in-situ reinforcements. In addition, the cooling conditions would affect the size and distribution of the reinforcements, which are closely related to the mechanical properties of the resulting products. For instance, when they form plate-like structures in the matrix, they would act as stress concentration defects which deteriorate the tensile properties. [1] In contrast, if they are small in size and evenly distributed in the matrix, they would strengthen the matrix by impeding the dislocation movements. [5]

Recently, there were several studies on reducing the size of Al-Fe intermetallics by rapid solidification techniques. Lendvai et al. [4], Lee et al. [6], Seo et al. [7],

Liang et al.[8] and Jones et al. [9] have done that by mold casting plasma spraying, droplet emulsion, water quenching, and splat cooling techniques, respectively. An alternative method to miniaturize the Al-Fe intermetallics is the addition of elements such as manganese, magnesium, sodium or lithium. However, the formations of other side-products limited the development of this method. [1,10]

In this work, the Al-based MMC reinforced by Al_2O_3 particles and Al-Fe intermetallics was produced by sintering of an Al-Fe_3O_4 mixture. The displacement reactions between Al and Fe_3O_4 took place and hypereutectic liquid (Al, Fe) containing Al_2O_3 particles was obtained. The liquid was solidified by furnace-cooling or NaCl-solution-quenching. This chapter reports the fabrication and characterization of this MMC. A model is proposed to describe the displacement reaction between Al and Fe_3O_4 during sintering and explain the phase transformation of the Al-Fe intermetallics during solidification. Results of hardness measurements of samples solidified with different cooling conditions are also presented.

5.2. Experiments

Commercial powders of aluminum (99.7% purity, <44 μm, Strem) and iron(II,III) oxide (98% purity, <5 μm, Aldrich) were used as the reactants in this work. Al-Fe_3O_4 mixture with a molar ratio of 299:3 was cold-pressed into 3-mm-thick pellets with a diameter of 10 mm. Liquid (Al, Fe) with 97 at% Al and 3 at% Fe (hypereutectic composition) containing Al_2O_3 particles was expected to form at elevated temperature after the occurrences of displacement reactions between Al and Fe_3O_4.

A piece of green sample was analyzed by the DTA to determine the temperatures at which the chemical reactions between Al and Fe_3O_4 took place. After DTA, the green samples were being sintered separately in a tube furnace for 1 h in argon atmosphere at different temperatures, which corresponded to the DTA trough/peak

positions. In order to study the effects of cooling rate on the microstructures and hardness of the sintered sample, the sample was cooled down to room temperature by furnace-cooling, or by NaCl-solution-quenching from 700 or 900°C. XRD was used to identify the phases in the sintered samples. Microstructures of the samples were investigated by SEM and TEM, while elemental analyses were conducted EDS.

5.3. Results and discussion

5.3.1. DTA and XRD results

Fig. 5.1 shows the DTA results of the Al-Fe_3O_4 sample. In the heating curve, the endothermic trough at ~660°C corresponded to the melting of Al was observed, and two broad exothermic peaks were observed at ~768 and ~1020°C. In the cooling curve, an exothermic peak at ~640°C corresponded to the solidification of the melt. Based on these results, the samples were being sintered separately for 1 h at 720, 840 and 1100°C before they were furnace-cooled to room temperature.

Fig. 5.2 shows the XRD patterns of the green sample and the sintered samples. The 2θ angles and intensities of the obtained diffraction patterns were matched with the standard patterns from JCPDS - International Centre for Diffraction Data for phase identifications. A summary of the XRD results is listed in Table 5.1. Peaks in the pattern of the green sample corresponded to those of Al and Fe_3O_4. In the pattern of the sample sintered at 720°C, Fe_3O_4 peaks disappeared and only those corresponding to Al were observed. The absence of Fe_3O_4 peaks indicated that it had been reduced by Al to form poorly crystalline phases. Al_3Fe peaks were identified for the sample sintered at 840°C, their appearance implied that some Fe had been produced via the displacement reactions between Al and Fe_3O_4. Peaks corresponding to Al, Al_3Fe and Al_2O_3 were found in the sample sintered at 1100°C, it suggested that the displacement reactions were completed and formed Fe and Al_2O_3. From these

results, it was reasonable to deduce that Fe_3O_4 was firstly reduced by Al to form poorly crystalline FeO and Al_2O_3. FeO was then further reduced to form Al_2O_3 and Fe, which dissolved in molten Al and formed Al_3Fe during solidification. This deduction would be justified in latter sessions.

5.3.2. SEM, TEM and EDS results

5.3.2.1. Green sample

The SEM micrographs of the green Al-Fe_3O_4 compact at different scales are shown in Fig. 5.3. The small-scale micrograph (Fig. 5.3a) revealed that the matrix was consisted of Al grains (dark), which have a size distribution from a few microns to tens of microns. From the large-scale micrograph (Fig. 5.3b), bright Fe_3O_4 particles with size smaller than 1 μm were located at the Al grain boundaries.

5.3.2.2. Furnace-cooled samples

5.3.2.2.1. Sample sintered at 720°C

Fig. 5.4 are SEM micrographs that shows the microstructures of the sample sintered at 720°C, which are similar to that of the green sample (Fig. 5.3) The enlarged view of the sample (Fig. 5.4b) revealed the presence of white particles with sub-micron size at the Al grain boundaries. Due to the small sizes of the white particles, they could not be analyzed by EDS individually, however, the EDS results indicated that Al, Fe and O were present at the grain boundaries. Since the Fe_3O_4 peaks were absent in the XRD spectrum (Fig. 5.2), a possible explanation was that some Fe_3O_4 had reacted with Al and formed FeO and Al_2O_3, which were poorly crystalline at that temperature.

5.3.2.2.2. Sample sintered at 840°C

Fig. 5.5 shows the SEM micrographs of the sample sintered at 840°C. The size of white particles increased to ~a few microns and some of them were located in the Al grains. The EDS analyses revealed that they had composition of ~40 at% Al and ~60

at% O. Some gray plates with length up to tens of microns and thickness smaller than 10 μm were observed. Also, some gray particles with sub-micron size were found at the Al grain boundaries. The gray plate consisted of ~75 at% Al and ~25 at% Fe while the gray particle contained ~50 at% Fe and ~50 at% O according to the EDS results. With reference to the XRD patterns (Fig. 5.2), it was apparent that the white particles, gray plates and gray particles were Al_2O_3, Al_3Fe and FeO, respectively. These results supported our deduction that some FeO further reacted with Al to form Fe.

5.3.2.2.3. Sample sintered at 1100°C

The SEM micrograph of the furnace-cooled sample sintered at 1100°C is shown in Fig. 5.6a. Comparing it with that sintered at 840°C (Fig. 5.5), several differences were noticed. First, the coalescence of Al grains was observed and the FeO located at the grain boundary disappeared. Second, the number of Al_2O_3 particles was increased dramatically and they distributed uniformly in the Al matrix. Moreover, the size of proeutectic Al_3Fe plates increased and they had length up to hundreds of microns and thickness of ~200 μm. Fig. 5.6b is the enlarged micrograph showing the microstructures of a proeutectic Al_3Fe plate. The EDS analyses on the Al_3Fe plate (Fig. 5.7) indicated that it consisted of ~75 at% Al and ~25 at% Fe. It was noticeable that some Al_2O_3 particles and defects such as cracks and voids were observed in the Al_3Fe plate, and the number of defects increased with increasing polishing time. The possible reasons were that Al_3Fe was hard and brittle and its wetting with Al_2O_3 was poor, brittle fracture and detachments of Al_2O_3 occurred during polishing. The divorced eutectic Al_3Fe was also found and the microstructure is shown in Fig. 5.6c. Their lengths were estimated to be ~hundred of microns with thickness of ~a few microns. Obviously, the displacement reactions between Al and Fe_3O_4 had been completed after sintering at 1100°C, Al_2O_3 and Fe were formed as products. The Fe dissolved in the molten Al, and the resulting (Al, Fe) liquid formed Al_3Fe phases

during solidification.

5.3.2.3. NaCl-solution quenched samples

In order to study the effects of cooling rate on the microstructures, two other samples were sintered at 1100°C for an hour, and then quenched by NaCl-solution when the temperature of the sample had dropped to 700°C and to 900°C. The XRD results of these samples were similar to that of the furnace cooled sample, where Al, Al_3Fe and Al_2O_3 were identified. However, it was found that the microstructures of these samples were significantly different from the furnace-cooled counterpart.

5.3.2.3.1. Sample quenched from 700°C

The SEM micrograph of the sample quenched from 700°C is shown in Fig. 5.8a. The sample was etched with 0.1M NaOH solution for 1 min. Similar to the furnace-cooled sample sintered at 1100°C (Fig. 5.6a), Al_2O_3 particles having size of ~a few microns and proeutectic Al_3Fe plates with length up to hundreds of microns and thickness of ~200 μm were found in the Al matrix. Figs. 5.8b-c are the enlarged micrographs showing the microstructures of a proeutectic Al_3Fe plate and the matrix. The proeutectic Al_3Fe plate was similar to that of the furnace-cooled sample (Fig. 5.8b). However, Al dendrites instead of divorced eutectic Al_3Fe were found in the matrix. The micrographs taken with higher magnifications (Figs. 5.8d-e) revealed that the dendritic spacing was ~a few microns and duplex phases with lamellar structures were located in the inter-dendritic regions.

To further investigate the duplex phases, thin foils obtained from the sample were examined by TEM. Fig. 5.9a is the bright-field TEM image of the dendritic region. The corresponding selected area electron diffraction (SAED) patterns (Figs. 5.9b-c) taken with different camera lengths revealed some diffraction rings, the calculated lattice parameters matched with those of Al and Al_6Fe phases. [12] Therefore, the duplex phases were characterized to be Al-Al_6Fe eutectics. From the

enlarged views of the eutectics (Figs. 5.9d-e), the size of the Al-Al_6Fe lamellae was in nano-scale with an average thickness of ~100 nm. A lamella appeared dark was analyzed by EDS using an electron beam with size of ~50 nm, the spectrum is shown in Fig. 5.10 and the quantified result indicated that it contained ~85 at% Al and ~15 at% Fe. It was apparent that the bright phases and dark phases in the eutectic regions corresponded to Al and Al_6Fe, respectively.

5.3.2.3.1. Sample quenched from 900°C

Figs. 5.11a-c show the SEM micrographs with different magnifications of the sample quenched from 900°C. The sample was etched with 0.1M NaOH solution for 1 min. By comparing with the furnace-cooled and 700°C-quenched sample, it was noted that the proeutectic Al_3Fe appeared as phases with irregular shapes instead of plate-like form. The size of proeutectic Al_3Fe ranged from a few to tens of microns, which were much smaller than the plate-like counterparts. Al_2O_3 particles with size of ~a few microns and Al_3Fe phases were distributed uniformly in the Al matrix. Fig. 5.11d is the enlarged micrographs showing the microstructures of the matrix. Two distinct microstructures were observed, the region further away from the proeutectic Al_3Fe was labeled as region A, and that adjacent to the proeutectic Al_3Fe was labeled as region B. SEM micrographs were taken from these two regions with higher magnifications (Figs. 5.11e-f). Region A contained some tiny bright phases embedded in the dark background, which was identified to be Al by EDS. However, the microstructures were too small to be resolved by the SEM. The microstructure of region B was similar to that of the matrix of the sample quenched at 700°C (Fig. 5.8d), it consisted of Al dendrites with dendritic spacing of ~a few microns, and duplex phases with lamellar structures were located in the inter-dendritic regions.

TEM having higher resolving power than SEM was used to further characterize regions A and B of the 900°C-quenched sample. Fig. 5.12a shows the bright-field

TEM image of region A. The SAED patterns (Figs. 5.12b-c) taken from this region showed rings corresponding to Al and Al_6Fe. [12] Hence, region A was identified to be Al-Al_6Fe eutectics. From the enlarged images of the eutectics taken with different orientations relative the electron beam (Figs. 5.12d-e), the Al_6Fe phases (dark) in the eutectics were found to possess rod-like structure. The length of the Al_6Fe rods was ~hundreds of nm and the diameter was ~tens of nm.

To study the crystallographic orientation relationships between the Al phase and Al_3Fe nano-rods in region A, converging beam electron diffraction (CBED) patterns (using an electron beam with size of ~30 nm) were taken from a Al_6Fe rod and adjacent Al phase, the corresponding TEM image is shown in Fig. 5.13a, where the Al_6Fe rod was parallel to the electron beam. The CBED pattern of the Al_6Fe rod (Fig. 5.13b) indicated that the preferential growth direction of the Al_6Fe rod was <001>, which was consistent with the study on chill-cast hypereutectic Al-Fe alloys by Burden et al.[13] The zone axis of adjacent Al phase was found to be [001] according to the CBED pattern shown in Fig. 5.13c. It was noted that the growth direction of the Al_6Fe rod was not exactly aligned with the crystal planes of Al pattern as the CBED pattern of Al_6Fe was not perfectly symmetric, this result was coherent with the microstructures shown in Fig. 5.12a.

In the selected area electron diffraction (SAED) pattern (Fig. 5.13d) of the circled area of the TEM image (Fig. 5.13a), two sets of diffraction patterns were indexed: one belongs to the Al_6Fe rod while the other to the Al phase. The crystallographic orientation relationships between them were found to be

$$Al[001] // Al_6Fe[00\bar{1}] \; ; \; Al(00\bar{2}) // Al_6Fe(310)$$

Adam et al. [14] and Jacobs et al. [15] had used TEM to study the Al-Al_6Fe eutectic structures of unidirectionally solidified hypoeutectic Al-Fe ingots and splat-quenched

hypereutectic Al-Fe alloys, respectively. The crystallographic orientation relationships between Al and Al_6Fe revealed by the two studies were identical, and the results were

$$Al[011] // Al_6Fe[001] \ ; \ Al(00\bar{2}) // Al_6Fe(310)$$

The relationship of the crystal planes was the same while that of the crystal directions was different compared with our results. Such discrepancy might be attributed to one or more of the following factors: compositions of the Al-Fe alloys; cooling conditions of the samples; morphologies of the Al-Al_6Fe eutectics; or the presence of phases such as Al_2O_3 particles in our samples. At present, details of these effects on the orientation relationships have not been clarified and further investigations are needed.

Fig. 5.14a shows the bright-field TEM image of region B. Al dendrites with Al-Al_6Fe eutectics were observed adjacent to the proeutectic Al_3Fe phase having irregular shape. The enlarged image of the region B (Fig. 5.14b) revealed that the dendritic spacing was ~a few microns and the Al-Al_6Fe lamella had an average thickness of ~100 nm. In fact, the microstructure of region B was quite similar to that of the matrix of the 700°C-quenched sample (Fig. 5.9d), however, the spacings of Al dendrites were less uniform and the lamellar structures of Al-Al_6Fe eutectics were less prominent.

5.3.3. Reaction mechanisms

Taking all the results of DTA, XRD and those from the microstructural and elemental analyses into consideration, it is possible to postulate the reactions that occurred during sintering.

From the SEM micrograph (Fig. 5.3), it confirmed that the green sample was composed of Al grains with Fe_3O_4 particles located at the Al grain boundaries. When the sample was heated to the temperature where the DTA trough was located (660°C), Al powder melted and but no chemical reaction occurred at this stage. When the

sample was heated to temperatures where the first DTA peak (~720-830°C) was located, the reaction between Al and Fe_3O_4 occurred, which formed poorly crystalline Al_2O_3 and FeO. The SEM micrographs of the sample sintered at 720°C (Fig. 5.4) revealed the status where the first-step displacement reaction had just been triggered, some newly formed Al_2O_3 particles were observed in the Al/Fe_3O_4 interfaces. Although Al was in its liquid state at 720°C, the reaction products were confined in the grain boundaries due to the low viscosity of the molten Al. As the reactant mixture were Al and Fe_3O_4 with a ratio of 299:3, the step-one reaction could be described by the following equation

$$299Al_{(l)} + 3Fe_3O_{4(s)} \rightarrow 297Al_{(l)} + 9FeO_{(s)} + Al_2O_{3(s)} \ldots\ldots (5.1)$$

where the subscripts s and l refer to the solid and liquid form of the substance, respectively. By sintering the sample near temperature where the second DTA peak was found (~840-1090°C), the step-two displacement reaction occurred, and FeO was further reduced by Al to form Al_2O_3 and Fe, which dissolved into the molten Al to form liquid (Al, Fe) with hypereutectic composition. The initial status of the step-two displacement reaction was shown in the SEM micrograph of the sample sintered at 840°C (Fig. 5.5). The presences of Al_3Fe plates and growths of Al_2O_3 particles indicated that some Fe and Al_2O_3 had formed as products of the reaction. Because the viscosity of the molten Al at this stage was relatively higher than that at 720°C, so the Al_2O_3 particles migrated into the molten Al grains. The step-two reaction and the formation of liquid (Al, Fe) with hypereutectic composition could be described by the following equations

$$297Al_{(l)} + 9FeO_{(s)} + Al_2O_{3(s)} \rightarrow 291Al_{(l)} + 9Fe_{(s)} + 4Al_2O_{3(s)} \ldots\ldots (5.2)$$

$$291Al_{(l)} + 9Fe_{(s)} + 4Al_2O_{3(s)} \rightarrow (Al, Fe)_{(l,\ \text{hypereutectic composition})} + 4Al_2O_{3(s)} \ldots\ldots (5.3)$$

With reference to the thermodynamic data of Barin et al., [16] the enthalpy changes of

reactions 5.1 and 5.2 were calculated to be -89 and -266 J/g. The values obtained by measuring the areas of the first and second exothermic peaks in the DTA curve (Fig. 5.1) were -97 and -301 J/g. The agreement of the two sets of values (error< 10%) further supported our proposed mechanisms.

5.3.4. Phase transformation in solidification

According to equation 5.3, the amount of Al in the liquid (Al, Fe) was ~3 at%. With reference to the Al-Fe binary phase diagram (Fig. 5.15), liquid (Al, Fe) with such Al content is hypereutectic. When the liquid was being cooled at equilibrium condition, Al_3Fe having the highest melting point among all possible phases emerged as proeutectic phase at ~770°C, and Al_3Fe phase continued to grow until the temperature had dropped to 655°C. After the formation of proeutectic Al_3Fe, the liquid reached the eutectic composition, and eutectic transformation took place at a temperature depending on the undercooling ΔT. The transformations can be described by the following expressions

$$(Al, Fe)_{(l,\ \text{hypereutectic composition})} \rightarrow (Al, Fe)_{(l,\ \text{eutectic composition})} + Al_3Fe_{(s,\ \text{proeutectic})} \quad \ldots\ldots (5.4)$$

$$(Al, Fe)_{(l,\ \text{eutectic composition})} \rightarrow (Al - Al_3Fe)_{(s,\ \text{eutectic})} \quad \ldots\ldots (5.5)$$

For the furnace-cooled system, the cooling rate was slow enough ($\leq$ 5°C/min) that the model of equilibrium phase transformation can be applied to explain the formation of proeutectic Al_3Fe plates and Al-Al_3Fe eutectics. It was interesting that the divorced eutectic formed instead of normal eutectic having lamellar structures. The studies by Yu et al. [17] on Al-Ni system and Norman et al. [18] on Al-Sc alloy postulated that when the difference in fractional volume between the two components in the eutectic was large, the eutectic tended to grow into divorced form. In our Al-Fe system, the volume fraction of Al_3Fe in the eutectic was calculated to be ~3%.

Moreover, undercooling ($\Delta T \sim 15^{\circ}C$) was revealed in the DTA cooling curve (Fig. 5.1), it implied that an extra amount of Fe was consumed to form proeutectic Al_3Fe plate, this further reduced the volume fraction of Al_3Fe in the eutectic. The SEM micrograph of the furnace-cooled sample sintered at 1100°C (Fig. 5.6a) confirmed that the amount of Al was much more than that of Al_3Fe in the eutectic. Thus, the Al-Al_3Fe eutectic in our furnace-cooled sample solidified in divorced form. The thermodynamic driving force of forming divorced eutectic is to minimize the interfacial energy between the two components. [17] Obviously, the Al-Al_6Fe surface area could be reduced with divorced form. However, as its formation required the components to move a longer distance than that of normal eutectic, [5] therefore, it was not observed in the NaCl solution-quenched samples, which were solidified rapidly and long distance diffusions of components were impossible.

As we mentioned before, the rapid solidification technique can alter the microstructures of the hypereutectic Al-Fe alloys by: shifting the eutectic point to higher values of iron content such that the hypereutectic melt may solidify in hypoeutectic manner; suppressing the formations stable Al_3Fe phase and leading to the formations of metastable phases such as Al_6Fe or Al_9Fe_2. For the sample quenched at 700°C, proeutectic Al_3Fe plates formed in the same way as the furnace-cooled sample during cooling from 770 to 700°C. When the sample was being cooled by NaCl solution from 700°C to room temperature, the liquid (Al, Fe) solidified in hypoeutectic manner and Al dendrites were formed. The subsequent growths of Al dendrites had two effects: Al from the liquid was taken up by the dendrites and the Fe content of the liquid increased; the liquid pushed towards the interdendritic regions. Eventually, the liquid reached the eutectic composition and formed Al-Al_6Fe eutectic in the interdendritic regions. For the sample quenched at 900°C, as the quenching temperature was higher than the liquidus temperature indicated by the Al-Fe phase

diagram (Fig. 5.15), such that the proeutectic Al_3Fe formed abruptly and appeared as phases with irregular shape. Their sizes were much smaller than the plate-like counterparts, and they distributed more uniformly in the matrix. The formation of proeutectic Al_3Fe consumed Fe in the surrounding liquid. Because the liquid was rapidly cooled, the concentration gradient of Fe in the liquid could not be completely eliminated by atomic diffusion before solidification took place. The liquid further away from the Al_3Fe was Fe-rich, it solidified in eutectic manner and formed Al-Al_6Fe eutectics (region A); the Fe-deficient liquid adjacent to the proeutectic Al_3Fe solidified similarly to the 700°C-quenched sample, and Al dendrites with Al-Al_6Fe eutectic in the interdendritic regions (region B) were formed.

5.3.5. Microhardness

Hardness measurements were performed on both furnace-cooled and NaCl-solution quenched samples sintered at 1100°C. The Vickers hardness numbers (VHNs) were obtained by a microhardness tester with 2000gf load indenter at room temperature. Each value reported was an average of 10 points selected randomly from different positions of the sample. The results were presented in Table 5.2 and the optical micrographs of the indents on the samples are shown in Fig. 5.16. The VHN of the furnace-cooled sample was 42±21, and those of samples quenched from 700 and 900°C were 68±20 and 78±8, respectively. It was obvious that the rapid-cooled samples possessed higher VHNs, and this was resulted from the refinements of Al phases. According to the Hall-Petch equation, [19] a fine-grained polycrystalline material is harder and stronger than one that is coarse-grained, since it has a greater grain boundary area to impede dislocation motion during plastic deformation. In the quenched samples, Al formed fine dendrites (dendritic spacing of ~a few μm) instead of large grains. In addition, the nano-scale Al-Al_6Fe lamellae in the interdendtrite regions and the Al_6Fe nano-rods in the eutectic acted as physical barriers to hinder the

dislocations from moving. Furthermore, the standard deviations in measurements of the furnace-cooled and 700°C-quenched samples were exceptionally large because of the presences of large proeutectic Al_3Fe plates in the matrix. In contrast, the standard deviation the 900°C-quenched sample was much smaller due to the fact that the proeutectic Al_3Fe phases were miniaturized and distributed more evenly in the matrix.

5.4. Conclusions

The Al-based MMC was synthesized by sintering of an Al-Fe_3O_4 mixture. The two-step displacement reaction between Al and Fe_3O_4 took place at 1100°C. Liquid (Al, Fe) with hypereutectic composition containing Al_2O_3 particles was obtained. The liquid was cooled down to room temperature by furnace-cooling, or by NaCl-solution-quenching from 700 or 900°C. The microstructures of the MMC products varied with different cooling conditions. For the furnace-cooled sample, proeutectic Al_3Fe plates, divorced eutectic Al_3Fe and Al_2O_3 particles were found in the Al matrix. For the sample quenched from 700°C, Al dendrites with dendritic spacing of ~a few μm were formed and Al-Al_6Fe eutectic was found in the inter-dendritic regions. For that quenched from 900°C, the size of proeutectic Al_3Fe phases was reduced to ~tens of μm. The Fe-rich liquid solidified by eutectic transformation and Al-Al_6Fe eutectic containing Al_6Fe nano-rods was formed, while the Fe-deficient liquid solidified in hypoeutectic manner and dendritic structures similar to that quenched from 700°C were formed. Moreover, the microhardness tests indicated that the MMCs were substantially hardened by NaCl-solution quenching. On average, the VHNs of the samples quenched from 700 and 900°C were 62% and 86% higher than that of the furnace-cooled sample.

References

1. C. McL. Adams, C. W. Tan and L. M. Hogan, J. Cryst. Growth, 51 (1981) p. 525-533
2. R. M. K. Young and T. W. Clyne, Scr. Metal. 15 (1981) p. 1211-1216
3. A. Griger, V. Stefániay, E. Kovács-Cseténvi and T. Turmezey, Key Eng. Mater. 44-45 (1990) p. 17-30
4. J. Lendvai, Key Eng. Mater. 44-45 (1990) p. 1-16
5. D. R. Askeland, The science and engineering of materials, PWS Publishing Company, Boston, Third edition, 1994, p. 264-266, 274-275
6. J. M. Lee, S. B. Kanf, T. Sato, H. Tezuka and A. Kamio, Mater. Sci. Eng. A343 (2003) p. 199-209
7. H. S. Seo, W. Y. Yoon, M. H. Kim, E. P. Yoon and K. H. Kim, J. Mater. Sci. 37 (2002) p. 4481-4486
8. D. Liang and H. Jones, Mater. Sci. Eng. A173 (1993) p. 109-114
9. H. Jones, Mater. Sci. Eng. 5 (1969) p.1-18
10. Z. Zhou and R. D. Li, Acta Metall. Sin. 6 (2003) p. 608-612
11. Binary alloy phase diagrams second edition plus updates on CD-ROM, ASM International, USA, 1996
12. Cards 04-0787 and 47-1433, JCPDS, International Centre for Diffraction Data, 12 Campus Boulevard, Newtown Square, PA 19073-3273, U.S.
13. M. H. Burden and H. Jones, Metallography 3 (1970) p. 307-326
14. C. McL. Adam and L. H. Hogan, J. Aust. Inst. Met. 17 (1972) p. 81-90
15. M. H. Jacobs, A. G. Doggett and M. J. Stowell, J. Mater. Sci. 9 (1974) p.1631-1643
16. I. Barin, F. Sauert, E. Schultze-Rhonhof and W. S. Sheng, Thermochemical Data

of Pure Substances, VCH, Weinheim, Federal Republic of Germany, 1989, p. 17, 48, 536, 561, 564-565

17. P. Yu, C. J. Deng, N. G. Ma, and D. H. L. Ng, J. Mater. Res. 19 (2004), p. 1187-1196
18. A. F. Norman, P. B. Prangnell, R. S. McEwen, Acta Mater. 46 (1998) p. 5715-5732
19. W. D. Callister, Jr., Materials science and engineering: an introduction, John Wiley & Sons, New York, Fourth edition, 1997, p. 160-161

Table 5.1. Summary of the XRD results: phases in the Al-Fe_3O_4 green sample and the samples sintered at 720, 840 and 1100°C.

Sample	Phases			
	Al	Fe_3O_4	Al_3Fe	Al_2O_3
Green	√	√		
Sintered at 720°C	√			
Sintered at 840°C	√		√	
Sintered at 1100°C	√		√	√

Table 5.2. Vickers hardness numbers (VHNs) of the furnace-cooled sample, and samples quenched from 700 and 900°C. The hardness were measured by using a 2000 gf load indenter at room temperature.

Sample	VHN
Furnace-cooled	42±21
NaCl-solution-quenched from 700°C	68±20
NaCl-solution-quenched from 900°C	78±8

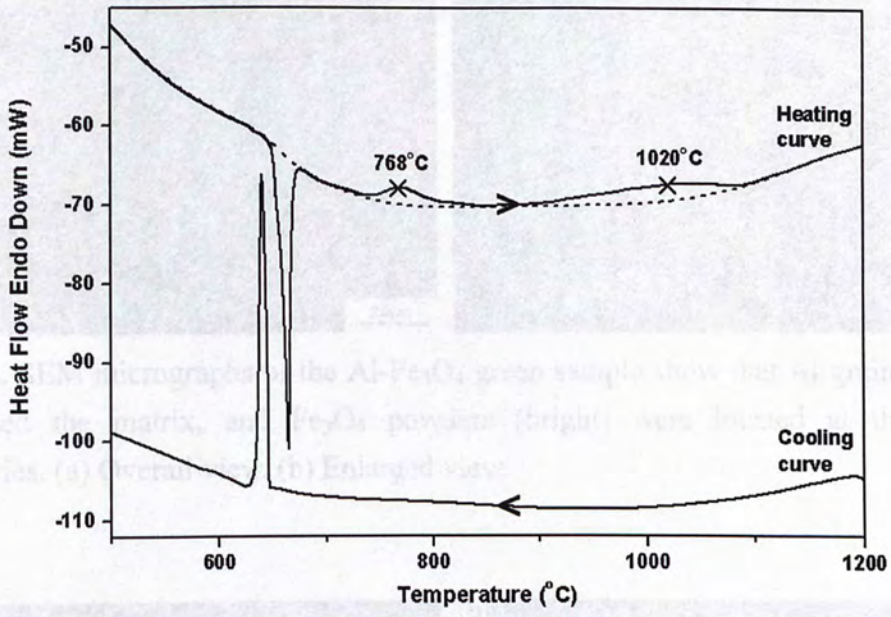

Fig. 5.1. DTA heating curve of the Al-Fe_3O_4 sample (molar ratio of 299:3) shows an endothermic trough and two exothermic peaks at 660, 768 and 1020°C. The changes in enthalpy ΔH related to the two peaks are -97 and -301 J/g, respectively. Cooling curve shows an exothermic peak at 640°C.

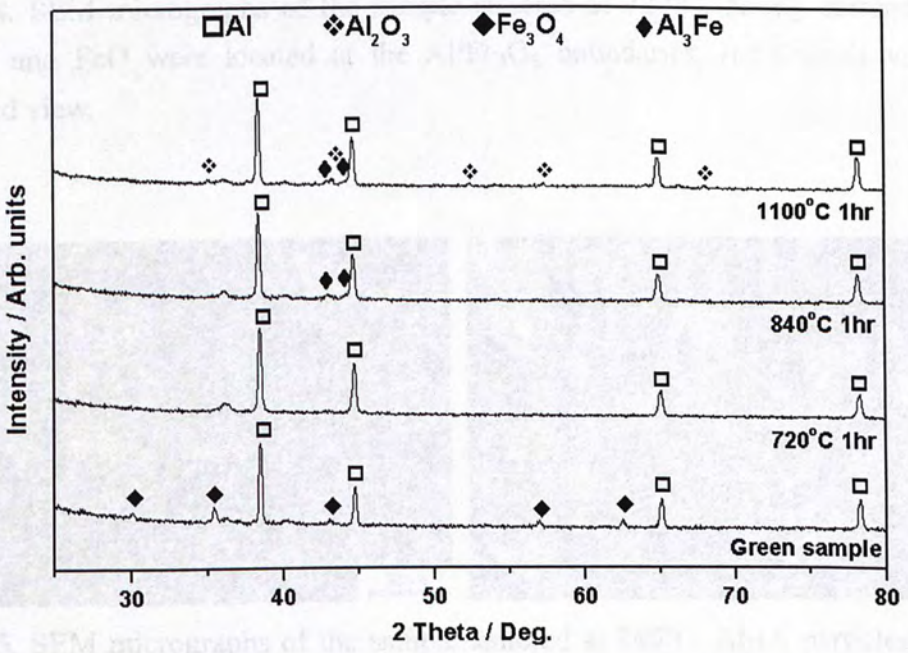

Fig. 5.2. XRD patterns of the green sample and the samples sintered at 720, 840 and 1100°C (peaks at ~36° are background signals).

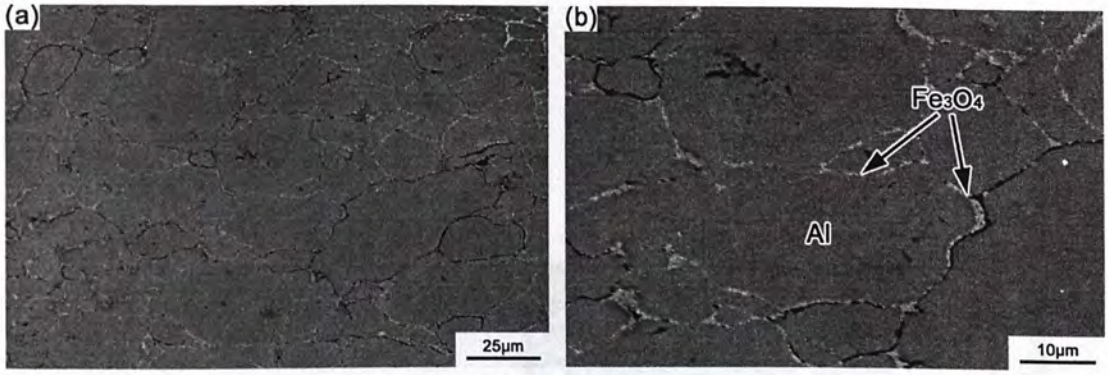

Fig. 5.3. SEM micrographs of the Al-Fe_3O_4 green sample show that Al grains (dark) comprised the matrix, and Fe_3O_4 powders (bright) were located at the grain boundaries. (a) Overall view. (b) Enlarged view.

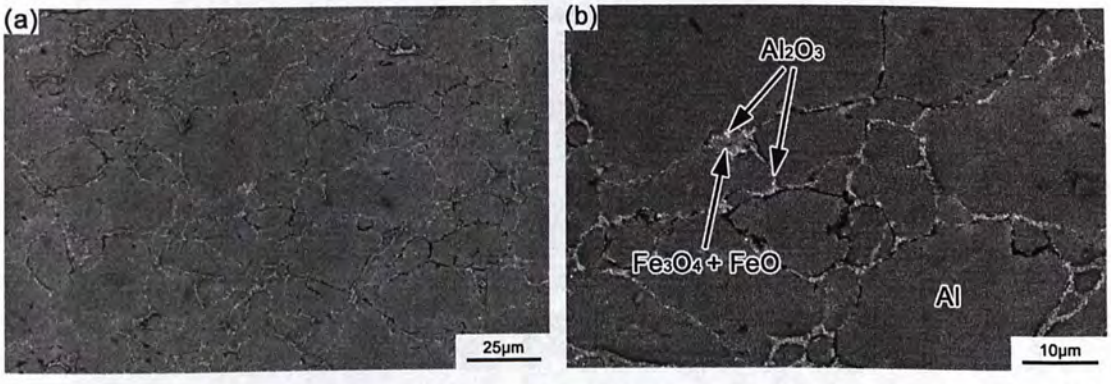

Fig. 5.4. SEM micrographs of the sample sintered at 720°C. Newly formed Al_2O_3 (white) and FeO were located at the Al/Fe_3O_4 boundaries. (a) Overall view. (b) Enlarged view.

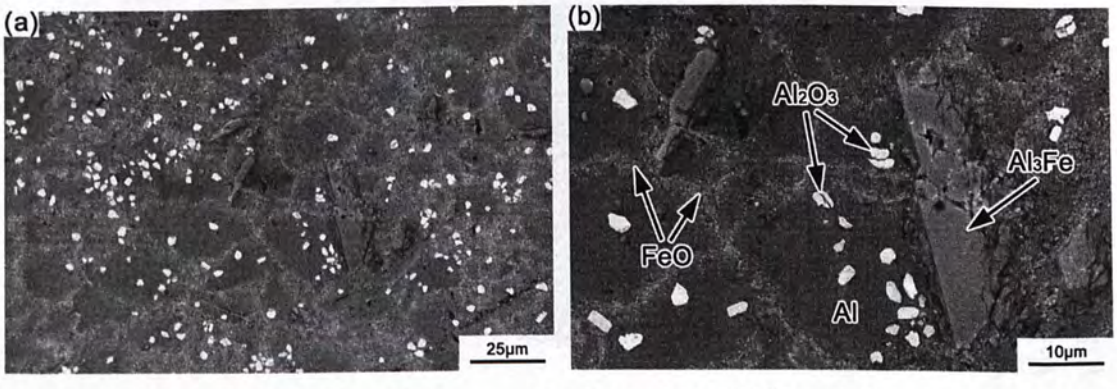

Fig. 5.5. SEM micrographs of the sample sintered at 840°C. Al_2O_3 particles (white) migrated into the Al grains while FeO particles were located at the Al grain boundaries. Some FeO was reduced by Al to Fe, which formed plate-like Al_3Fe (gray) in the Al matrix (dark) during solidification. (a) Overall view. (b) Enlarged view.

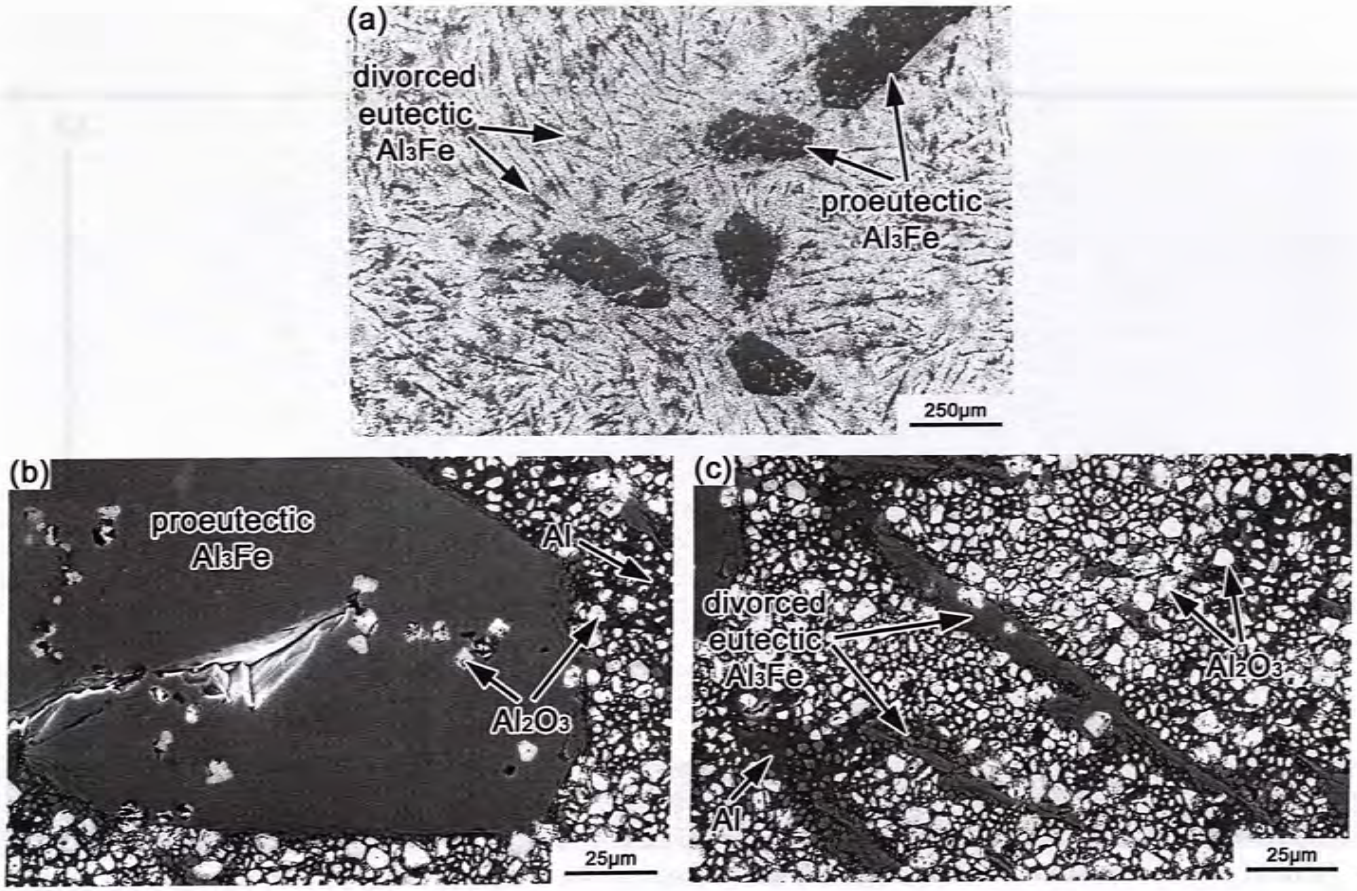

Fig. 5.6. SEM micrographs of the furnace-cooled sample sintered at 1100°C. Al_2O_3 particles (white), proeutectic Al_3Fe plates and plate-like divorced eutectic Al_3Fe were located in the Al matrix. (a) Overall view. (b) Enlarged view of a proeutectic Al_3Fe plate. (c) Enlarged view of the divorced eutectic Al_3Fe.

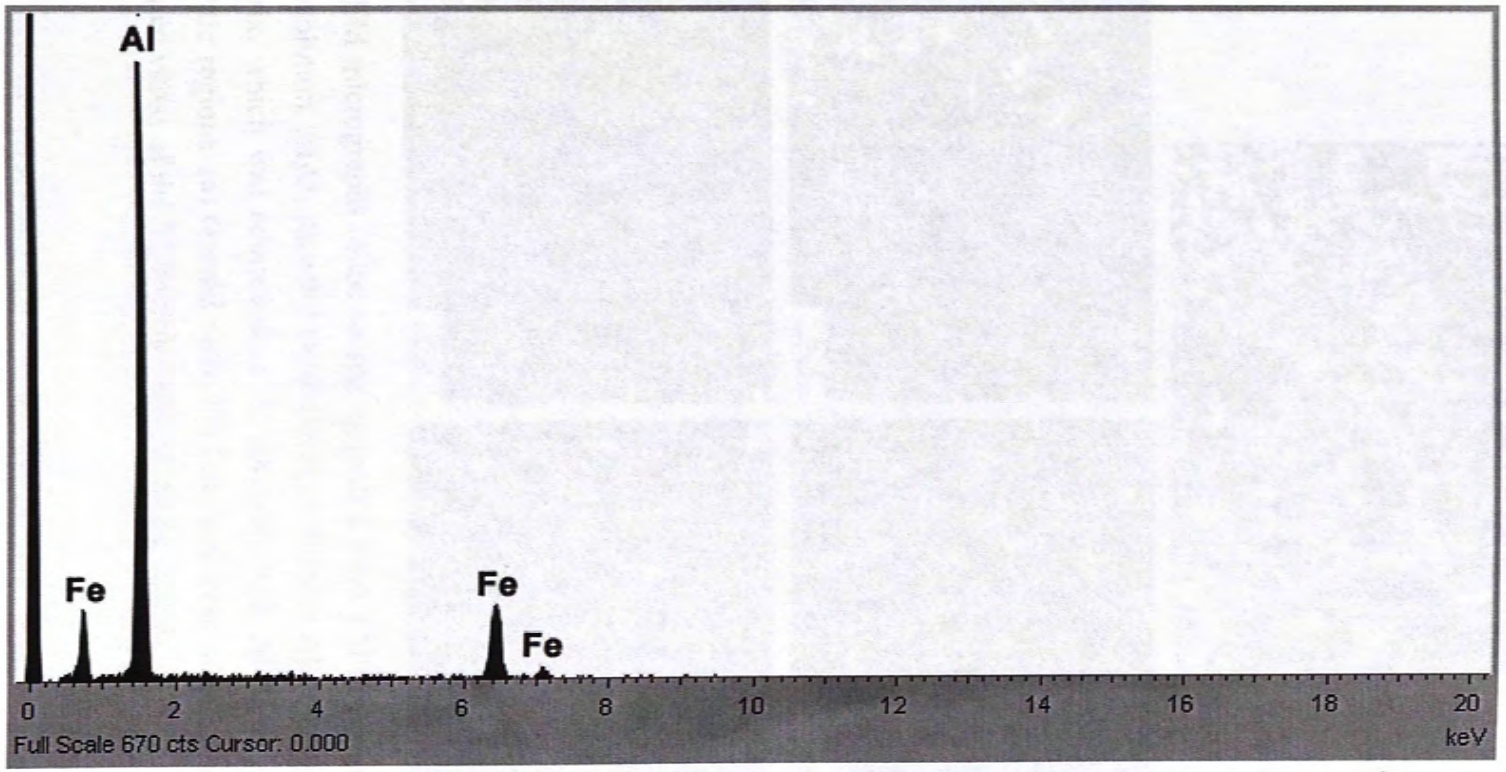

Fig. 5.7. EDS spectrum of the proeutectic Al_3Fe plate of the furnace-cooled sample sintered at 1100°C.

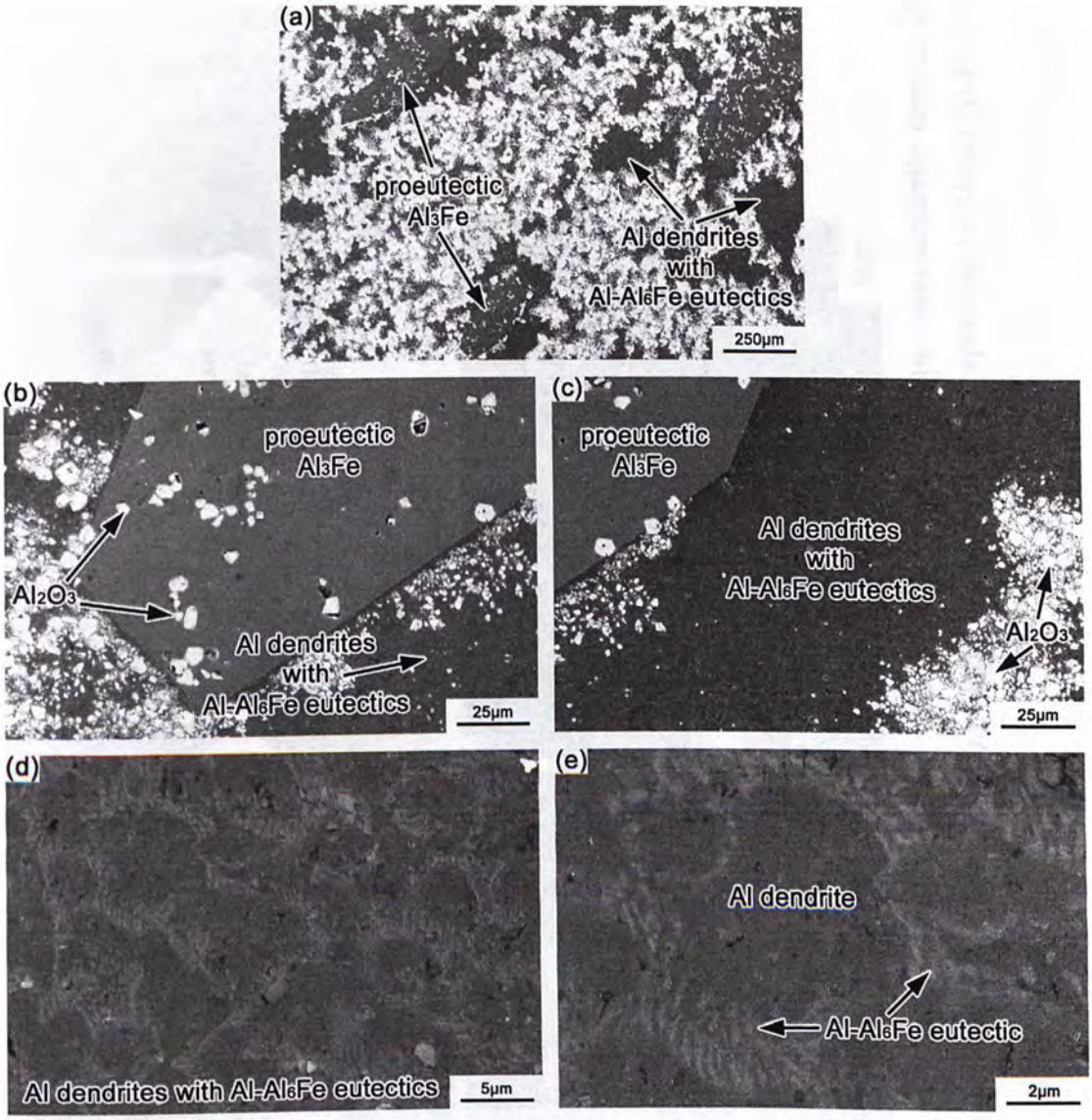

Fig. 5.8. SEM micrographs of the sample quenched from 700°C to room temperature with NaCl-solution. Al_2O_3 particles (white) and proeutectic Al_3Fe plates were located in the matrix, which was composed of Al dendrites with Al-Al_6Fe eutectics in the inter-dendritic regions. (a) Overall view. (b) Enlarged view of the proeutectic Al_3Fe. (c-e) Enlarged views of the Al dendrites and Al-Al_6Fe eutectics.

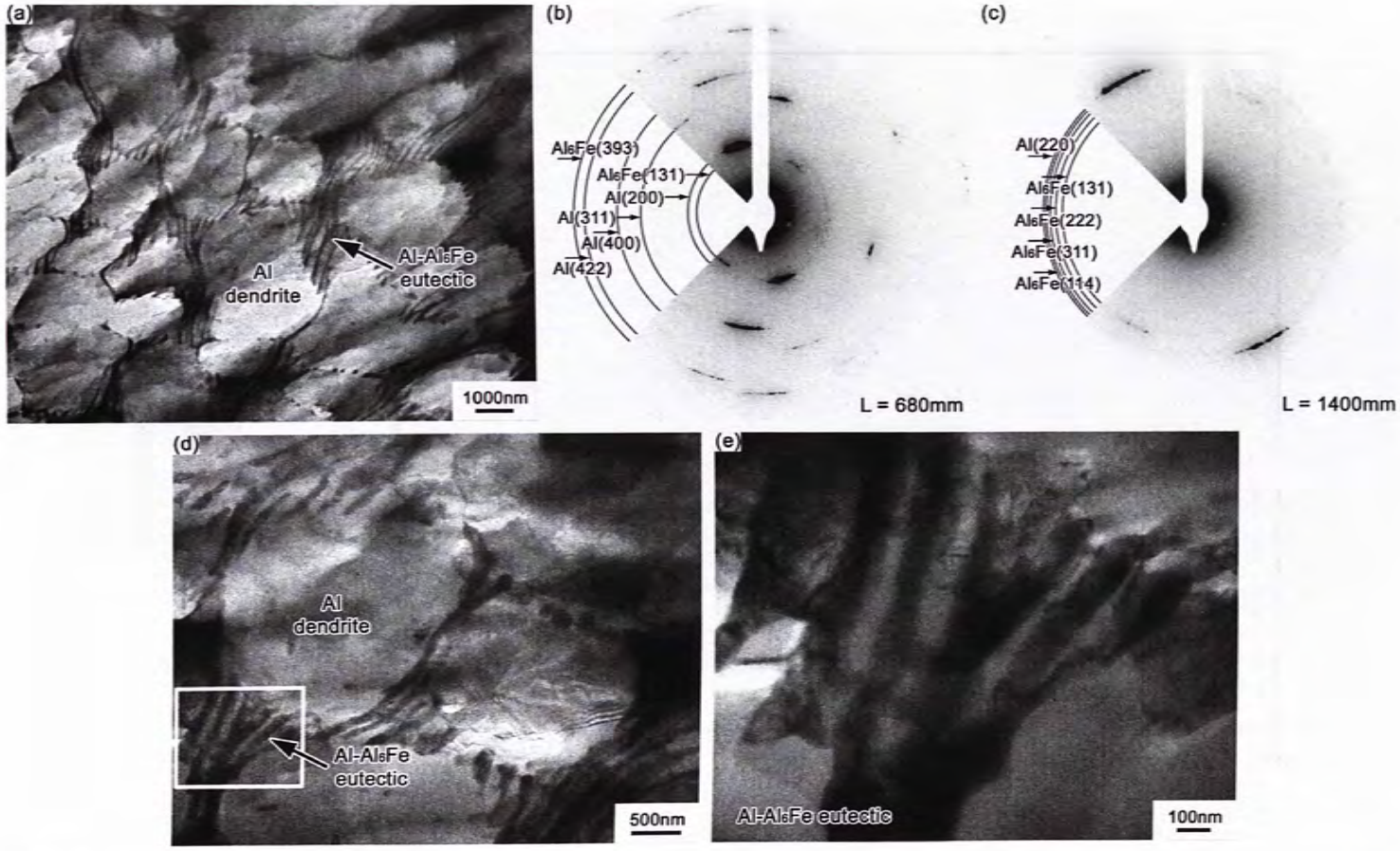

Fig. 5.9. (a) TEM micrograph of the matrix composed of Al dendrites with Al-Al_6Fe eutectics in the inter-dendritic regions of the sample quenched from 700°C. (b-c) The selected area electron diffraction (SAED) patterns revealed rings corresponding to Al and Al_6Fe. (d-e) Enlarged views of the Al-Al_6Fe eutectic.

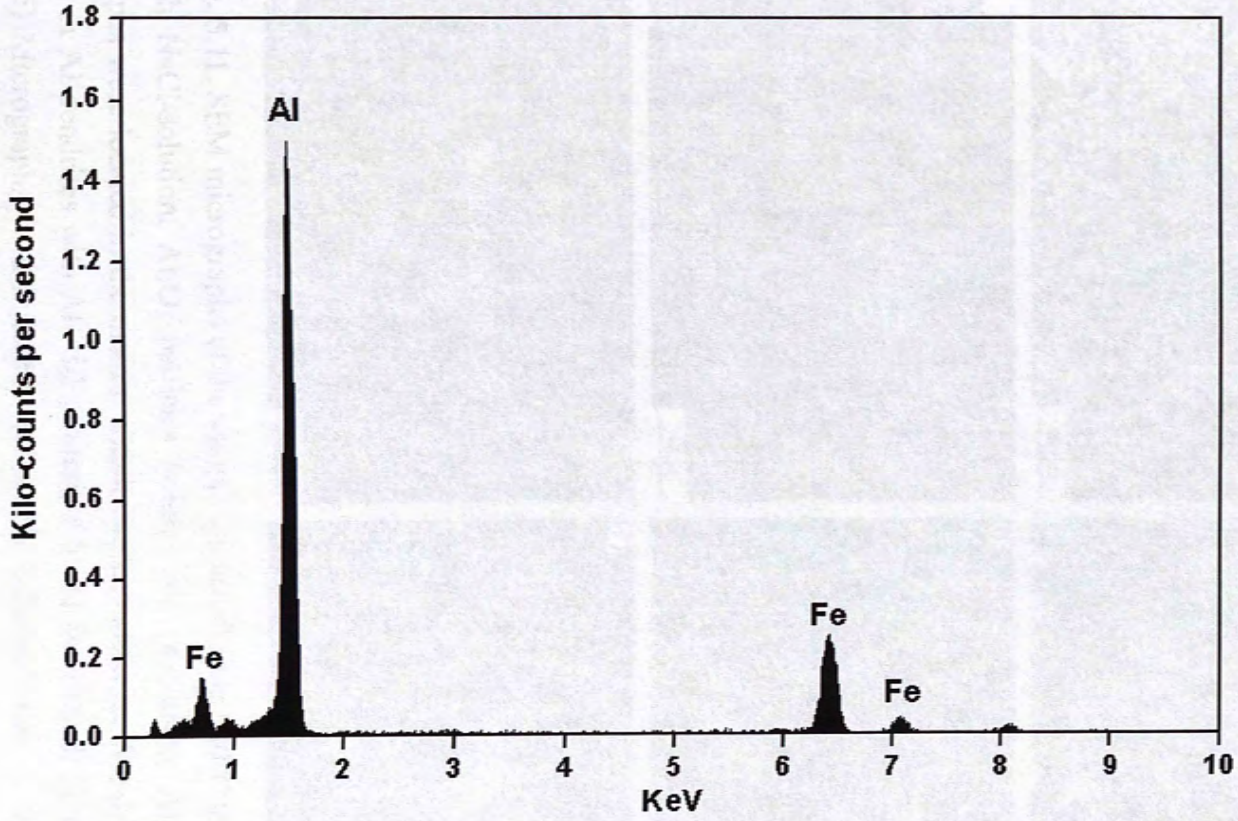

Fig. 5.10. EDS spectrum of the Al_6Fe in the inter-dendritic regions of the sample quenched from 700°C.

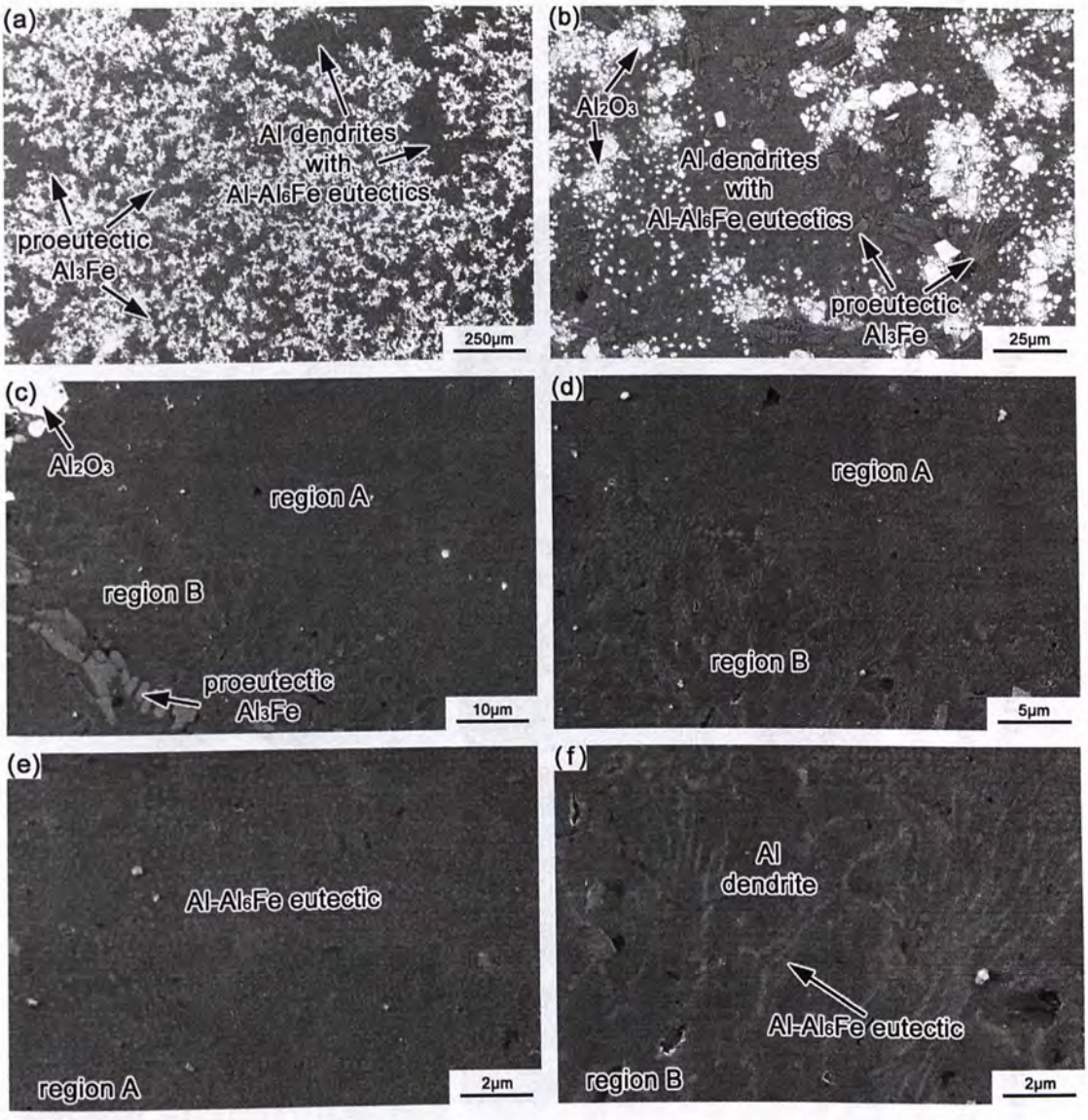

Fig. 5.11. SEM micrographs of the sample quenched from 900°C to room temperature with NaCl-solution. Al_2O_3 particles (white) and proeutectic Al_3Fe with irregular shapes were located in the matrix, which was composed of Al-Al_6Fe eutectic (region A), or Al dendrites with Al-Al_6Fe eutectics in the inter-dendritic regions (region B). (a-c) Micrographs with different scales. (d) Enlarged view of the matrix showing regions A and B. (e) Enlarged view of region A. (f) Enlarged view of region B.

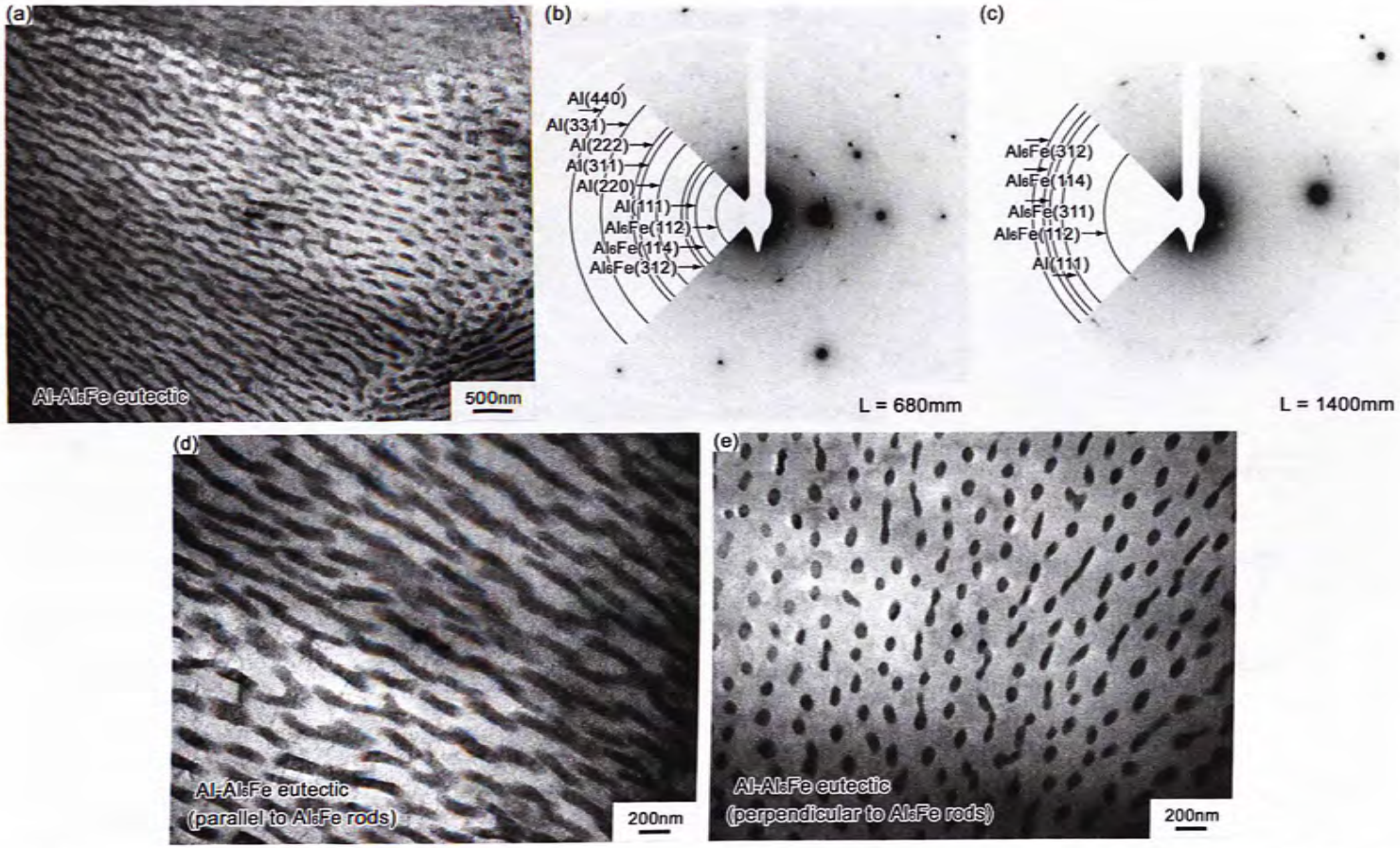

Fig. 5.12. (a) TEM micrograph of the region A (composed of Al-Al_6Fe eutectics) of the sample quenched from 900°C. (b-c) The selected area electron diffraction (SAED) patterns revealed rings corresponding to Al and Al_6Fe. (d) Enlarged views of the Al-Al_6Fe eutectic with Al_6Fe rods parallel to the paper. (d) Enlarged views of the Al-Al_6Fe eutectic with Al_6Fe rods perpendicular to the paper.

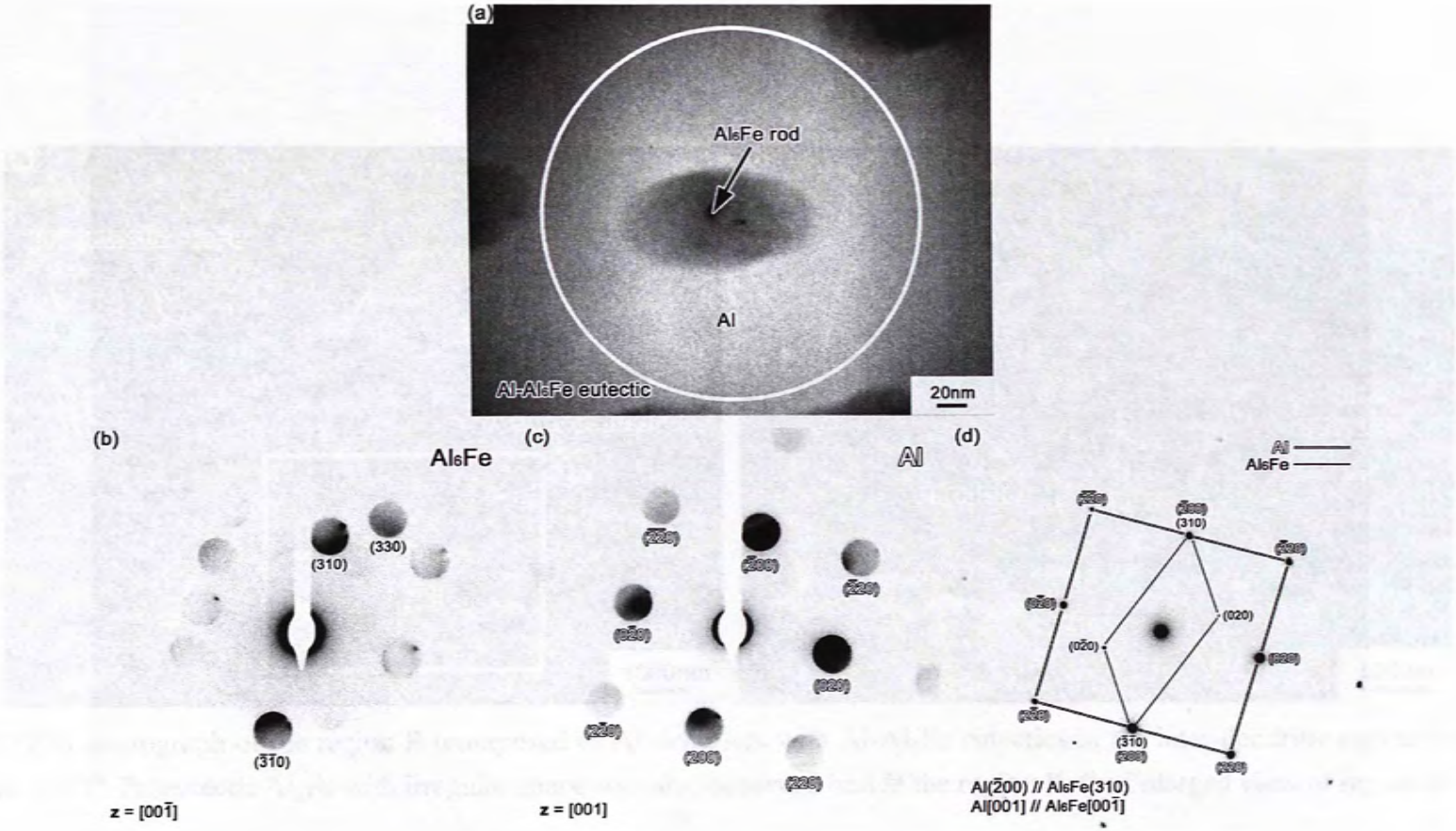

Fig. 5.13. (a) TEM micrograph of a Al_6Fe rod in the region A of the sample quenched from 900°C, with the rod perpendicular to the paper. (b) The converging beam electron diffraction (CBED) patterns of the Al_6Fe rod. (c)The CBED of the Al beside the Al_6Fe rod. (d) The selected area electron diffraction (SAED) pattern of the circled area.

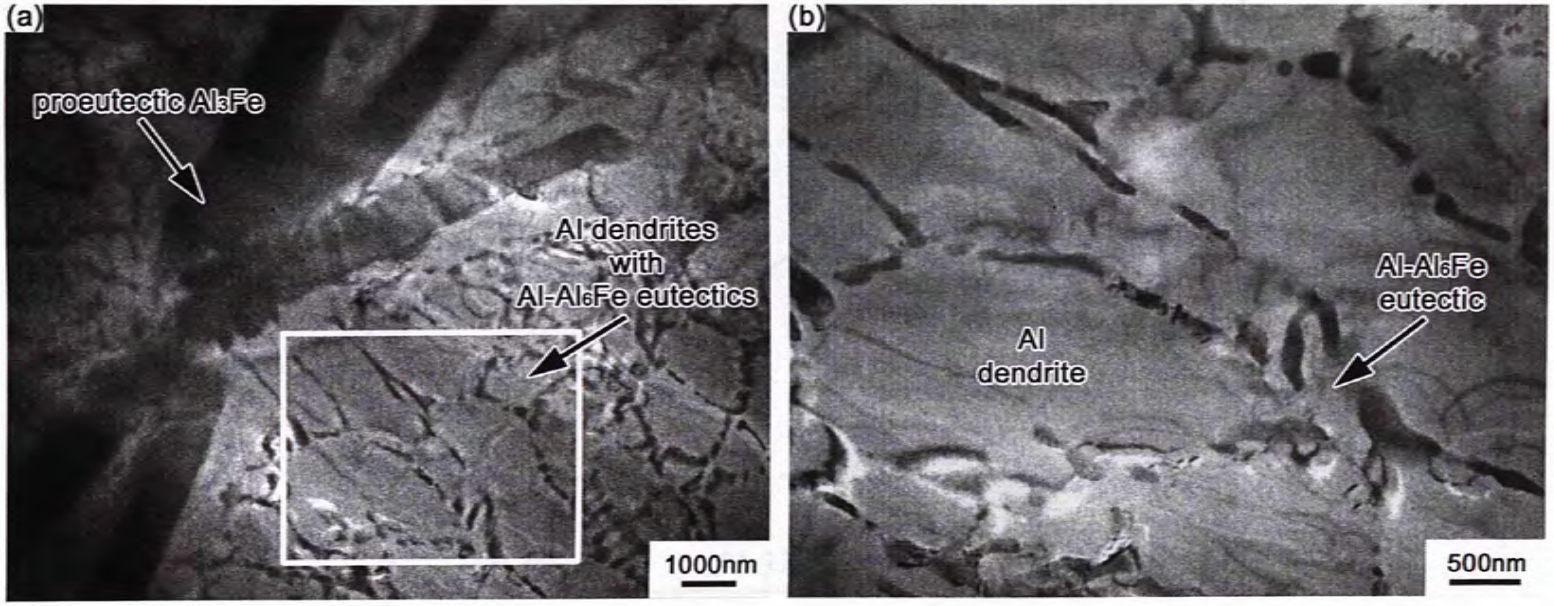

Fig. 5.14. (a) TEM micrograph of the region B (composed of Al dendrites with Al-Al_6Fe eutectics in the inter-dendritic regions) of the sample quenched from 900°C. Proeutectic Al_3Fe with irregular shape was also observed beside the region B. (b) Enlarged view of region B.

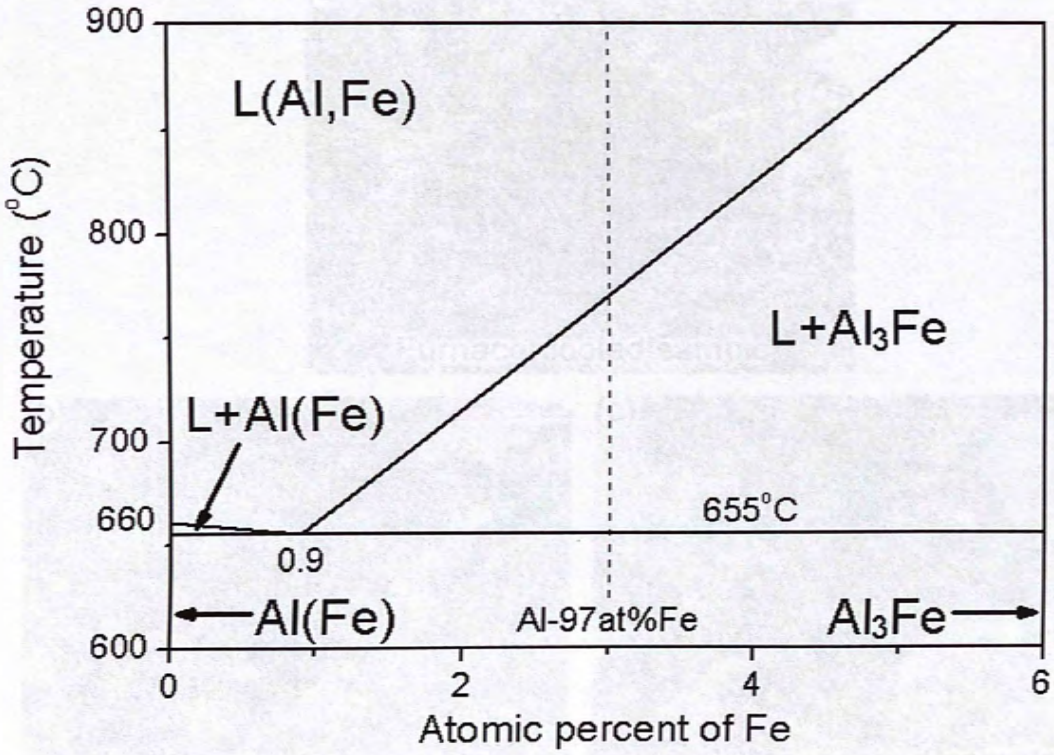

Fig. 5.15. An Al-Fe binary phase diagram, showing only the Al-rich side. [11]

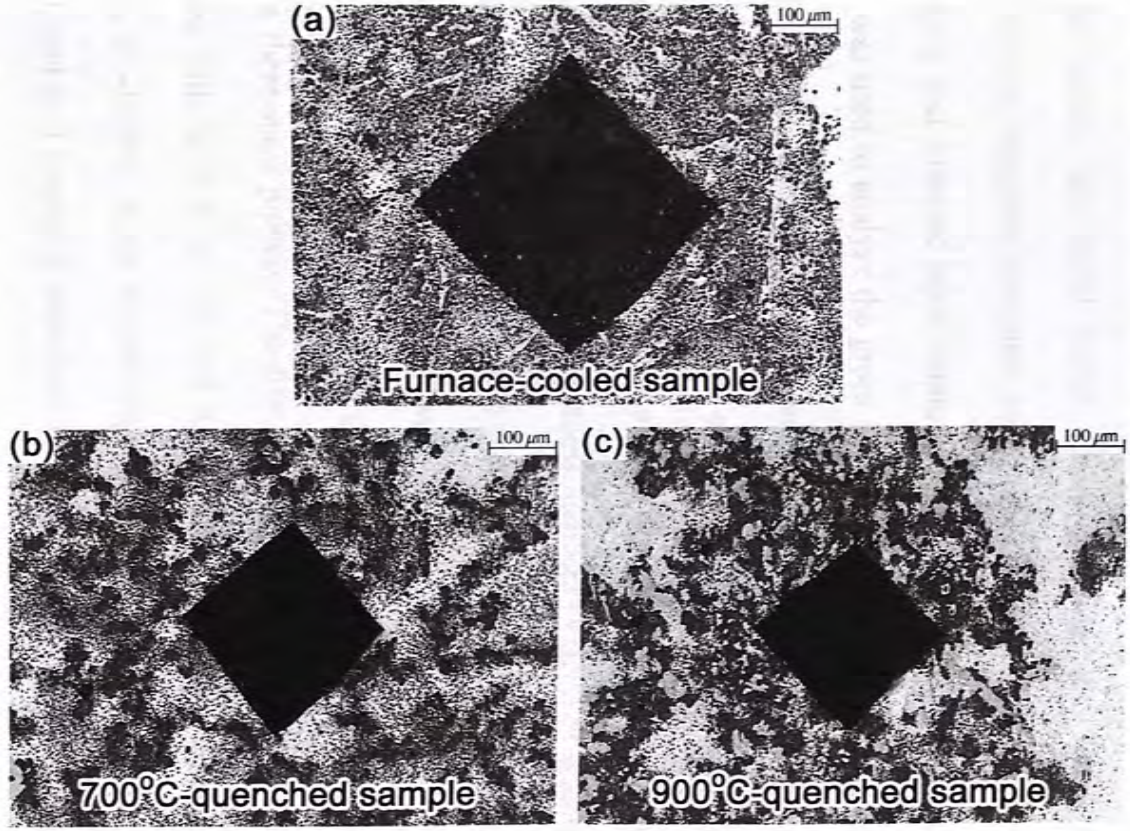

Fig. 5.16. Optical micrographs showing the indents on the samples after the Vickers hardness measurements using a 2000 gf load indenter. (a) Furnace-cooled sample. (b) 700°C-quenched sample. (c) 900°C-quenched sample.

Chapter 6 Conclusions and future work

6.1. Conclusions

By using simple and low-cost powder metallurgy routes, three types of MMC products were successfully synthesized by the displacement reactions between selected metals and metal oxides during sintering, they were Fe-based MMC reinforced by magnetic hercynite, Fe_3Al-based MMC reinforced by Al_2O_3, MgO or $MgAl_2O_4$, and Al-based MMC reinforced by Al-Fe intermetallics and Al_2O_3. DTA or DSC was used to analyze the green samples to determine the sintering temperatures for the studies. The green samples and sintered samples were characterized by XRD, OM, SEM, TEM and EDS. Based on these results, the reaction mechanisms were proposed to describe the formation of each type of MMCs. The values of saturation magnetization (m_s) and Vickers hardness numbers (VHNs) of selected samples were measured to investigate the magnetic and mechanical properties of the MMC products. The results are summarized as follows:

In the Fe-based MMC system, the displacement reaction between Al and Fe_3O_4 was a three-stage process. The first stage was initiated at ~900°C, in which Fe_3O_4 reacted with Al to form FeO and Al_2O_3. FeO was further reduced to form Fe and Al_2O_3 at ~1100°C in the second stage. The third stage occurred at ~1350°C where Al_2O_3 and FeO reacted to form hercynite. Due to the diffusion of Fe atoms in the iron layer into the newly-formed hercynite at elevated temperatures, the stoichiometric ratio of the resulting hercynite was deviated. Segregation of molten iron and hercynite were observed during the arc-melting of the green compact. It provided a simple method to extract pure hercynite. The values of m_s of hercynites obtained in this work were smaller than the literature value. This was explained by the deviation of the

stoichiometric ratio and the degree of inversion of the spinel structure.

In the Fe_3Al-based MMC system, the Fe_3Al matrices were reinforced by Al_2O_3, MgO or $MgAl_2O_4$. The Al_2O_3-reinforced MMC was synthesized by sintering of a Fe-Al-Fe_3O_4 mixture. At ~640°C, Al reacted with Fe to form Fe_2Al_5. The Fe_3O_4 was reduced by Fe_2Al_5 to amorphous FeO and Al_2O_3, and then to Fe and Al_2O_3 via a two-step displacement reactions occurred at temperatures beyond ~900°C. Meanwhile, diffusion of Al from Fe_2Al_5 to Fe resulted in the formation of Fe_3Al matrix. At 1400°C, all the reactions completed and a Fe_3Al-Al_2O_3 MMC was obtained. The wetting between Fe_3Al matrix and Al_2O_3 particle was poor. The displacement reaction between Mg and Al_2O_3 was utilized to form MgO instead of Al_2O_3 in the Fe_3Al-MgO MMC, which was produced by a two-step sintering of a Fe-Al-Mg-Al_2O_3 mixture. During the step-one sintering at 480°C, liquid Al_3Mg_2 formed and reacted with Al_2O_3 and Fe to form MgO and Fe_2Al_5, and a fragile sample containing Fe, Fe_2Al_5 and MgO was resulted. After re-pressing and step-two sintering, Fe_3Al matrix was formed and the Fe_3Al-MgO MMC was produced. Similarly, the Fe_3Al-$MgAl_2O_4$ MMC was synthesized by decreasing the relative amount of Mg. Residual Al_2O_3 reacted with MgO to form $MgAl_2O_4$ during the step-two sintering at 1400°C. The Fe_3Al-MgO and Fe_3Al-$MgAl_2O_4$ MMCs sintered at 1000 and 1400°C, respectively, had higher VHNs and relative densities than their pure Fe_3Al counterparts.

In the Al-based MMC system, the two-step displacement reaction between Al and Fe_3O_4 took place at 1100°C. Liquid (Al, Fe) with hypereutectic composition containing Al_2O_3 particles was obtained and was cooled down to room temperature by furnace-cooling, or by NaCl-solution-quenching from 700 or 900°C. Proeutectic Al_3Fe plates, divorced eutectic Al_3Fe and Al_2O_3 particles were found in the Al matrix. For the sample quenched from 700°C, Al dendrites with dendritic spacing of ~a few μm were formed and nano-scale Al-Al_6Fe eutectic was found in the inter-dendritic

regions. For that quenched from 900°C, the size of proeutectic Al_3Fe phases was reduced to ~tens of μm. The Fe-rich liquid solidified by eutectic transformation and Al-Al_6Fe eutectic containing Al_6Fe nanorods was formed, while the Fe-deficient liquid solidified in hypoeutectic manner and dendritic structures similar to that quenched from 700°C were formed. On average, the VHNs of the samples quenched from 700 and 900°C were 62% and 86% higher than that of the furnace-cooled sample.

6.2. Future work

In the study on the Fe-based MMC system, hercynites were successfully synthesized and extracted. However, the values of m_s of the hercynites were small due to deviation of the stoichiometric ratio and the inversion of the spinel structure. In order to suit engineering purposes, it is crucial to find some methods to inhibit the diffusion of Fe atoms in the iron layer into the newly-formed hercynite at elevated temperatures and retain the normal spinel structure, such that the value of m_s can be increased. Also, parameters such as permeability, coercive field and remanence are suggested to measure.

In the study on the Fe_3Al-based MMC system, although the MgO-reinforced and $MgAl_2O_4$-reinforced samples were measured to be 95% and 98% of their theoretical densities (TD), they were not high enough for structural applications. The density can be further increased by using pressure-assisted sintering such as hot isostatic pressing (HIP) technique. Moreover, standard tensile or bending specimens instead of pellets can be fabricated, so that more mechanical tests can be conducted. Also, the mechanical properties of the samples can be measured at elevated temperatures. To further investigate the wettabilty between the Fe_3Al matrix and reinforcements, high-resolution TEM images can be taken from the matrix/reinforcement interfaces.

In the study on the Al-based MMC system, the rapid coolings of the samples were achieved by NaCl-solution quenching. Apart from NaCl solution, other quenching media such as lubricating oil, distilled water and liquid nitrogen can be used to attain different cooling rates. In our samples, since the Al_2O_3 particles had no effect on the phase transformation in solidification, so that other particles can be used to determine whether they can act as nucleation sites of the Al-Fe intermetallics. Also, super-saturated Al(Fe) solid solution and meta-stable Al_6Fe phases were present in the quenched samples, which can be further annealed such that precipitations and re-crystallizations of stable Fe_3Al phases with interesting microstructures may occur. Furthermore, factors such as alloy compositions, cooling rates and morphologies of the eutectics, which may affect the crystallographic orientation relationships between Al and Al_6Fe have not been clarified in this work and further investigations are needed. Finally, other mechanical tests on tensile strength, shear strength, flexural strength and wear resistance are suggested to conduct on the samples.